

**Effect of Cutting Tool Microgeometry when Milling Hardened Steels,
A Finite Element Simulation and Surface Integrity Analysis**

by

Mohamd Imad

A thesis submitted to the
School of Graduate and Postdoctoral Studies in partial
fulfillment of the requirements for the degree of
Master of Applied Science in Mechanical Engineering

In

Faculty of Engineering and Applied Science

University of Ontario Institute of Technology (Ontario Tech University)

Oshawa, Ontario, Canada

January, 2021

© Mohamd Imad, 2021

THESIS EXAMINATION INFORMATION

Submitted by: **Mohamd Imad**

Master of Applied Science in Mechanical Engineering

Thesis title: Effect of Cutting Tool Microgeometry when Milling Hardened Steels, A Finite Element Simulation and Surface Integrity Analysis

An oral defense of this thesis took place on January 20, 2021 in front of the following examining committee:

Examining Committee:

Chair of Examining Committee	Dr. Martin Agelin-Chaab
Research Supervisor	Dr. Sayyed Ali Hosseini
Research Co-supervisor	Dr. Hossam Kishawy
Examining Committee Member	Dr. Remon Pop-Iliev
Thesis Examiner	Dr. Amirkianoosh Kiani, University of Ontario Institute of Technology

The above committee determined that the thesis is acceptable in form and content and that a satisfactory knowledge of the field covered by the thesis was demonstrated by the candidate during an oral examination. A signed copy of the Certificate of Approval is available from the School of Graduate and Postdoctoral Studies.

Abstract

This research work presents a 3D finite element model for the milling of hardened steels. The model was developed using ABAQUS/Explicit software and the Lagrangian approach was utilized. Experimental milling tests were performed to validate the numerically generated cutting forces and chip morphologies. A close agreement between the results was reported.

Moreover, experiments results were used to investigate the impact of cutting conditions and the microgeometry of cutting inserts on the cutting forces and the surface integrity. Two levels of feed rate, three levels of cutting speeds, and five levels of edge radii were utilized. The impact of edge radii on the workpiece surface integrity was analyzed in terms of 2D surface roughness, generated feed marks, subsurface plastic deformation, and subsurface microhardness.

Keywords: Milling; 3D finite element analysis; Cutting forces; Surface integrity; Inserts
Microgeometry

Author's Declaration

I hereby declare that this thesis consists of original work of which I have authored. This is a true copy of the thesis, including any required final revisions, as accepted by my examiners.

I authorize the University of Ontario Institute of Technology (Ontario Tech University) to lend this thesis to other institutions or individuals for the purpose of scholarly research. I further authorize University of Ontario Institute of Technology (Ontario Tech University) to reproduce this thesis by photocopying or by other means, in total or in part, at the request of other institutions or individuals for the purpose of scholarly research. I understand that my thesis will be made electronically available to the public.

Mohamd Imad

Acknowledgements

The research done in this thesis would have not been possible without the continuous support and motivation by my supervisors Dr. Sayyed Ali Hosseini and Dr. Hossam Kishawy. My supervisors provided me with a great working environment that had all the necessarily tools I needed to successfully conduct my research.

Many thanks to Dr. Nima Zarif-Yussefian and Sandvik Coromant for providing the custom-made cutting tools that were essential to conduct my research. I would like to also thank Mr. Richard Blackwell, Mr. Ian Wilcox, and Mr. Gus Meszaros from Opti-tech Scientific Inc for their support during samples feed marks analysis and samples etching. Additionally, I would like to acknowledge the members of my examination committee for their interest in my work and their feedback.

I would like to thank the members of the Machining Research Laboratory of the University of Ontario Institute of Technology namely: Dr. Hussien Hegab, Waleed Ahmed, Amr Salem, Connor Hopkins, Zahra Fattahi, and Zahra Khodabakhshi for always being available to help and making the past two years much more enjoyable. Moreover, many thanks to Waleed for his remarkable assistance and much appreciated inputs for the numerical work of my research. Additionally, special thanks to Connor for being a great teammate during the experimental work of this thesis and during the graduate courses that we took together.

My lovely people whom I spent countless late nights with and many nights at various study rooms and libraries, these memories were priceless and thank you for all of your support.

Dedication

This work is dedicated to my family whom continues to provide me with unconditional love and support. My father Dr. Imad Abdul-Karim and my mother Eman Jafar whom I have always looked up to with every decision I made, your sacrifices of leaving your home land and leaving everything behind so my siblings and I have a better life and better opportunities than the opportunities you had, has always motivated me to continuously work hard to make you proud and inshallah I will continue to do so.

Statement of Contributions

Part of the work described in Chapter 4 has been published as:

M. Imad, A. Hosseini, H. A. Kishawy, and N.Z. Yussefian, " 3D Finite Element Simulation of Cutting Forces in Milling Hardened Steels", Conference: Canadian Society for Mechanical Engineering (CSME) International Congress 2020, Prince Edward Island, Canada, 21-24 June, 2020.

I performed the majority of the experimental testing, development and execution of the numerical simulation and I am the sole author of this thesis.

Table of Contents

Abstract.....	iii
Author’s Declaration	iv
Acknowledgements	v
Dedication	vi
Statement of Contributions.....	vii
Table of Contents	viii
List of Figures.....	xi
List of Tables	xvii
List of Abbreviations and Symbols	xviii
Chapter 1: Introduction	1
1-1 Preamble	1
1-2 Motivation of Research.....	3
1-3 Breakdown of Thesis	4
Chapter 2: Literature Review.....	6
2-1 Preamble	6
2-2 Mechanics of Machining Processes.....	6
2-2-1 Cutting Tool Microgeometry.....	8
2-3 FEA in Metal Cutting	10
2-4 Surface Integrity	13
2-4-1 Impact of Cutting Edge Microgeometry on the Surface Integrity.....	14
2-5 Summary.....	19
Chapter 3: Metal Cutting Simulations Using FEA.....	20
3-1 Preamble	20
3-2 Model Formulations.....	20
3-2-1 Lagrangian Formulation	21
3-2-2 Eulerian Formulation.....	21
3-2-3 ALE Formulation.....	22
3-3 Time Integration Schemes	22
3-3-1 Implicit Analysis	23

3-3-2 Explicit Analysis	24
3-4 Workpiece Material Models	25
3-4-1 J-C Strength Material Model	26
3-4-2 Zerilli-Armstrong Material Model	34
3-5 Chip Generation.....	35
3-6 Workpiece Damage Model	37
3-7 Friction Models.....	42
3-7-1 Coulomb Friction Law Model	43
3-7-2 Constant Shear Friction Model.....	43
3-7-3 Stick-Slip Friction Model	43
3-8 FE Software Packages	44
3-9 Summary.....	45
Chapter 4: Numerical Simulation and Experimental Investigation	47
4-1 Preamble	47
4-2 Model Development	47
4-2-1 Assigning Workpiece Material Properties.....	48
4-2-2 Modeling of The Cutting Tool	51
4-2-3 Assembling Workpiece and Cutting Insert and Defining Boundary Conditions ...	55
4-3 Experimental Setup.....	58
4-4 Model Verification.....	62
4-4-1 Experimental and Numerical Cutting Forces Verification	62
4-4-2 Experimental and Numerical Chip Formation Validation.....	73
4-5 Impact of Cutting Conditions on the Experimental and Numerical Cutting Forces.....	76
4-6 Summary.....	81
Chapter 5: Effect of Tool Microgeometry and Cutting Conditions on the Surface Integrity	83
.....	
5-1 Preamble	83
5-2 The Significance of Surface Integrity and Experimental Analysis	83
5-3 Effects of Edge Radius and Cutting Conditions on The Surface Roughness and Tool Flank Wear.....	89
5-4 Effects of Edge Radius on the Feed Marks left on the machined Surface	93
5-5 Effects of Edge Radius on The Subsurface Plastic Deformation and Subsurface Microhardness.....	97
5-6 Summary.....	101
Chapter 6: Conclusions and Future works.....	102
6-1 Conclusions.....	102
6-2 Future Works	104
References.....	105
Appendix A. Feed Marks Figures	110

Appendix B. Subsurface Plastic Deformation Figures..... 128

List of Figures

Figure 1-1: Turning Process.....	2
Figure 1-2: Milling Process	2
Figure 2-1: Orthogonal Machining	7
Figure 2-2: Oblique Machining	7
Figure 2-3: (a) Down Milling Kinematics, (b) Up Milling Kinematics	8
Figure 2-4 A Solid End Mill.....	9
Figure 2-5: Micro Edge Radius.....	10
Figure 2-6: Honed and Chamfered Cutting Edges.....	10
Figure 2-7: The Method of K Factor, (a) $K=1$, (b) $K>1$, and (c) $K<1$	17
Figure 3-1: Boundary Conditions of ALE Formulation	22
Figure 3-2: Engineering Stress-Strain Curve.....	28
Figure 3-3: Steps Required to Obtain Constants B and n	29
Figure 3-4: Steps to Calculate Contact C	31
Figure 3-5: Steps Required to Calculate Contact m	33
Figure 3-6: Nodal Separation Method	36
Figure 3-7: Element Deletion Method.....	37
Figure 3-8: Specimen at the Necked Region	38
Figure 3-9: Stress Strain Curve for Materials Experiencing Progressive Damage Evolution.....	41
Figure 4-1: Cutting Insert and Workpiece Assembly In ABAQUS/Explicit™.....	48
Figure 4-2: Down Milling Kinematics.....	48
Figure 4-3: Meshed Workpiece in ABAQUS/Explicit™	51
Figure 4-4: Tool Holder and Cutting Insert [55, 56]	52
Figure 4-5: Steps Required to Draw the Cutting Insert in ABAQUS/Explicit™	54
Figure 4-6: Meshed Insert in ABAQUS/Explicit™.....	55

Figure 4-7: Initial Chip Load Formulation in ABAQUS/Explicit™	57
Figure 4-8: Reference Point Location in ABAQUS/Explicit™	57
Figure 4-9: 3-Axis HAAS VF-2BYT CNC Machining Center	58
Figure 4-10: Experimental Setup	59
Figure 4-11: Edge Radii Comparison	60
Figure 4-12: Numerical Forces Comparison Between Different Edge Radii	61
Figure 4-13: Experimental vs. Numerical Average Resultant Cutting Forces Fr	63
Figure 4-14: Feed Rate = 800 mm/min and Cutting Speed = 75 m/min	64
Figure 4-15: Feed Rate = 800 mm/min and Cutting Speed = 100 m/min	65
Figure 4-16: Feed Rate = 800 mm/min and Cutting Speed = 125 m/min	65
Figure 4-17: Feed Rate = 1000 mm/min and Cutting Speed = 75 m/min	66
Figure 4-18: Feed Rate = 1000 mm/min and Cutting Speed = 100 m/min	66
Figure 4-19: Feed Rate = 1000 mm/min and Cutting Speed = 125 m/min	67
Figure 4-20: Feed Rate = 800 mm/min and Cutting Speed = 75 m/min	68
Figure 4-21: Feed Rate = 800 mm/min and Cutting Speed = 100 m/min	68
Figure 4-22: Feed Rate = 800 mm/min and Cutting Speed = 125 m/min	69
Figure 4-23: Feed Rate = 1000 mm/min and Cutting Speed = 75 m/min	69
Figure 4-24: Feed Rate = 1000 mm/min and Cutting Speed = 100 m/min	70
Figure 4-25: Feed Rate = 1000 mm/min and Cutting Speed = 125 m/min	70
Figure 4-26: Numerical Model Error Discussion	73
Figure 4-27: Experimentally obtained Serrated Chip.....	74
Figure 4-28: Generation of a Serrated chip in ABAQUS/Explicit™	75
Figure 4-29: Forces at Feed Rate = 800 mm/min and Cutting Speed = 75 m/min	77
Figure 4-30: Forces at Feed Rate = 1000 mm/min and Cutting Speed = 75 m/min	77
Figure 4-31: Forces at Feed Rate = 800 mm/min and Cutting Speed = 100 m/min	78

Figure 4-32: Forces at Feed Rate = 1000 <i>mm/min</i> and Cutting Speed = 100 <i>m/min</i>	78
Figure 4-33: Forces at Feed Rate = 800 <i>mm/min</i> and Cutting Speed = 125 <i>m/min</i>	79
Figure 4-34: Forces at Feed Rate = 1000 <i>mm/min</i> and Cutting Speed = 125 <i>m/min</i>	79
Figure 5-1: Surface Roughness Measurements Setup	85
Figure 5-2: Specimens Cut Via Wire EDM.....	86
Figure 5-3: Leica DVM6 Digital Microscope [60].....	87
Figure 5-4: Schematic of a Wire EDM cut to Cold Mounted, Polished and Etched Specimen ...	87
Figure 5-5: XJP-403JT Optical Microscope	88
Figure 5-6: SMHV-1000A Digital Microhardness Tester	88
Figure 5-7: A Specimen in SMHV-1000A Digital Microhardness Tester	89
Figure 5-8: The Relationship of <i>Ra</i> , <i>Rq</i> , <i>ML</i> , and <i>Lsample</i>	90
Figure 5-9: Run 1 Top View of a Machined Specimen Using a 25 μm Edge Radius Insert.....	94
Figure 5-10: Run 31 Top View of a Machined Specimen Using a 30 μm Edge Radius Insert....	94
Figure 5-11: Run 31 Top View of a Machined Specimen Using a 35 μm Edge Radius Insert....	95
Figure 5-12: Run 22 Top View of a Machined Specimen Using a 40 μm Edge Radius Insert....	95
Figure 5-13: Run 23 Top View of a Machined Specimen Using a 45 μm Edge Radius Insert....	96
Figure 5-14: Zoomed-in Image of Run 22 Top View of a Machined Specimen Using a 40 μm Edge Radius Insert	96
Figure 5-15: Subsurface Microstructure of a Machined Specimen Using a 25 μm Edge Radius Insert	97
Figure 5-16: Subsurface Microstructure of a Machined Specimen Using a 30 μm Edge Radius Insert	98
Figure 5-17: Subsurface Microstructure of a Machined Specimen Using a 35 μm Edge Radius Insert	98
Figure 5-18: Subsurface Microstructure of a Machined Specimen Using a 40 μm Edge Radius Insert	99
Figure 5-19: Subsurface Microstructure of a Machined Specimen Using a 45 μm Edge Radius Insert	99

Figure 5-20: Experimentally Captured and Recorded Microhardness Readings.....	100
Figure A-1: Run 1 Top View of a Machined Specimen Using a 25 μm Edge Radius Insert.....	110
Figure A-2: Run 5 Top View of a Machined Specimen Using a 25 μm Edge Radius Insert.....	110
Figure A-3: Run 21 Top View of a Machined Specimen Using a 30 μm Edge Radius Insert...	111
Figure A-4: Run 26 Top View of a Machined Specimen Using a 30 μm Edge Radius Insert...	111
Figure A-5: Run 31 Top View of a Machined Specimen Using a 30 μm Edge Radius Insert...	112
Figure A-6: Run 35 Top View of a Machined Specimen Using a 30 μm Edge Radius Insert...	112
Figure A-7: Run 31 Top View of a Machined Specimen Using a 35 μm Edge Radius Insert...	113
Figure A-8: Run 36 Top View of a Machined Specimen Using a 35 μm Edge Radius Insert...	113
Figure A-9: Run 41 Top View of a Machined Specimen Using a 35 μm Edge Radius Insert...	114
Figure A-10: Run 45 Top View of a Machined Specimen Using a 35 μm Edge Radius Insert.	114
Figure A-11: Run 8 Top View of a Machined Specimen Using a 40 μm Edge Radius Insert...	115
Figure A-12: Run 13 Top View of a Machined Specimen Using a 40 μm Edge Radius Insert.	115
Figure A-13: Run 18 Top View of a Machined Specimen Using a 40 μm Edge Radius Insert.	116
Figure A-14: Run 22 Top View of a Machined Specimen Using a 40 μm Edge Radius Insert.	116
Figure A-15: Run 18 Top View of a Machined Specimen Using a 45 μm Edge Radius Insert.	117
Figure A-16: Run 23 Top View of a Machined Specimen Using a 45 μm Edge Radius Insert.	117
Figure A-17: Run 28 Top View of a Machined Specimen Using a 45 μm Edge Radius Insert.	118
Figure A-18: Run 32 Top View of a Machined Specimen Using a 45 μm Edge Radius Insert.	118
Figure A-19: Zoomed-in Image of Run 1 Top View of a Machined Specimen Using a 25 μm Edge Radius Insert	119
Figure A-20: Zoomed-in Image of Run 5 Top View of a Machined Specimen Using a 25 μm Edge Radius Insert	119
Figure A-21: Zoomed-in Image of Run 21 Top View of a Machined Specimen Using a 30 μm Edge Radius Insert	120
Figure A-22: Zoomed-in Image of Run 26 Top View of a Machined Specimen Using a 30 μm Edge Radius Insert	120

Figure A-23: Zoomed-in Image of Run 31 Top View of a Machined Specimen Using a 30 μm Edge Radius Insert	121
Figure A-24: Zoomed-in Image of Run 35 Top View of a Machined Specimen Using a 30 μm Edge Radius Insert	121
Figure A-25: Zoomed-in Image of Run 31 Top View of a Machined Specimen Using a 35 μm Edge Radius Insert	122
Figure A-26: Zoomed-in Image of Run 36 Top View of a Machined Specimen Using a 35 μm Edge Radius Insert	122
Figure A-27: Zoomed-in Image of Run 41 Top View of a Machined Specimen Using a 35 μm Edge Radius Insert	123
Figure A-28: Zoomed-in Image of Run 45 Top View of a Machined Specimen Using a 35 μm Edge Radius Insert	123
Figure A-29: Zoomed-in Image of Run 8 Top View of a Machined Specimen Using a 40 μm Edge Radius Insert	124
Figure A-30: Zoomed-in Image of Run 13 Top View of a Machined Specimen Using a 40 μm Edge Radius Insert	124
Figure A-31: Zoomed-in Image of Run 18 Top View of a Machined Specimen Using a 40 μm Edge Radius Insert	125
Figure A-32: Zoomed-in Image of Run 22 Top View of a Machined Specimen Using a 40 μm Edge Radius Insert	125
Figure A-33: Zoomed-in Image of Run 18 Top View of a Machined Specimen Using a 45 μm Edge Radius Insert	126
Figure A-34: Zoomed-in Image of Run 23 Top View of a Machined Specimen Using a 45 μm Edge Radius Insert	126
Figure A-35: Zoomed-in Image of Run 28 Top View of a Machined Specimen Using a 45 μm Edge Radius Insert	127
Figure A-36: Zoomed-in Image of Run 32 Top View of a Machined Specimen Using a 45 μm Edge Radius Insert	127
Figure B-1: Subsurface Microstructure of a Machined Specimen Using a 25 μm Edge Radius Insert at Run 1	128
Figure B-2: Subsurface Microstructure of a Machined Specimen Using a 25 μm Edge Radius Insert at Run 5	128

Figure B-3: Subsurface Microstructure of a Machined Specimen Using a 30 μm Edge Radius Insert at Run 21 129

Figure B-4: Subsurface Microstructure of a Machined Specimen Using a 30 μm Edge Radius Insert at Run 26 129

Figure B-5: Subsurface Microstructure of a Machined Specimen Using a 30 μm Edge Radius Insert at Run 31 130

Figure B-6: Subsurface Microstructure of a Machined Specimen Using a 30 μm Edge Radius Insert at Run 35 130

Figure B-7: Subsurface Microstructure of a Machined Specimen Using a 35 μm Edge Radius Insert at Run 31 131

Figure B-8: Subsurface Microstructure of a Machined Specimen Using a 35 μm Edge Radius Insert at Run 36 131

Figure B-9: Subsurface Microstructure of a Machined Specimen Using a 35 μm Edge Radius Insert at Run 41 132

Figure B-10: Subsurface Microstructure of a Machined Specimen Using a 35 μm Edge Radius Insert at Run 45 132

Figure B-11: Subsurface Microstructure of a Machined Specimen Using a 40 μm Edge Radius Insert at Run 8 133

Figure B-12: Subsurface Microstructure of a Machined Specimen Using a 40 μm Edge Radius Insert at Run 13 133

Figure B-13: Subsurface Microstructure of a Machined Specimen Using a 40 μm Edge Radius Insert at Run 18 134

Figure B-14: Subsurface Microstructure of a Machined Specimen Using a 40 μm Edge Radius Insert at Run 22 134

Figure B-15: Subsurface Microstructure of a Machined Specimen Using a 45 μm Edge Radius Insert at Run 18 135

Figure B-16: Subsurface Microstructure of a Machined Specimen Using a 45 μm Edge Radius Insert at Run 23 135

Figure B-17: Subsurface Microstructure of a Machined Specimen Using a 45 μm Edge Radius Insert at Run 28 136

Figure B-18: Subsurface Microstructure of a Machined Specimen Using a 45 μm Edge Radius Insert at Run 32 136

List of Tables

Table 3-1: Comparison Between Explicit and Implicit Time Integration Schemes	46
Table 3-2: Comparison Between Commonly Utilized FE Software	46
Table 4-1: Workpiece Material General Properties [54]	49
Table 4-2: Constants of J-C Strength Model [21].....	49
Table 4-3: Constants of J-C Fracture Model [21].....	50
Table 4-4: Dimensions of Cylindrical Shank and cutting Insert [55, 56].....	52
Table 4-5: Experimental Cutting Conditions.....	62
Table 4-6: Comparison Between Feed Rates and Cutting Speeds.....	76
Table 5-1: Ra μm (Runs 1-5) and VB μm (Run 5) Measurements	91
Table 5-2: Ra μm (Runs 16-20) and VB μm (Run 20) Measurements	91

List of Abbreviations and Symbols

RDOC	Radial depth of cut
ADOC	Axial depth of cut
R&D	Research and development
FEA	Finite element analysis
J-C	Johnson-Cook
ALE	Arbitrary lagrangian formulation
FCC	Face centered cubic
BCC	Body centered cubic
W	Width of cut
t_0	Uncut chip thickness
i	Inclination angle
η_c	Chip flow angle
ϕ_{st}	Start angle
ϕ_{ex}	Exit angle
f	Feed per tooth
r_β	Edge radius
S_γ	Rake face segment
S_α	Flank face segment
V	Cutting speed
M	Mass matrix
P	External applied load
I	Internal force
\ddot{u}	Nodal acceleration

$\Delta t_{critical}$	Critical time
L_{e0}	Initial length of an element
E	Young's Modulus
ν	Poisson's ratio
ρ	Density
\dot{u}	Nodal velocity
Δt	Time increment
t	Time of a current increment
u	Nodal displacement
σ	Von Mises flow stress
A	Yield stress
B	Strength coefficient
C	Strain sensitivity constant
n	Strain hardening exponent
m	Thermal sensitivity constant
ε	Equivalent plastic strain
ε^f	Equivalent plastic fracture strain
$\dot{\varepsilon}$	Strain rate
$\dot{\varepsilon}_0$	Reference strain rate
$\dot{\varepsilon}^*$	Plastic strain rate
T	Temperature
$T_{Reference}$	Reference temperature
$T_{Melting}$	Melting temperature
T^*	Homologous temperature

C_0	Zerilli-Armstrong stress parameter
$C_1 - C_5$	Zerilli-Armstrong material constant
n_{ZA}	Zerilli-Armstrong material constant
$D_{critical}$	Critical distance
w	Damage initiation parameter
D	Damage parameter
σ^*	Stress triaxiality
σ_m	Average of the three normal stresses
R	Radius of the necked region
a	Minimum cross-sectional area
$D_1 - D_5$	Johnson-Cook damage model constants
L	Characteristic length when calculating the damage parameter
$\bar{\epsilon}^{pl}$	Equivalent plastic strain when calculating the damage parameter
\bar{u}^{pl}	Equivalent plastic displacement when calculating the damage parameter
\bar{u}_f^{pl}	Equivalent plastic displacement at failure when calculating the damage parameter
σ_y	Yield stress
σ_{y0}	Yield stress at onset damage
$\bar{\epsilon}_0^{pl}$	Equivalent plastic strain at the onset damage
G_f	Fracture energy
K_c	Fracture toughness
L_e	Length of an element
τ	Shear stress
σ_n	Normal stress
μ	Coulomb's friction coefficient

m_s	Constant shear friction factor
k_s	Shear flow stress
L_c	Tool chip contact length
$W1$	Width of an insert
LE	Cutting edge effective length of an insert
RE	Corner radius of an insert
BS	Wiper edge length of an insert
S	Thickness of an insert
S_{speed}	Spindle speed
N_t	Number of teeth/inserts
F	Feed rate
D_{tool}	Tool's diameter
F_x	Cutting force in the x -direction
F_y	Cutting force in the y -direction
F_z	Cutting force in the z -direction
F_r	Resultant cutting force
\bar{F}_x	Average of cutting forces in the x -direction
\bar{F}_y	Average of cutting forces in the y -direction
\bar{F}_z	Average of cutting forces in the z -direction
\bar{F}_r	Average of resultant cutting forces
$ \bar{F}_x $	Absolute average of cutting forces in the x -direction
$ \bar{F}_y $	Absolute average of cutting forces in the y -direction
$ \bar{F}_z $	Absolute average of cutting forces in the z -direction
$ \bar{F}_r $	Absolute average of resultant cutting forces

EDM	Electrical discharge machining
R_a	Arithmetic mean value
R_q	Root-mean square average
M_L	Mean line
L_{sample}	Sample length
q	Single sample measurement
j	Number of q measurements
VB	Flank wear

Chapter 1: Introduction

1-1 Preamble

Metal removal processes are categorized into three categories namely conventional processes, abrasive processes, and advanced (nontraditional) processes. Conventional processes, also known as machining processes comprise of turning, milling, drilling, broaching, etc. Abrasive processes include grinding, lapping, honing, and ultrasonic machining. Advanced or nontraditional processes refer to metal removal processes that uses chemical, thermal, electrical, and optical sources of energy to remove workpiece material.

Machining processes utilize sharp cutting tools to remove the material and shape raw workpiece into a desired final product. Turning and milling are the most commonly used cutting (metal removal) processes within the machining industry. A combination of tool and workpiece motions are utilized by these processes to manufacture various parts of many shapes and complexities [1]. Schematics of turning and milling are displayed in Figure 1-1 and Figure 1-2, respectively. These processes are able to produce geometrically complex parts with tight tolerances, which other manufacturing processes such as bulk deformation and casting cannot achieve [2]. Components manufactured via bulk deformation or casting processes still require finish machining to reach the required surface quality and dimensional accuracy. This combination of features makes machining processes almost irreplaceable in the manufacturing industry. Despite their capabilities and flexibilities in producing complex parts of high quality and tight tolerances, machining processes are wasteful of material and thus placed toward the end of the manufacturing chain. Thus, machining processes undergo continuous optimization and improvement to lower the cost and increase productivity.

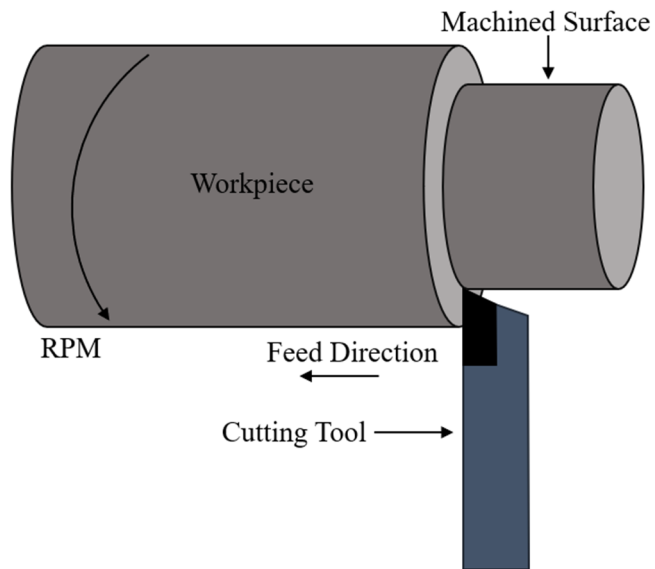


Figure 1-1: Turning Process



Figure 1-2: Milling Process

Chapter 1: Introduction

Optimization of machining processes requires great knowledge of the process and its components and it highly depends on the proper selection of machine tool, cutting tool, and cutting parameters. Considering the fact that switching between different machine tools might not be an option, carefully designing the cutting tools and optimizing cutting conditions play an important role in improving machining processes.

Optimizing cutting conditions (e.g., cutting speed, feed rate, radial depth of cut (RDOC), and axial depth of cut (ADOC)) is simpler and cheaper than refining the tool design (i.e., geometrical features of tools) since cutting conditions can be easily altered. Optimization of cutting parameters is executed by investigating the impact of each of the cutting conditions on the process output parameters such as dimensional accuracy, surface integrity, tool life, etc. The results allow researchers to find the most practical combination of parameters that yield the best production rate, best surface quality, and the longest tool life. In contrast, optimization of cutting tools and their geometrical features is not as straightforward as optimization of cutting condition as it needs tools with different geometrical features (i.e., edge radius, nose radius, rake angle, etc.) to study the effect of those features on output parameters (i.e. cutting forces, surface integrity, and tool life).

1-2 Motivation of Research

Design of cutting tools requires extensive research and development (R&D) and experienced tool designers. This process involves analysis, experimentations, and sometimes trial and errors until the best tool with optimum design is obtained and manufactured in large scale. This process is costly and time consuming; therefore, having access to reliable simulations and models that enable tool designers to test their design in a less costly virtual environment is extremely important.

Chapter 1: Introduction

In this context, Finite Element Analysis (FEA) models provides designers with enough data that enhance the decision-making process during the design stage of cutting tools. The provided data include properties that are difficult to capture experimentally and/or calculate analytically such as stress distribution, temperature distribution, tool/chip contact length, cutting forces, etc. In this context, models for 3D milling processes are difficult to develop mainly because of the variable chip thickness during the cut and the relatively complex nature of the process. Therefore, there has been limited works that proposed and developed such 3D FEA models for milling.

Cutting conditions along with cutting tool geometry also affect the integrity of machined surface thereby influence the performance of the workpiece during its service life. Investigations of the influence of cutting conditions on machined surfaces are widely available. However, there has been limited research that investigated the impact of milling tools microgeometry on the quality and integrity of machined surface. Cutting edge microgeometry plays a major role in the mechanics of chip formation [3]. Investigating the impact of milling tools microgeometry on the mechanics of chip formation will help tool designers and enhance their ability to include the impact of geometrical parameters on the tool performance and surface quality. Additionally, tool designers will be able to use the provided data to select an optimum tool for any specific purpose.

1-3 Breakdown of Thesis

Mechanics of milling processes and the impact of milling inserts microgeometry is thoroughly investigated in this thesis. This thesis is broken down into six chapters. The first chapter introduces the work and its significance on the field of metal cutting. The second chapter presents an extensive literature review of the works that proposed and developed 2D and 3D metal cutting FEA models with a focus on turning and milling. Also, research that investigated the impact of edge radius on the surface integrity during turning and milling processes are highlighted.

Chapter 1: Introduction

Chapter three discusses methods and steps involved in the development of FE models including numerical formulations, time integration schemes, material models, chip generation methods, damage models, friction models, and advantages/disadvantages of common FEA solvers. Chapter four presents and validates a detailed 3D FEA model for milling of hardened AISI 4340 steel via ABAQUS/Explicit™ solver. The model is validated in terms of cutting forces and chip morphology. Chapter five investigates the surface integrity of machined AISI 4340 steel. The surface integrity examination is broken down into 2D surface roughness, plastic subsurface deformation, and subsurface microhardness. Finally, chapter six summarizes the work and highlights recommendations for future research within this topic.

Chapter 2: Literature Review

2-1 Preamble

This chapter consists of three main sections. The first section discusses mechanics of machining processes and includes a subsection that highlights the importance of inserts' microgeometry. Notable works in the literature that constructed and presented machining FEA models are highlighted in the second section. Lastly, the third section discusses the significance of machined surface integrity, while reviewing works that investigated the impact of cutting edge microgeometry on the surface integrity.

2-2 Mechanics of Machining Processes

Machining is a process in which a sharp wedge-shaped cutting tool removes raw workpiece material to create the final product. Quality of the final product is expressed by various measures which surface quality and/or dimensional accuracy are among the most important factors. Generally, machining is modelled either as a simple 2D orthogonal cutting process or a more complicated 3D oblique cutting process [4]. An orthogonal cutting process is defined by its straight cutting edge that is perpendicular to the direction of the cut. Oblique cutting in its least complex forms is parted from orthogonal cutting by having its cutting edge set on an angle, known as the inclination angle. An orthogonal cutting process and an oblique cutting process are displayed in Figure 2-1 and Figure 2-2, respectively. W , t_0 , i , η_c represent the width of cut, uncut chip thickness, inclination angle, and chip flow angle.

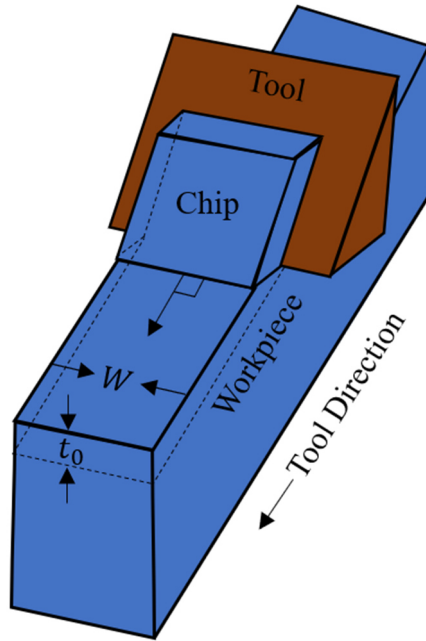


Figure 2-1: Orthogonal Machining

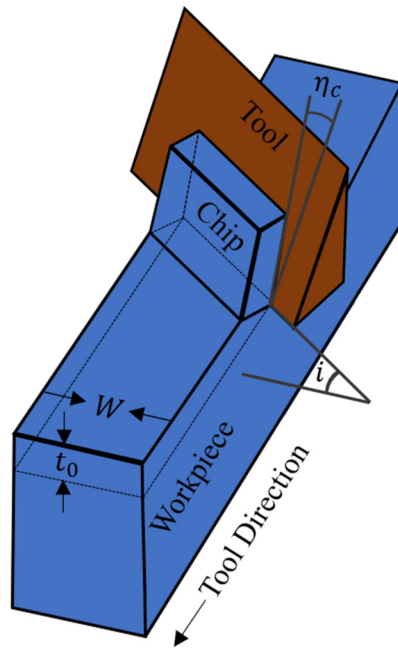


Figure 2-2: Oblique Machining

Milling is one of the most commonly used machining processes due to its ability to produce variety of complex parts [5]. Kinematics of milling are categorized as up milling or down milling, both generate variable chip thickness. The main difference between both kinematics is that up

milling initiates its cut with a small chip thickness and completes the cut with a large chip thickness, while down milling initiates the cut with a large chip thickness and completes the cut with a small chip thickness. In up milling, the insert experiences a high chip load at the end of the cut while in down milling, it sustains a high chip load at the starting point of each cut. Another perspective that may be used to distinguish both kinematics is by their start angle ϕ_{st} and exit angle ϕ_{ex} . In a half immersion scenario, an up-milling kinematic has a ϕ_{st} , and ϕ_{ex} of 0° and 90° , respectively. While, a half immersion down milling kinematic has a ϕ_{st} , and ϕ_{ex} of 90° and 180° , respectively. Both milling kinematic are presented in Figure 2-3 (a and b). Moreover, f in both figures is the feed per tooth. Please note other immersion angles are also possible during milling processes.

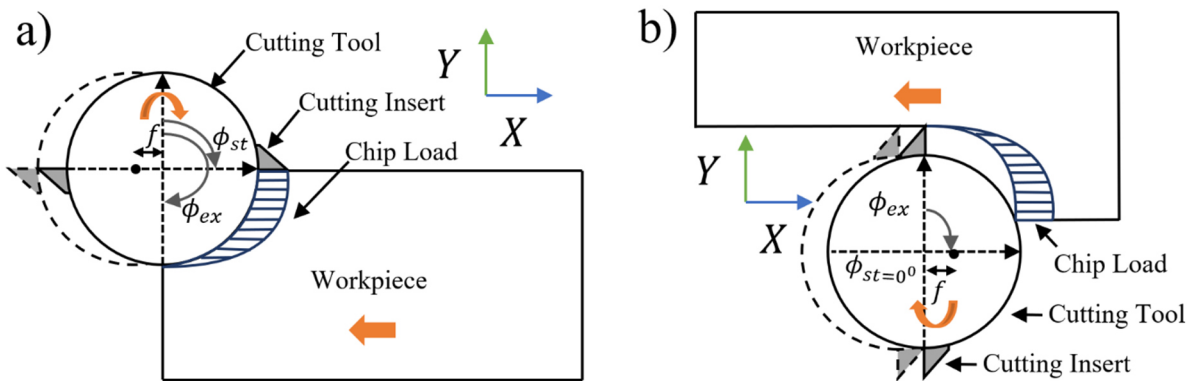


Figure 2-3: (a) Down Milling Kinematics, (b) Up Milling Kinematics

2-2-1 Cutting Tool Microgeometry

Cutting tools geometrical features can be categorized to macro and micro features. Macro features are shown in Figure 2-4. Features include but not limited to overall length, length of cut, number of flutes, length of flute, cut diameter, shank diameter, etc. In regards of micro-geometrical features, the edge radius (r_β) is considered to be the most influential one, because it is the first part of the tool that engages with the workpiece during machining [6]. Cutting edge radius impacts

Chapter 2: Literature Review

many parameters including cutting forces, tool life, and surface integrity of the final product [7]. Representation of r_β is shown in Figure 2-5. Cutting edges are constructed by various methods of the edge preparation process. Methods include drag finishing, brush honing, micro-blasting, etc. [3]. Edge preparation enhances the rigidity of sharp edged cutting tools, allowing for better control of the produced chips and improving the coating deposition process [8]. Figure 2-6 illustrates the schematics of honed and chamfered cutting edges, which are produced by edge preparation. Different shapes of cutting edges can be utilized best for different scenarios. Round honed cutting edges can produce better surface quality in comparison to chamfered cutting edges. However, this type of microgeometry can cause larger plastic deformation on the newly machined surface. Chamfered cutting edges have higher strength because they are able to utilize the collected built-up edge material to form a new effective rake angle, that is able to shear material smoothly. Therefore, they perform better during roughing cuts and tend to have better tool life characteristics [9].

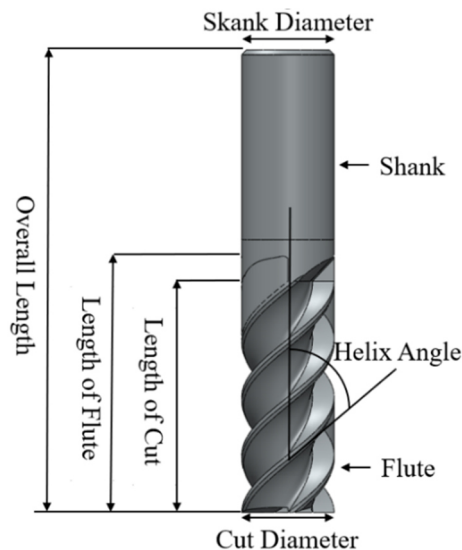


Figure 2-4 A Solid End Mill

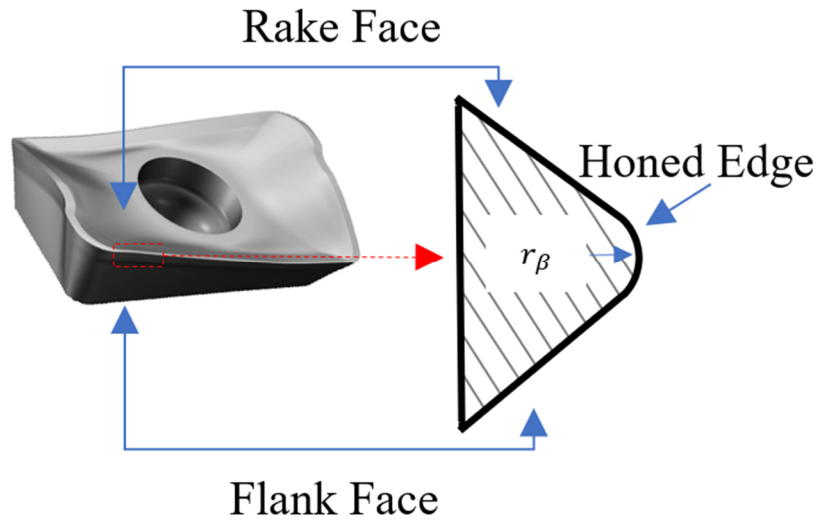


Figure 2-5: Micro Edge Radius

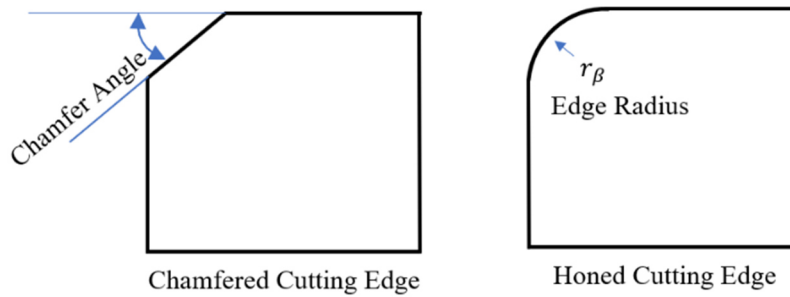


Figure 2-6: Honed and Chamfered Cutting Edges

2-3 FEA in Metal Cutting

FEA models are great apparatus in the hands of tool designers that enable them to successfully test the tools in a virtual environment before prototyping. FEA models are often used to obtain properties and features, that are either extremely difficult or impossible to capture experimentally and/or analytically. Such properties include stress distribution, temperature distribution, tool/chip numerically calculated contact length, etc. Features comprise modelling various complex/irregular shapes at low cost, providing highly accurate results (when boundary conditions are set accurately), producing a visual image of the results, and allowing designers to spot vulnerable

Chapter 2: Literature Review

points within their designs. Researchers have developed 2D orthogonal and 3D machining models in the literature to investigate machining processes thoroughly. 2D orthogonal FEA models are the most commonly developed models in machining. They have the ability to predict process outputs and have been developed within various software packages.

2D models of milling have limited abilities because their plain strain deformation assumption can only be applied when the nose radius is much smaller than the radial depth of cut [10]. 2D FEA models of machining, especially for milling, are not that realistic and thus not very common in modelling and simulation of milling process. 2D machining models are mainly used to simulate turning processes. 2D orthogonal FEA models have been developed/validated utilizing three commonly used software packages. ABAQUS/Explicit™ was adopted by Özel and Zeren [11], Ramesh and Melkote [12], Chen et al. [13], Xi et al. [14], and Ghandehariun et al. [15]. AdvantEdge™ was used by Maranhão and Davim [16], Jiang and Wang [17]. DEFROM-2D® was utilized by Özel and Altan [18], Wang et al. [19], and Yen et al. [20]. The plain strain assumption of 2D orthogonal models has driven researchers to develop 3D models which present a more realistic and reliable representation of machining processes. 3D FEA models of turning process have also been developed using various FEA solvers. ABAQUS/Explicit™ was utilized by Ng et al [21], Soo et al [22], and Zhang [23]. AdvantEdge™ was employed by Li and Shih [24] and Ma et al. [25]. DEFROM-3D® was used by Aurich and Bill [26], Özel [27], and Yadav et al. [28]. Unlike turning process in which the geometry of engagement between the tool and workpiece remain constant, in milling the cutting tool rotates about its axis and travels over the workpiece surface. This combination of motions results in a complex engagement, which produces chips that are variable in thickness. Due to this complexity, creating 3D FEA models for milling is not as convenient as that of turning. Few 3D milling models have been proposed in the literature. Pittalà

et al. [10] utilized DEFORM-3D FEA to develop a 3D face milling model for the milling of a 6000 series aluminum alloy using indexable tools. The model was able to predict cutting forces and investigate the real geometry of used of the cutting inserts. Soo et al. [29] used ABAQUS/Explicit™ to develop a Lagrangian 3D end milling model that simulated the milling of Inconel 718 by a solid ball nose cutter. During the model validation step, numerical forces in the feed and step over directions were found to be within the 10% range of experimental ones. However, forces in the axial direction had a discrepancy of around 90% in comparison to those obtained from experiments. The large error was related to the elements deletion technique that was implemented in the model. The element deletion technique impacted the contact between the cutting edge and the newly machined workpiece surface and caused the contact area to be removed, which in turn did not allow the software to capture forces in the axial direction. Also, the model contained an additional layer of validation by comparing the numerical and experimental shear zone temperatures. Later, AdvantEdge was adopted by Rao et al. [30] to propose an updated Lagrangian 3D FEA model for face milling. The model was used to simulate the machining of Ti-6Al-4V titanium alloy by an indexable cutter. It was designed to predict the specific cutting energy, the tool-chip contact length, and stress/temperature distributions. Moreover, based on the FEA predicted outputs, a tool flank wear model was developed. Furthermore, an end milling 3D FEA model in ABQUS/Explicit was created by Wu et al. [31] to simulate the milling of Ti-6AL-4V titanium alloy using a solid end mill. A Johnson-Cook (J-C) material model constants were experimentally derived for the workpiece material. The utilization of ABAQUS/Explicit™ software allowed authors to capture multiple properties including generated chips, stresses/temperature distributions, and cutting forces. Further developments of FEA 3D milling modeling of Ti-6Al-4V titanium alloy was presented by Thepsonthi and Özel [32] where authors

employed DEFORM-3D to develop multiple 3D micro-end milling models. Models were used to examine the impact of increasing the edge radius on tool wear. Edge radius was investigated during up/down milling kinematics, half immersion, full immersion RDOC and slot micro end milling. Davoudinejad et al [33], utilized AdvantEdge to propose a Lagrangian 3D FEA model that simulated the milling of Al6082-T6 aluminum alloy. Moreover, a Lagrangian FEA 3D end milling model was proposed by Bolar and Joshi [34]. ABAQUS/Explicit™ was utilized to simulate the thin-wall end milling of Aluminum 2024-T351 by a solid end milling and the impact of cutting parameters on cutting forces, stress distributions, cutting temperature, workpiece deflection, and chip morphology was investigated. ABAQUS/Explicit™ was also used by Zhang et al. [35], to develop a 3D FEA model during the hard milling of AISI H13 steel by a milling circular indexable insert to explore the impacts of cutting speeds and feed rates on cutting temperatures and cutting forces.

2-4 Surface Integrity

The term surface integrity was first used in 1964 by Michael Field and John F. Kahles to refer to the workpiece surface condition after undergoing a manufacturing process [36]. The surface integrity of a machined workpiece directly influences the physical appearance of the machined workpiece, wear and friction properties, effectivity of post-process machining operations (welding, coating, painting, etc.), thermal and electrical conductivity, and cracks initiation due to defects within the surface [2]. The integrity of machined surface, including the outer surface and immediate subsurface layers, is impacted by stresses induced during machining as well as generated temperatures [4]. According to Paulo [37], the surface integrity characteristics of a workpiece tend to change after machining. Characteristics of surface integrity may be categorized into geometrical, physical/chemical, crystallographic, and mechanical properties. Therefore, to

improve the overall quality and lower the machining cost, it is crucial to investigate and understand the impact of machining processes and parameters on the newly machined surfaces.

After Field and Kahles first used the term “surface integrity”, the application of this term has not been consistent throughout the literature [4]. However, according to the 11th edition of Black and Kohser’s book “Degramo’s Materials and Processes in Manufacturing” this term is commonly divided into two categories [36]. The first category is topography characteristics, which include surface roughness, waviness and form errors. The second category is surface layer characteristics, which includes subsurface plastic deformation, metallurgical changes (microhardness, recrystallization, etc.), induced residual stress and surface cracks [36].

2-4-1 Impact of Cutting Edge Microgeometry on the Surface Integrity

Effect of individual cutting parameters such as cutting speed, feed rate, axial/radial depths of cut on the surface integrity may be investigated individually straightforwardly, because they can be changed easily during the tests. However, geometrical parameters are much more difficult to investigate as they require manufacturing cutting tools of different geometry to be tested. Such custom made tools for tests are not available off-the-shelf and must be prototyped accordingly, which is significantly costly and need access to the necessary equipment. One of the geometrical parameters that is of an interest to researchers is the radius of the cutting edge of cutting tools. Edge radius has a significant impact on the generated cutting forces, stress/temperature distributions, tool wear, tool life, and notably the surface quality.

Researchers mainly looked into the effect of tool microgeometry during turning processes due to the lower associated complexity of turning in comparison to milling. Hughes et al. [38], investigated the impact of two cutting inserts during the machining of Ti-6Al-4V titanium alloy.

Chapter 2: Literature Review

Inserts were ground inserts with an edge radius of 10-20 μm and directly pressed inserts with edge rounding treatment with an edge radius of around 40 μm . The study included two levels of cutting speeds and two levels of feed rate. Their results concluded that the inserts of the 40 μm edge radius generated smoother surfaces in comparison to the inserts with 10-20 μm edge radii. Pu et al [39], examined the impact of variable inserts edge radii on the surface integrity when turning of AZ31B Magnesium alloy with two uncoated 30 μm and 70 μm edge radii inserts. They also studied the effects of dry and cryogenic cooling strategies. It was concluded that when machining under cryogenic cooling conditions and using the larger 70 μm edge radius cutting inserts, better surface integrity was observed. Multiple combinations of symmetric cutting edge radii were explored by Denkena et al [40]. During their research the impact of cutting tools edge radius and cutting conditions, while turning AISI 51200 steel with hardness of 62 HRC roller bearings was examined. Inserts edge radii were 40 μm , 50 μm , 70 μm , 80 μm , and 100 μm . It was found that larger cutting edge radius as well as larger feeds resulted in higher compressive stresses on the surface of the machined workpiece. In addition, an increase in white layers formation was observed when using a larger edge radius. This is due to the increase in the cutting zone temperature when employing larger edge radii cutting tools. The influence of varying cutting edge radii of cutting inserts on process output parameters (including the surface quality) when turning hardened AISI 51200 with a hardness of 53-58 HRC was investigated by Zhao et al [9]. Inserts edge radii were 20 μm , 30 μm , and 40 μm . Their works indicated that the most optimum surface roughness values were generated, when the 30 μm radius cutting tools was used. Mainly because higher processes stability was observed while using the 30 μm edge radius in comparison to the 20 μm and the 40 μm cutting edge radii inserts.

Chapter 2: Literature Review

As mentioned earlier, milling is more complex in comparison to turning, mainly due to the variation of chip thickness and the fact that it is an intermitted machining process. Therefore, there has been limited works that looked into the impact of tools geometrical parameters on the surface integrity of milled parts. A notable research that have covered milling processes was presented by Denkena et al [41], where the influence of honed cutting edged inserts on tool wear, burr formation, and residual stresses, was analyzed during the slot milling of 42CrMo4 steel alloy. They applied the characterization method of K factor, which is used to design symmetric and asymmetric honed cutting inserts. This method consists of two edge segments namely the rake face edge segment S_γ and the flank face edge segment S_α . In the K factor method $K = S_\gamma / S_\alpha$. Figure 2-7 displays the three possible scenarios. Figure 2-7-a presents a symmetric honed edge radius. Symmetric honed edge is commonly known as symmetric hone [8]. Figure 2-7-b, illustrates a case when K is larger than 1, which means that the influence of S_γ and the rake face is greater than that of S_α and the flank face. In this case, the honed edge is known as reverse waterfall hone. Figure 2-7-c displays the case when K is less than 1, indicating that S_α is larger than S_γ and the influence of the flank face is higher than that of the rake face. Also, the honed edge in this case is known as waterfall hone [8]. Denkena et al [41], investigated eight different combinations of edge radii, four of which were of symmetrically honed, two of which were of a reversed waterfall honed at $K = 1.5$, and the last two were of a waterfall honed with a $K = 0.5$. In all different cases S_α and S_γ varied between $20 \mu m$ to $60 \mu m$. Authors concluded that in terms of surface integrity, the observed tensile stresses on the machined workpiece material increase with increase of the ploughing zone size. These stresses are a combination between the experienced plastic-elastic deformation of the subsurface and the experienced thermal load. In addition, it was noted that as S_α increased the temperature in the cutting zone also increased.

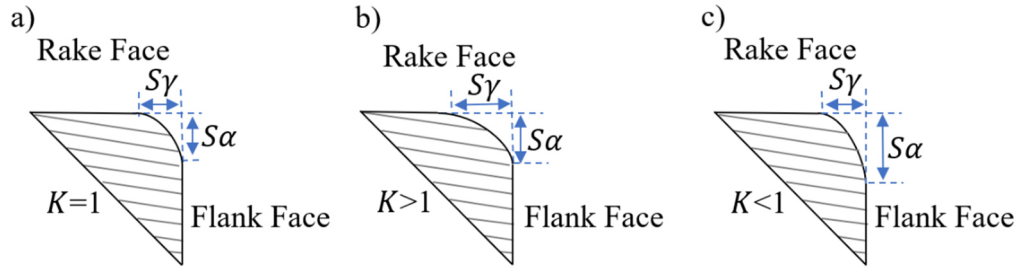


Figure 2-7: The Method of K Factor, (a) $K=1$, (b) $K>1$, and (c) $K<1$

Later, Wyen et al [42] examined the influence of cutting edge microgeometry on the surface integrity and burr formation during the up/down milling of Ti-6Al-4V titanium alloy. Multiple different cutting edge microgeometry radii were investigated, the smallest edge radius was $6\pm 2 \mu m$ and the largest edge radius was $50\pm 1 \mu m$. The research indicated that increasing the edge radius increases the residual stresses during both milling kinematics, due to the increase in mechanical deformation. Also, it was noted that increasing the edge radius increases the cutting temperature, because of its influence on the plastic deformation which is commonly accompanied by heat generation. Varying the edge radius presented no influence to slight influence on the microhardness and surface roughness during down/up milling. In addition, the visibility of feed marks and the size of the sub-surface deformation zone increase with the increase of cutting edge microgeometry. The influence of cutting edge microgeometry on tool life, generated forces, and the surface roughness when down milling ferrite-martensite stainless steel was considered during the works of Fulemova and Janda [43]. Tools were categorized based on their edge radius preparation method. Tools were prepared via grinding, drag finishing, and laser technology. Tools that utilized grinding and laser technology had an edge radius of $5 \mu m$, while tools that utilized drag finishing had an edge radius of $5 \mu m$, $10 \mu m$, and $15 \mu m$. Their results indicated that the surface roughness decrease with the increase of edge radius, which is linked with decreasing the tool wear. Additionally, authors indicated that the sharper the edge radius the easier it is for the

tool to penetrate through the workpiece. Therefore, initially generated forces decreased with the decrease of the edge radius. However, interestingly when the lowest and the highest edge radii inserts were compared after removing a 6 cm^3 of workpiece material, it was noted that the $15 \mu\text{m}$ radius insert had better surface roughness. This is contributed to the less tool wear the higher edge radius tools experience. Thus, surface roughness increased with the increase of tool wear. The edge preparation method impacted the tool wear as well. The dragged finished tool displayed the highest tool life while the laser treated tools displayed the lowest tool life. This is mainly due to error in the setup for the laser treatment process. Such errors occur because of the complexity of the laser setup process. The impact of edge honed radii uncoated cutting inserts on cutting forces, surface integrity, and surface oxidation, was investigated by Li et al [44], during the milling of an AISI H13 steel of a hardness of $50 \pm 1 \text{ HRC}$. Multiple edge radii were analyzed and were $5 \mu\text{m}$, $30 \mu\text{m}$, $60 \mu\text{m}$, $90 \mu\text{m}$, and $120 \mu\text{m}$. The paper noted that both cutting and feed forces increased with increase of edge radius. The connection between forces and edge radius is reasoned to the increase in the contact area between the hone and the workpiece material, as well as the experienced plowing actions. Therefore, these factors cause the friction and cutting forces to increase. The works highlighted similar point that was emphasized in the research presented in [43], in which over time forces may increase with the lower edge radius inserts. Mainly, due to the higher tool wear lower edge radii inserts experience. Similarly, inserts with larger edge radius display higher surface roughness measurements, with the exception for the $30 \mu\text{m}$ insert. This exception may be due to the lower vibrations that this edge radius size produce. In addition, the increase of surface roughness measurements with the increase of edge radius is reasoned to the plowing effects of the flank face that generates a material side flow. Moreover, the depth of the deformation layer in the machined sub-surface increases with the increase of edge radius, because of the higher friction,

temperature, shearing action, and plowing effects that larger honed edge radii inserts produce. Li et al [44], mentioned that compressive stresses were presented during the machining, and stresses increase with the increase of edge radius, due to the generated microcracks on the surface.

2-5 Summary

Majority of the available FEA machining models were either orthogonal 2D or 3D turning models. Additionally, the available reviewed 3D milling models either externally imported solid cutting tools, and/or created geometrically simple milling inserts and/or utilized software that did not give users broad control over the inputs of models, which in terms impacted the results of the models. Therefore, this thesis presents a Lagrangian-based 3D milling model that utilized the actual complex geometry of the widely used indexable inserts. ABAQUS/Explicit™ (version 2020) was utilized to develop the proposed model. The model was able to simulate cutting forces and generated chips during the hard milling of AISI 4340 steel. The model was validated in terms of cutting forces and generated chip morphology, by comparing its results against experimental tests of the same geometrical and cutting conditions. Cutting forces have a significant impact on the machine's power consumption, workpiece surface quality, tool wear, etc. Thus, the validation of cutting forces is considered an essential condition that must be satisfied during the development of FEA models. Majority of the referenced works in this chapter have validated their numerical models by at least comparing the data of the generated numerical forces against that of the captured experimental forces. Also, the work presented in this thesis attempts to thoroughly investigate the impact of cutting edge microgeometry while down milling AISI 4340 steel of 47 ± 1 HRC on the workpiece surface integrity. Because, the impact of cutting edge micro geometry of cutting inserts has not been widely explored in the literature specially for milling hardened steel with coated carbide inserts.

Chapter 3: Metal Cutting Simulations Using FEA

3-1 Preamble

Machining is a process in which a sharp wedge-shaped cutting tool removes the workpiece surface layers and converts it to the final product. Prediction and simulation of metal behavior during machining processes are complex tasks, due to multiple factors that are present within machining processes. These factors include high strains, high strain rates, and high temperatures. Numerical models are frequently implemented to model machining processes in a virtual environment to minimize the need for costly experimentations. Numerically developed FEA models can mimic complicated machining processes, by properly simulating their complex setup [21]. Additionally, FEA models present superiority in comparison to analytical models in terms of details of output results and understanding the behavior of workpiece materials during machining. FEA models enable the possibility of capturing multiple difficult to capture properties such as stress distribution, temperature distribution (within the tool, workpiece, chip and their interfaces), residual stresses, cutting forces, etc. [21]. Furthermore, tool designers utilize the knowledge gained from these models to optimally design and develop new cutting tools. Moreover, FEA models present their end users with a virtual tool that enables them to optimize material removal rate, power consumption and tool wear during machining [45]. The utilization of FEA models as virtual tools eliminates the need for costly and time consuming experimental tests [32].

3-2 Model Formulations

Formulations of numerical machining models are generally broken down into Lagrangian, Eulerian, and Arbitrary Lagrangian-Eulerian (ALE) formulations.

3-2-1 Lagrangian Formulation

In the Lagrangian formulation, movement of meshes is correlated to the movement of material and meshes are solved at discrete points of time. Also, mesh computation is integrated within the material domain of the analysis, which contributes to mesh distortion problems. Nonetheless, mesh distortion problems can be solved by using finer mesh sizes or employing adaptive meshing techniques. The Lagrangian formulation is commonly used to formulate numerical problems that simulate an unconstrained materials flow (e.g., machining). Therefore, Lagrangian formulation has the ability to predict chip shapes throughout the simulation, instead of the need to identify chip shapes prior to the start of the simulation. Identification of chip shapes at the start of the simulation requires prior knowledge of chip shapes, which necessitates conducting experimental tests to analyze the type of chips produced in reality.

3-2-2 Eulerian Formulation

In the Eulerian formulation, mesh computation is not integrated within the material domain. Instead the assigned meshes are fixed while the material flows through a controlled volume. This feature eliminates the problem of material distortion. Yet, the initial chip shape and material flow boundaries must be identified prior to the simulation. Because Eulerian formulation assumes that the operation initiates from a steady state condition, a separation criterion does not have to be defined. These assumptions impact the accuracy of the formulation in predicting processes outputs. In addition, Eulerian formulation mainly simulates continuous chips and cannot simulate serrated and/or discontinuous chips, due to its inability to adopt to the modeling of the unconstrained flow of material during chip formation.

3-2-3 ALE Formulation

The third type of formulation is the ALE formulation. This formulation combines the advantageous of Lagrangian and Eulerian formulations. Meshes remain of high quality during the analysis because mesh and material motions are independent. However, a mesh motion scheme must be identified during the simulation in order to maintain high quality meshes. Tracking the mesh motion during 3D FEA simulations is a challenging task due to the involved dimensionality. Figure 3-1 displays the ALE formulation as a combination of the Lagrangian and Eulerian formulations. Additionally, V is the cutting speed.

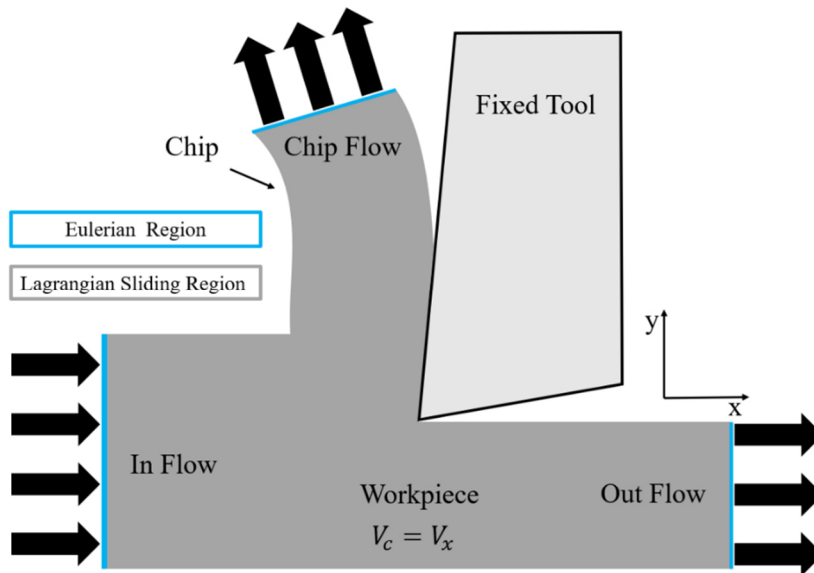


Figure 3-1: Boundary Conditions of ALE Formulation

3-3 Time Integration Schemes

In terms of time incrementation in finite element modeling, users employ either explicit or implicit analyses, based on the type/class of the investigated numerical problems. Explicit analysis is the preferred choice when solving dynamic nonlinear (high-speed), complex contact, complex post-buckling, nonlinear quasi-static and material with degradation/failure numerical problems. Implicit analysis is utilized for static linear/nonlinear, dynamic linear and dynamic nonlinear (low-

speed) numerical problems. Nonlinearity is evaluated in terms of material, geometry and contact. Nevertheless, there are numerical static and quasi-static problems that can be solved by either analysis. Therefore, a proper understanding of both analyses enables users to select the most appropriate analysis for their specific numerical problems. Implicit and explicit analyses share the same general dynamic equilibrium (i.e., steady state) equation as presented in equation (3-1).

$$M\ddot{u} = P - I \quad (3-1)$$

Where, M is the mass matrix, P is the external applied load, I is the internal forces of elements and \ddot{u} is the approximated nodal acceleration. The state of equilibrium of a system can be represented by equation (3-1). when the external applied load P is small enough to be negligible. Both analyses differ in their solution methodology for nodal accelerations predictions. Implicit analysis uses a direct solution method to solve a set of linear equations; thus, the nodal accelerations are solved iteratively. Explicit analysis integrates an explicit integration rule with a diagonal or lumped element mass matrix to solve for nodal accelerations directly at any given time.

3-3-1 Implicit Analysis

Implicit analysis generally solves numerical problems with small number of iterations. The unconditionally stable constraint of the implicit analysis allows the time integration scheme to have no limitation on the size of its time steps. Also, this constraint forces the analysis to always work towards converging to a solution. If convergence is achieved, the solution is considered to be very reliable. The implicit analysis solves a set of linear equation during each time step by utilizing the full Newton Iterative Solution method to solve for accelerations and displacements. Moreover, when numerical problems of high nonlinearity are solved, convergence issues might be experienced and, in some cases, convergence is not possible. Such difficulties result in increasing

the number of iterations and decreasing the size of time steps, which in turn significantly increases the computational time.

3-3-2 Explicit Analysis

Explicit FEA analysis solves numerical problems as wave propagation problems and it generates a conditionally stable numerical solution. Therefore, to ensure process stability and solution accuracy a critical time step parameter is set. Thus, the analysis time step must be lower than the critical time step. The critical time step $\Delta t_{critical}$ is represented by equation(3-2) [21]; where, L_{e0} is initial length of the element, E the Young's Modulus, ν is Poisson's ratio, and ρ is the density of the workpiece material.

The proposed model in this work utilizes the explicit option of ABAQUS™ software, namely: ABAQUS/Explicit. The adopted explicit analysis does not require iterations and/or stiffness matrix. In order to conduct its explicit dynamic analysis, the solver integrates an explicit integration rule with a diagonal or lumped element mass matrix. The central difference method (i.e., Forward Euler) is the integration rule utilized by ABAQUS/Explicit. The explicit solution at the end of each time step is exclusively based on displacements, velocities, and accelerations gathered at the beginning of each time step. The iteration procedure of ABAQUS/Explicit of a single time step is broken down into three steps: nodal calculations, elements calculations, and time advancements. The nodal calculation involves the following sub-steps: (a) solving the general dynamic equation presented in equation (3-1), (b) calculating the acceleration of the current time step using equation (3-3), (c) calculating the change of velocity by assuming the acceleration is constant. The velocity is estimated by equation (3-4) where \dot{u} is the velocity, Δt is the time increment, and t is the current incremental time. Step (d) is calculating the displacement at the end

of the increment by utilizing the calculated change in velocity in step (c) as presented by equation (3-5) where u is the displacement.

$$\Delta t_{critical} = \frac{L_{e0}}{\sqrt{\frac{E}{\rho(1+\nu)}}} \quad (3-2)$$

$$\ddot{u}|_{(t)} = M^{-1}(P - I)|_{(t)} \quad (3-3)$$

$$\dot{u}|_{(t+\frac{\Delta t}{2})} = \dot{u}|_{(t-\frac{\Delta t}{2})} + \frac{\Delta t|_{(t+\Delta t)} + \Delta t|_{(t)}}{2} \ddot{u}|_{(t)} \quad (3-4)$$

$$u|_{(t+\Delta t)} = u|_{(t)} + \Delta t|_{(t+\Delta t)} \dot{u}|_{(t+\Delta t)} \quad (3-5)$$

The second main step is the elements calculation and it is the most computationally expensive step. Also, in this step, incremental strains of elements are calculated from their strain rates. Then, material constitutive equations are applied to calculate the elements experienced stresses, which enables the solver to solve for internal forces. Lastly, the time advancing step is performed to advance the solution into the next iteration. ABAQUS/Explicit time incrementation scheme is an automated process and it does not require user interference.

3-4 Workpiece Material Models

An accurate representation of the workpiece material during the developments of FEA models greatly impact the results of models. Workpiece material models are proposed as constitutive equations that are able to represent the instantaneous flow stress of materials during FEA simulations. Due to the complex nature of cutting processes, material flow stresses depends on the strains, strains rates and temperatures experienced by the workpiece during machining. Most

commonly utilized material constitutive equations in machining simulations are J-C (strength) and Zerilli-Armstrong.

3-4-1 J-C Strength Material Model

In 1983, Gordon R. Johnson and William H. Cook proposed a constitutive material model, which is widely known as Johnson-Cook strength model. The model has the ability to represent the behavior of a material subjected to high strains, high strain rates, and high temperatures [46]. It expresses the behavior of a material during its deformation process by calculating its von Mises flow stress (σ) as shown in equation (3-6).

$$\sigma = [A + B\varepsilon^n][1 + C \ln(\dot{\varepsilon}^*)][1 - T^{*m}] \quad (3-6)$$

As can be seen, J-C model contains five constants A , B , C , n and m . Constants are obtained experimentally from torsion tests, static tensile tests, and dynamic Hopkinson bar tensile tests. Tests are conducted over a wide range of strain rates and temperatures. J-C strength model is a general material model; however, it is commonly used in FEA models of machining operations. This is due to the J-C model ability to represent the flow stress of workpiece material by taking strains, strain rates, and temperatures into consideration. Various J-C strength model constants for the same material have been proposed in the literature, because constants vary based on their derived testing conditions. Therefore, the reliability of proposed constants in simulating the material behavior during machining highly depends on the proximity between the strains, strain rates and temperatures during the experimentations for obtaining the constants, and the strains, strain rates and temperatures during the investigated machining operation. As can be seen, equation (3-6) consists of three main terms that represent strain, strain rate, and temperature experienced by the workpiece during machining.

Chapter 3: Metal Cutting Simulations Using FEA

The first term in equation (3-6) is $[A + B\varepsilon^n]$, it consists of four parameters: A , B , ε , and n . A and B are constants in MPa and they represent the yield stress and strength coefficient of the workpiece material, respectively. ε is the equivalent plastic strain and it expresses the plastic deformation the material experiences. n is strain hardening exponent and it is a dimensionless constant.

A quasi-static strain test at a referenced temperature is required to calculate the constant A . This approach would eliminate the second and third terms of equation (3-6) as shown by equation (3-7). The second terms of equation (3-6) would be eliminated because $\dot{\varepsilon} = \dot{\varepsilon}_0$ and the third term of equation (3-6) would be eliminated because $T = T_{Reference}$.

$$\sigma = [A + B\varepsilon^n] \tag{3-7}$$

Two steps are required to obtain A . Steps must be executed as follows: (a) obtaining the engineering stress-strain curve of the material and (b) The 0.2% strain offset approach must be considered knowing A is the yield stress of the material. Therefore, the engineering strain along the x -axis would change into a percentage form. Then, a parallel line to the elastic region line of the engineering stress-strain curve must be constructed starting from the 0.2% point of the x -axis. The intersection of the drawn line and the engineering stress-strain curve is the equal to the constant A . Figure 3-2 illustrates steps (a) and (b) of acquiring the constant. The UTS point in Figure 3-2 stands for the ultimate tensile strength, which is the maximum stress a material can withstand prior to fracture.

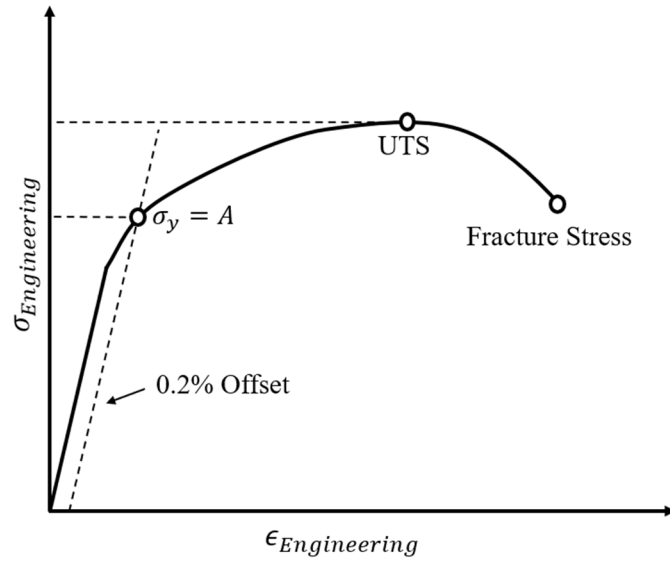


Figure 3-2: Engineering Stress-Strain Curve

A quasi-static strain test at a referenced temperature is also required to calculate constants B and n . Two steps are involved to obtain these constants. (a), obtaining the true stress-true strain curve of the material. (b), constructing a graph where the y -axis is equal to equation (3-8) and the x -axis is equal to equation (3-9).

$$Y - axis = \ln(\sigma - A) \quad (3-8)$$

$$X - axis = \ln(\epsilon) \quad (3-9)$$

Then, based on the given data, a fitted line is constructed as displayed by equation (3-10). The slope of equation (3-10) equal to the constant n and the intercept is equal to natural logarithmic of the constant B , $\ln(B)$. Figure 3-3 (a) and (b) illustrates the required steps to obtain constants B and n .

$$\ln(\sigma - A) = n \ln(\epsilon) + \ln(B) \quad (3-10)$$

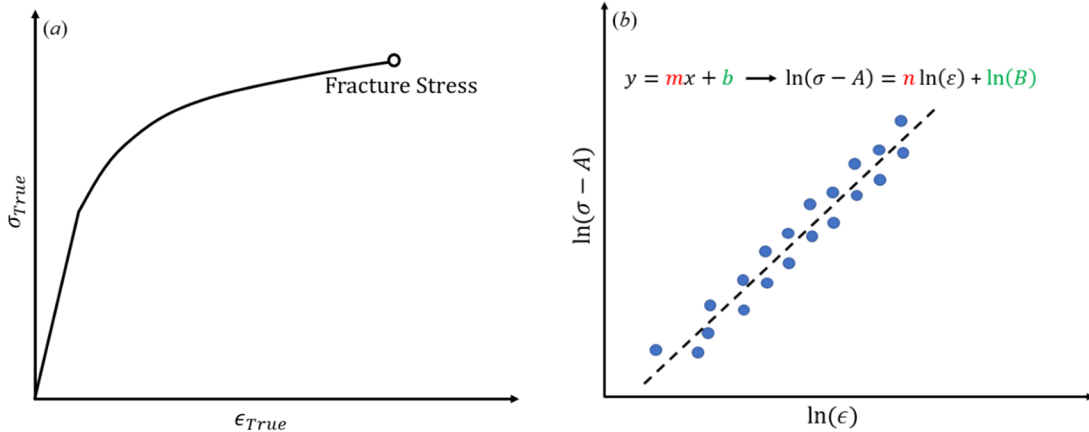


Figure 3-3: Steps Required to Obtain Constants B and n

The second term in equation (3-6) is $[1 + C \ln(\dot{\epsilon}^*)]$. This term represents the strain rate experienced by the material. It consists of two main parameters which are the dimensionless plastic strain rate $\dot{\epsilon}^*$ and the constant C . Equation (3-11) indicates that $\dot{\epsilon}^*$ is calculated in terms of $\dot{\epsilon}$ and $\dot{\epsilon}_0$ where $\dot{\epsilon}$ is the plastic strain rate. This parameter is constantly updated during the simulation and given per unit of time s^{-1} . $\dot{\epsilon}_0$ is the referenced strain rate and it remains unchanged during the simulation. C is the strain sensitivity parameter constant and it is acquired experimentally.

$$\dot{\epsilon}^* = \frac{\dot{\epsilon}}{\dot{\epsilon}_0} \quad (3-11)$$

Various high strain rates tests at a referenced temperature are required to calculate the constant C . This approach would eliminate the thermal softening term of equation (3-6). The third term of equation (3-6) is eliminated when $T = T_{Reference}$. Thus, equation (3-6) would be simplified as shown by equation (3-12).

$$\sigma = [A + B\varepsilon^n][1 + C\ln(\dot{\varepsilon}^*)] \quad (3-12)$$

Four steps are required to derive the constant C . (a), conducting multiple high strain rates tests, while maintaining the same testing temperature (referenced temperature). (b), constructing true stress – true strain graph from the conducted tests. (c), formulating a graph on the basis of assuming the approximate relationship displayed by equation (3-13) is valid. The y -axis of the graph is given by equation (3-14) and the x -axis is presented by equation (3-15).

$$\frac{\sigma}{[A + B\varepsilon^n]} \sim \ln(\dot{\varepsilon}^*) \quad (3-13)$$

$$Y - axis = \frac{\sigma}{[A + B\varepsilon^n]} \quad (3-14)$$

$$X - axis = \ln(\dot{\varepsilon}^*) \quad (3-15)$$

(d), rearranging equation (3-6) in a form that allows the constant C to be the slope of the equation as shown by the rearranged equation (3-16). Steps (b-d) of obtaining the constant C are presented in Figure 3-4.

$$\frac{\sigma}{[A + B\varepsilon^n]} = [C\ln(\dot{\varepsilon}^*) + 1] \quad (3-16)$$

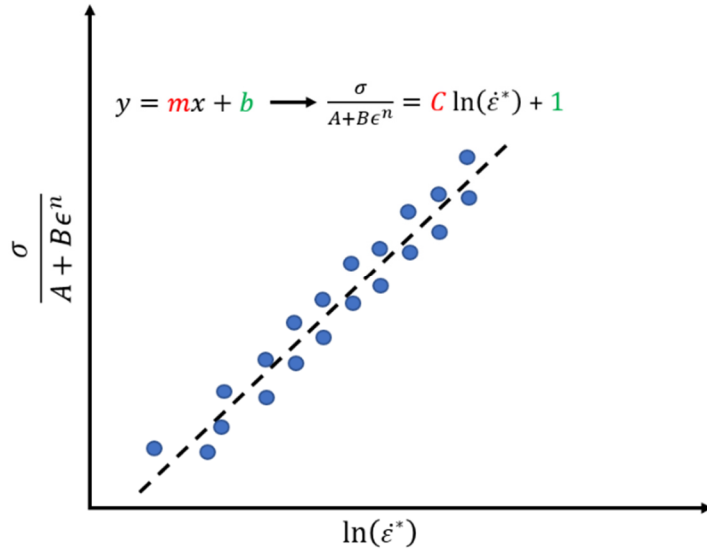


Figure 3-4: Steps to Calculate Contact C

Another approach to calculate the constant C can be conducted through the following three steps. (a) conducting multiple high strain rates tests at the same temperature (referenced temperature). (b) The values of the flow stress σ and the true strain ϵ must be taken at the initial yield point for each of the high strain rates tests. This approach will lower the impact of the thermal softening of the material. Subsequently, equation (3-6) is rearranged without the thermal softening term to solve for C as shown by equation (3-17). (c) The strain rate constant C would be equal to the mean value of all obtained strain rate constants from the multiple high strain rate tests $\bar{C}_{Of\ All\ High\ Strain\ Tests}$ as displayed by equation (3-18). In equation (3-18) j is the number of obtained constants C .

$$C = \frac{\frac{\sigma}{[A + B\epsilon^n]} - 1}{\ln(\dot{\epsilon}^*)} \quad (3-17)$$

$$C = \bar{C}_{Of\ All\ High\ Strain\ Tests} = \frac{\sum_{i=1}^j C_i}{j} \quad (3-18)$$

Chapter 3: Metal Cutting Simulations Using FEA

The third term in equation (3-6) is $[1 - T^{*m}]$. Two parameters are included in this term; the dimensionless homologous temperature T^* and the experimentally obtained thermal sensitivity constant m . Equation (3-19) illustrates that the homologous temperature is calculated based on three parameters, the materials temperature during the simulation T , referenced temperature $T_{Reference}$ (in this work $T_{Reference} = 20\text{ }^\circ\text{C}$), and the melting temperature of the material $T_{Melting}$. $T_{Reference}$, remains constant during the simulation and its purpose is to cause the third term of equation (3-6) to be equal to unity, which is required to calculate the other constants of equation (3-6).

$$T^* = \frac{T - T_{Reference}}{T_{Melting} - T_{Reference}} \quad (3-19)$$

Quasi-static strain tests at various high temperatures are required to obtain the thermal sensitivity constant m . The approach will eliminate the second term in equation (3-6), as displayed by equation (3-20). The second term of equation (3-6) is eliminated because the quasi-static strain condition cause $\dot{\epsilon}$ to equal to the $\dot{\epsilon}_0$.

$$\sigma = [A + B\epsilon^n][1 - T^{*m}] \quad (3-20)$$

Four main steps are involved to obtain the constant m . (a) conducting multiple high temperature tests at constant strain rates (referenced strain rate), (b) constructing true stress – true strain graph from the conducted tests, and (c) formulating a graph in which the y -axis is equal to equation (3-21) and the x -axis is equal to equation (3-22).

$$Y - axis = \ln\left(1 - \frac{\sigma}{[A + B\varepsilon^n]}\right) \quad (3-21)$$

$$X - axis = \ln(T^*) \quad (3-22)$$

In step (d), based on the given data, a fitted line is constructed as presented by equation (3-23)-(ii). The analytical derivation of the fitted line is presented by steps (i) and (ii) of equation (3-23). The slope of the derived fitted line is equal to the constant m . Steps b to d to obtain the constant m are displayed in Figure 3-5.

$$\left(1 - \frac{\sigma}{[A + B\varepsilon^n]}\right) = T^{*m} \quad (i)$$

$$\ln\left(1 - \frac{\sigma}{[A + B\varepsilon^n]}\right) = m \ln(T^*) \quad (ii) \quad (3-23)$$

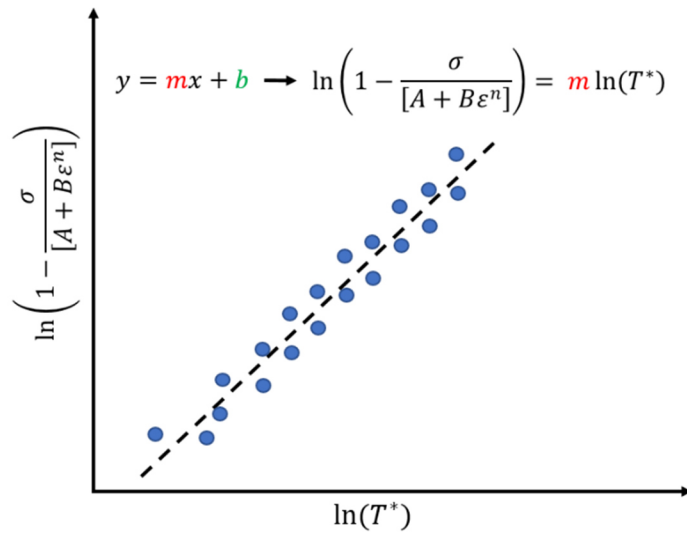


Figure 3-5: Steps Required to Calculate Contact m

Constant m can also be obtained by following the next three steps. (a) conducting multiple high temperature tests at the same strain rate (referenced strain rate). (b) The values of the flow stress σ and the true strain ε must be taken at the initial yield point for each of the high temperature

tests. Next, equation (3-6) is rearranged without the strain rate term to solve for m as shown by equation (3-24). (c) deriving the thermal sensitivity constant m , which equals to the mean value of all obtained thermal sensitives constants from the various temperatures tests $\overline{m}_{of\ All\ Different\ Temperatures\ Tests}$ as displayed by equation (3-25). In equation (3-25) h is the number of obtained constants.

$$m = \frac{\ln\left(1 - \frac{\sigma}{[A + B\varepsilon^n]}\right)}{\ln(T^*)} \quad (3-24)$$

$$m = \overline{m}_{of\ All\ Different\ Temperatures\ Tests} = \frac{\sum_{i=1}^h m_i}{h} \quad (3-25)$$

3-4-2 Zerilli-Armstrong Material Model

Frank J. Zerilli and Ronald W. Armstrong proposed two constitutive material equations in 1987 [47]. Proposed equations were for materials of Face Centered Cubic (FCC) and Body Centered Cubic (BCC) crystalline structures. Two equations were developed for each crystalline structure-based material, because of the notable response difference these materials exhibit under high strain rates and temperatures. Equations (3-26) and (3-27) present Zerilli-Armstrong's BCC and FCC materials based crystalline structures flow stress equations, respectively. The main difference between both equations is the strain parameter. In equation (3-26) the impact of the strain parameter on the flow stress is independent of the temperature and the strain rate. In equation (3-27) impacts of the strain, strain rate, and temperature are combined in single term (second term). C_0 is a stress parameter that considers the dislocation density on the flow stress, $C_1 - C_5$ and n are material constants, and T is the absolute temperature.

$$\sigma = C_0 + C_1 e^{\left(-C_3 T + C_4 T \ln\left(\frac{\dot{\epsilon}}{\dot{\epsilon}_0}\right)\right)} + C_5 \epsilon^{n_{ZA}} \quad (3-26)$$

$$\sigma = C_0 + C_2 \epsilon^{-\left(\frac{1}{2}\right)} e^{-C_3 T + C_4 T \ln\left(\frac{\dot{\epsilon}}{\dot{\epsilon}_0}\right)} \quad (3-27)$$

3-5 Chip Generation

Numerical chip generation is an important parameter that is used to validate numerical models. The validation is conducted by comparing numerical/experimental chip shapes, chip geometries, or both chip shapes/geometries. During machining, chips are typically generated as continuous, serrated (saw-toothed), and discontinuous. Type of chips depends on workpiece material, cutting tool geometry, cutting conditions, etc. Numerically simulated chips are generated based on the nodal separation method or the element deletion method.

Nodal separation is a geometrical based method. Separation occurs along a pre-defined parting line as shown in Figure 3-6 (a) and (b). Figure 3-6 (a) presents the tool and workpiece prior to nodal separation while Figure 3-6 (b) displays the tool and workpiece after nodal separation. Figure 3-6 (a) and (b) consist of a cutting tool, two four noded elements and a parting line. The parting line goes through both elements representing the nodes separation location. Separation occurs when distance D along the parting line between the cutting tool and the nodes is smaller or equal than a set critical distance $D_{critical}$. Which, is the minimum distance that when reached elements begin to separate.

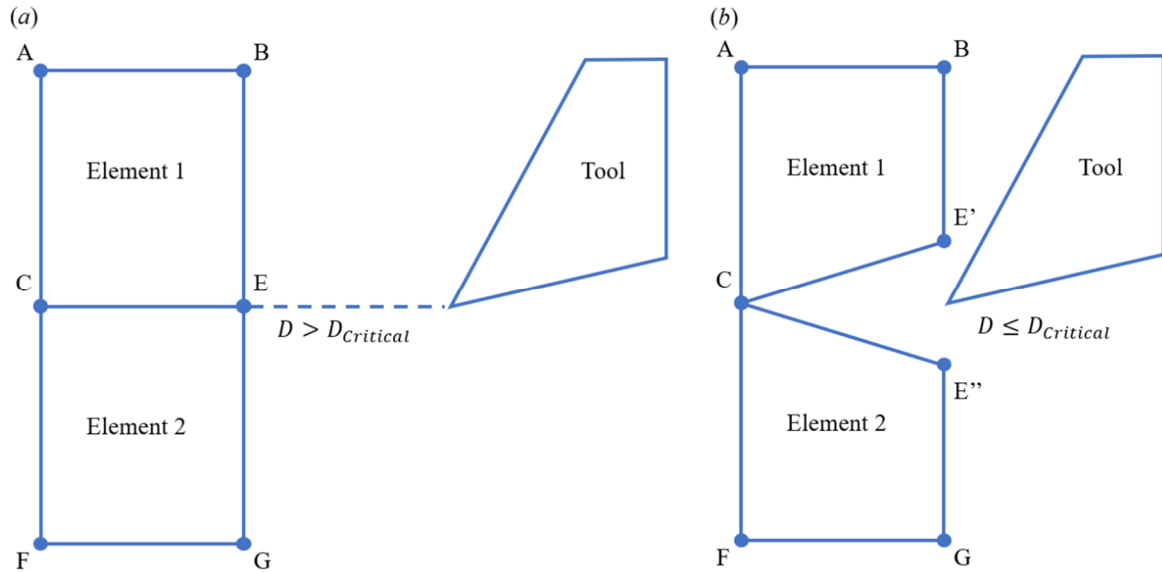


Figure 3-6: Nodal Separation Method

Element deletion method is based on the workpiece material properties. Workpiece elements are assigned critical damage evaluation parameters. Parameters are either energy based or displacement based. In the energy-based technique, an element is deleted when its maximum energy dissipation per unit area exceeds the set limits. Similarly, in the displacement-based technique, an element is deleted when its maximum plastic displacement distance exceeds the set displacement limits. Moreover, in specific cases depending on the kinematics/dimensionality of the developed FEA model, a thin partition area may be defined to enhance the ability of the model to generate a chip as shown in Figure 3-7. The partition tends to be extremely thin. Thus, its deletion does not impact the accuracy of the results. However, creating a partition in 3D FEA milling models is not convenient, and thus has not been investigated widely, due to variations of chip thickness throughout the cut.

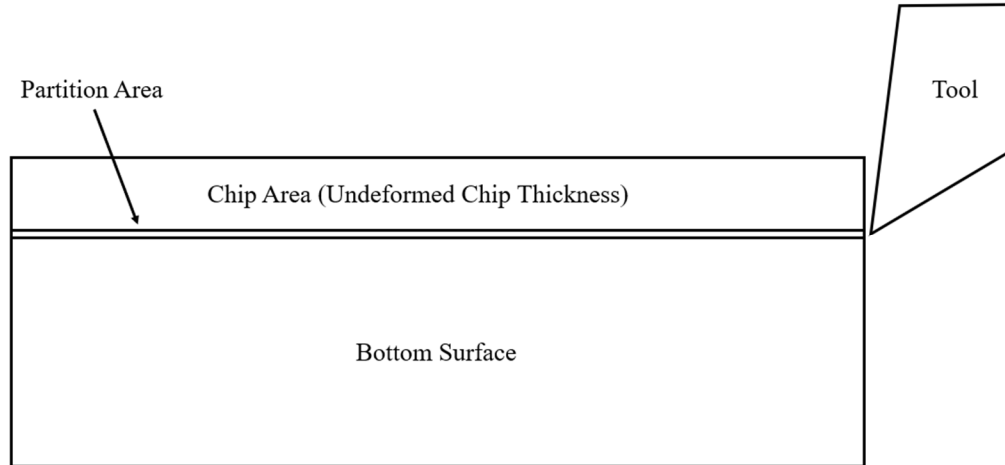


Figure 3-7: Element Deletion Method

3-6 Workpiece Damage Model

Materials fracture characteristics are taken into account when the J-C fracture model is applied [48]. Employing J-C fracture model decreases the computational time of the simulation, by enabling users to use coarser mesh sizes. In addition, when J-C fracture model is used, the initial chip shape does not need to be identified, which allows the FEA software to generate chips based on the input parameters. Chip formation occurs during two stages because of shear deformation. The first stage is elements failure initiation and the second stage is elements failure progression.

Equation (3-28) presents the damage initiation scalar parameter w of the elements. Damage is initiated when $w = 1$. The damage initiation parameter w is equal to the division of summation of the equivalent plastic strain $\Delta\varepsilon$ and the equivalent fracture strain ε^f . $\Delta\varepsilon$ is calculated during the numerical simulation. ε^f is presented by equation (3-29) and considers the stress triaxiality ratio, the strain rate, and the temperature.

$$w = \sum \frac{\Delta\varepsilon}{\varepsilon^f} \quad (3-28)$$

$$\varepsilon^f = [D_1 + D_2 e^{D_3 \sigma^*}][1 + D_4 \dot{\varepsilon}^*][1 + D_5 T^*] \quad (3-29)$$

The first term in equation (3-29) is the stress triaxiality term and it consists of D_1, D_2, D_3 , and σ^* . The first three parameters are experimentally obtained constants. σ^* , is the dimensionless stress triaxiality parameter, and $\sigma^* \leq 1.5$. The analytical representation of σ^* is presented in equation (3-30) and it is equal to the division of the average of the three normal stresses σ_m to the von Mises flow stress σ . Furthermore, researchers have attempted to calculate the stress triaxiality in different approaches such as Bridgman's stress triaxiality equation, which is presented by equation (3-31) [49]. In equation (3-31), R in mm is the radius of the necked region and a in mm is the minimum cross-sectional area of the tested specimen. Description of the specimen at the necking region is shown in Figure 3-8.

$$\sigma^* = \frac{\sigma_m}{\sigma} \quad (3-30)$$

$$\sigma^* = 0.3 \ln \left(1 + \left(\frac{a}{2R} \right) \right) \quad (3-31)$$

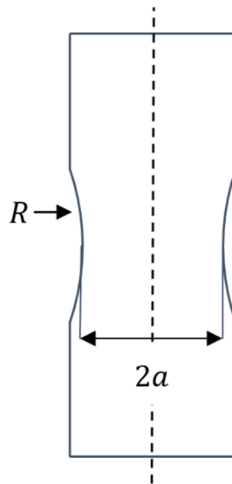


Figure 3-8: Specimen at the Necked Region

A combination of quasi-static strain tests at a referenced temperature and specimens of various notch geometries must be conducted to derive D_1, D_2 and D_3 . Quasi-static strain tests at a referenced temperature would eliminate the second and third terms of equation (3-29). To obtain the first three constants, a graph must be created, where the x -axis is equal to the strain at fracture and the y -axis is equal to the stress triaxiality. The strain at fracture is measured by the true strain equation. The initial area of the specimen is the pre-fractured area and the final area is the area of the specimens after fractured has occurred. To calculate the area of the fractured specimen, the separated parts of the fractured specimens must be put back together. Then a microscope must be used to measure the cross-sectional area of the fractured specimen. The stress triaxiality is calculated by equation (3-31). Having multiple strain at fracture values and multiple stress triaxiality values would allow users to calculate the unknown constants by utilizing the available system of equations.

The second term in equation (3-29) is the equivalent strain term and it consists of dimensionless plastic strain rate $\dot{\epsilon}^*$ and the exponentially obtained constant D_4 . Calculation of $\dot{\epsilon}^*$ in J-C fracture model is similar to calculating $\dot{\epsilon}^*$ in the J-C strength model. The strain rate constant D_4 is conducted in a similar way as the constant C of the J-C strength model. However, the plot for the constant is mainly focused on the area in which fracture initiates.

The third term in equation (3-29) is the temperature term and it consists of the homologous temperature T^* and the exponentially acquired constant D_5 . Calculation of T^* in J-C fracture model is also similar to calculating T^* in the J-C strength model. The constant D_5 is conducted in a similar way as the constant thermal sensitivity constant m of the J-C strength model. Nonetheless, the plot for D_5 is mainly focused on the area in which fracture initiates.

Equation (3-32) presents the standard damage law, which describes damage evaluation of elements from damage initiation up-to complete failure. An element reaches a complete state of failure when its damage parameter D equals to unity $D = 1$. The damage parameter D is represented in terms of L , $\bar{\epsilon}^{pl}$, \bar{u}^{pl} and \bar{u}_f^{pl} , which are the characteristic length, equivalent plastic strain, equivalent plastic displacement and equivalent plastic displacement at failure, respectively.

$$D = \frac{L\bar{\epsilon}^{pl}}{\bar{u}_f^{pl}} = \frac{\bar{u}^{pl}}{\bar{u}_f^{pl}} \quad (3-32)$$

The material stiffness of an element degrades with the progression of its damage. This damage progression is described by a damage evaluation criterion. Damage degradation curve of a ductile material is presented in Figure 3-9. Damage degradation curve describes the stress-strain behavior of material experiencing damage. σ , ϵ , σ_y , σ_{y0} , $\bar{\epsilon}_0^{pl}$, and $\bar{\epsilon}_f^{pl}$ are the stress, plastic strain, yield stress, yield stress at the onset damage, equivalent plastic strain at the onset damage, and equivalent plastic strain at failure. Two curves are presented in Figure 3-9. A solid curve representing the material response under damage and dashed curve representing material response under the absence of damage. Stages 1-2 of the solid curve displays the linear elastic behavior of material. Then, through stages 2-3 material begins to experience plastic yielding and strain hardening. During stages 3-4 is when material begins to experience damage and ultimately failure. At stage 3 damage is initiated $w = 1$. At 4 failure is reached and complete damage is achieved at $D = 1$. The degraded strength of a material along the curve is calculated by equation (3-33), where $\bar{\sigma}$ is the undamaged stress response.

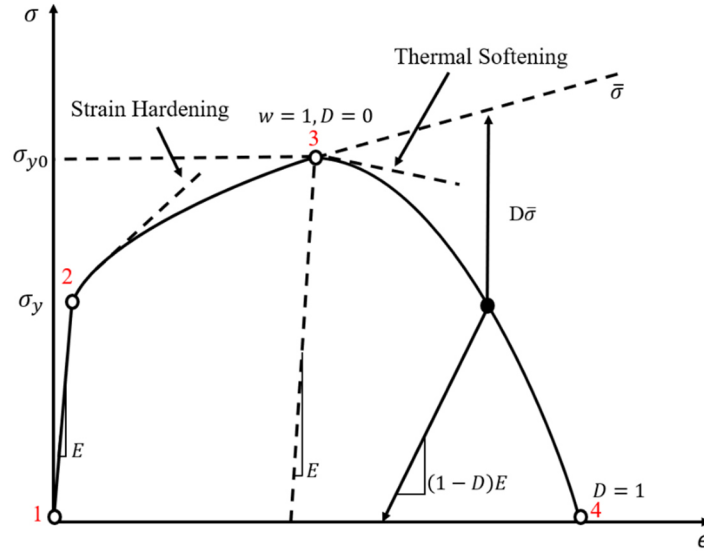


Figure 3-9: Stress Strain Curve for Materials Experiencing Progressive Damage Evolution

$$\sigma = (1 - D) \bar{\sigma} \quad (3-33)$$

General stress-strain relationship is an invalid tool to use to predict the behavior of a ductile material when it experiences damage, especially when coarse meshes are used. Because, utilization of stress-strain relationship presents a strong mesh reliance, which is based on strain localization. This phenomenon results in decreasing energy dissipation, when meshes are decreased in size. Therefore, two methods can be used to evaluate the damage experienced by materials namely fracture energy dissipation per unit area G_f and equivalent plastic displacement \bar{u}^{pl} . Both methods are utilized to ensure mesh dependency of the model is minimized. Hillerborg et al. [50] fracture energy model is used to calculate the fracture energy. This is the energy required to open a unit area of a crack, G_f is presented by equation (3-34). The fracture energy can also be calculated by equation (3-35), where K_c is the fracture toughness. Fracture toughness is commonly used to present the ability of a material to resist crack growth. However, this parameter can also be used to predict the initiation of fracture.

$$G_f = \int_{\bar{\epsilon}_0^{pl}}^{\bar{\epsilon}_f^{pl}} L_e \sigma_y \bar{\epsilon}^{pl} = \int_0^{\bar{u}_f^{pl}} \sigma_y d\bar{u}^{pl} \quad (3-34)$$

$$G_f = \left(\frac{1 - \nu^2}{E} \right) k_c^2 \quad (3-35)$$

The equivalent plastic displacement of an element after damage initiation is calculated in terms of equivalent plastic strain at the onset damage and the characteristic length of an element L_e , as shown in equation (3-36).

$$\bar{u}^{pl} = L_e \bar{\epsilon}^{pl} \quad (3-36)$$

Prior to damage initiation, $\bar{u}^{pl} = 0$. An element will fail when $\bar{u}^{pl} = \bar{u}_f^{pl}$. Also, instantaneous failure will occur when $\bar{u}_f^{pl} = 0$. The equivalent plastic displacement method was utilized in this model to evaluate the damage experienced by the workpiece elements. The value for \bar{u}_f^{pl} was modified until a good agreement between numerical cutting forces and generated chips and experimental captured forces and collected chips was established.

3-7 Friction Models

Numerical machining simulations require friction models between the cutting tool and the workpiece material to be properly and thoroughly selected as friction models impact the tool-chip contact length, chips shapes/geometries, cutting temperatures, and cutting forces. Most commonly used friction models in machining simulations are Coulomb Friction Law, Constant Shear Friction, and Stick-Slip Friction models.

3-7-1 Coulomb Friction Law Model

Coulomb's friction law model is considered to be one of the first models that represents the contact between two bodies. The model is considered to be simplistic in comparison to other friction models, because the contact between the cutting tool and the workpiece material is assumed to occur over a single region. Analytically, the model is presented by equation (3-37). The model consists of three terms: τ , σ_n , and μ , which represent the shear stress, normal stress, and Coulomb's friction coefficient, respectively.

$$\tau = \mu\sigma_n \quad (3-37)$$

3-7-2 Constant Shear Friction Model

The constant shear friction model assumes that frictional stress is constant along the rake face of cutting tool. The model is represented mathematically by equation (3-38) and it consists of three terms: τ , m_s , and k_s , which represent the shear stress, constant shear friction factor, and shear flow stress of the workpiece material, respectively.

$$\tau = mk \quad (3-38)$$

3-7-3 Stick-Slip Friction Model

The developed model in this work uses the widely used stick-slip friction model, developed by Zorev [51] in 1963. The stick-slip friction model divides the tool-chip contact length into two regions. Namely sticking and sliding regions. Within the sticking region the shear stress and the critical frictional stress are equal. Also, the shear stress is assumed to be constant within the sticking region. Within the sliding region, the shear stress and the normal stress are proportional. Also, the Coulomb friction law is adopted within the sliding region [31]. The contact is presented analytically in equation (3-39). Equation (3-39) consists of four terms τ , τ_{max} , σ_n , and μ which

represent the shear stress, maximum shear stress, normal stress, and Coulomb's friction coefficient, respectively. L_c is the tool-chip contact length. μ is equal to the ratio between the force in the parallel direction to the rake face of the cutting insert to the force in the normal direction to the rake face. In addition, μ is assumed to be constant along the rake face of the cutting insert and it is obtained experimentally with values ranging between 0.2-1.8 [52]. In this work $\mu = 0.3$.

$$\begin{aligned} \tau &= \tau_{max} & 0 \leq Length \leq L_c & & \text{When, } \mu\sigma_n \geq \tau_{max} \\ \tau &= \mu\sigma_n & 0 \leq Length \leq L_c & & \text{When, } \mu\sigma_n < \tau_{max} \end{aligned} \quad (3-39)$$

3-8 FE Software Packages

The three most commonly used FEA solvers for modeling machining operations are: ABAQUS™, AdvantEdge™, and DEFROM® [16]. These software packages offer different features which may be considered advantageous or disadvantageous based on the investigated numerical problem. A characterization summary of the aforementioned solvers was presented by Rodríguez et al. [53]. FEA packages were characterized in terms of creation of geometries/importing CAD data, material catalogue, element types, time integration schemes, remeshing routines, usage (field), access to the modules code, and parallelization availability.

In terms of creation of geometries/importing CAD data, ABAQUS™ allows its users to design a wide range of complex geometries, and that is the case for metal cutting tools. AdvantEdge™ and DEFROM® allow for designing simple geometries only. All three software allow for importing CAD data from external sources. In regards of material catalogue, ABAQUS™ allows its users to input their specific material properties within their models. DEFROM® and AdvantEdge™ has their own material library and allow their users to import data for investigated materials as well. Defining material properties in FEA models is a sensitive step because inputting incorrect

properties would result in inaccurate results. ABAQUS™ grants its users the ability to utilize every element type enhancing the ability of the solver to deal with complex numerical problems. In this context, AdvantEdge™ and DEFROM® only permit the usage of tetrahedron and rectangular elements. Implicit and explicit time integration options are also available in ABAQUS™. AdvantEdge™ allows its users to only use explicit time integration schemes, while implicit analysis are the only time integration schemes available in DEFROM®. AdvantEdge™ and DEFROM® allow their users to use remeshing routines while ABAQUS™ does not, which contributes to mesh distortion problems that ABAQUS™ models may experience. However, to overcome this issue, ABAQUS™ allows for adaptive meshing. In terms of fields of application. ABAQUS™ is a general-purpose FEA solver, while AdvantEdge™ and DEFROM® are mainly used for cutting and deformation operations, respectively. ABAQUS™ and DEFROM® solvers allow their users to access their modules code and manipulate certain settings to improve the efficiency of the process; while AdvantEdge™ does not. Finally, all three solvers allow their users to utilize parallelization, which improves the computational time.

3-9 Summary

In this chapter, methodologies of constructing FE models in machining were discussed. Topics were broken down into: formulation types, time integration schemes, material models, chip generation techniques, J-C fracture model, friction models, and widely used FEA packages. Discussed topics in this chapter make up the foundations for the development of the FEA model presented later in the thesis. Steps to develop the model via ABAQUS/Explicit are presented in chapter 4. Additionally, chapter 4 contains the experimental validation of the model and an in-depth discussion of the generated results. Comparative summaries of time integration schemes and commonly utilized FE software are presented in Table 3-1 and Table 3-2, respectively.

Table 3-1: Comparison Between Explicit and Implicit Time Integration Schemes

Feature	Explicit	Implicit
Stability of Solution	Conditional	Unconditional
Problems Type	Dynamic Nonlinear (High-Speed)	Static Linear/Nonlinear
	Complex Contact	Dynamic Linear
	Complex Post-Buckling	Dynamic Nonlinear (Low-Speed)
	Nonlinear Quasi-Static	
	Material with Degradation/Failure	
Solution Methodology	Integration Rule with A Diagonal or Lumped Element Mass Matrix	Newton Iterative Solution Method

Table 3-2: Comparison Between Commonly Utilized FE Software

Feature	ABAQUS™	Advantedge™	DEFROM
Modeling In-House	Yes	Yes	Yes
Modeling Complexity	Complex	Simple	Simple
Materials Library	Yes	Yes	Yes
Elements Types	All Types	Tetrahedron/Rectangle	Tetrahedron/Rectangle
Time Integration	Explicit and Implicit	Explicit	Implicit
Remeshing	No	Yes	Yes
Field	General	Cutting Processes	Deformation Processes
Code Modification	Yes	No	Yes
Parallelization	Yes	Yes	Yes

Chapter 4: Numerical Simulation and Experimental

Investigation

4-1 Preamble

An accurate representation of milling processes via 3D FEA software is a challenging task, because of several parameters involved. These parameters include kinematics of milling processes, modeling of the workpiece material, modeling of the cutting tool, and properly assembling the cutting tool to the workpiece within the FEA solver. In this chapter, a 3D FEA model for milling of hardened AISI 4340 steel (47 ± 1 HRC) is developed via ABAQUS/ExplicitTM solver. The model was built such that it exactly mimics the experimental setup. The results of the proposed model is validated by comparing its virtually simulated cutting forces and chip morphology to those obtained by the experiments of similar conditions.

4-2 Model Development

The simulated milling process presented in this model was based on a half immersion RDOC of a down milling operation. The assembly and initial mesh of the cutting insert and the workpiece is shown in Figure 4-1. Down milling kinematics was chosen, because this setup induces the highest impact forces at the start of each cut thus enables studying the effect of varying edge radii on the tool performance. During this setup, the tool initiates the cut with the largest and completes the cut with the smallest chip load. In end milling operations, RDOC is governed by the tool diameter, entry or start angle ϕ_{st} , and exit angle ϕ_{ex} . Kinematics of down milling is presented by Figure 4-2. All numerical simulations and experimental tests in this thesis were performed considering half immersion down milling operation. Which, is equivalent to a RDOC equal to a

quarter of the circumference of the experimental cutting tool, with entry and exit angles of 90° and 180° , respectively.

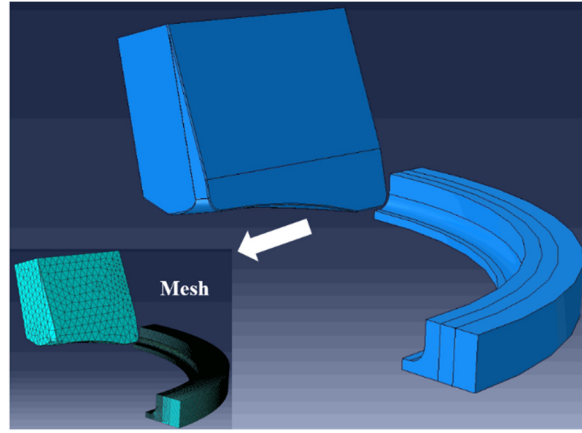


Figure 4-1: Cutting Insert and Workpiece Assembly In ABAQUS/ExplicitTM

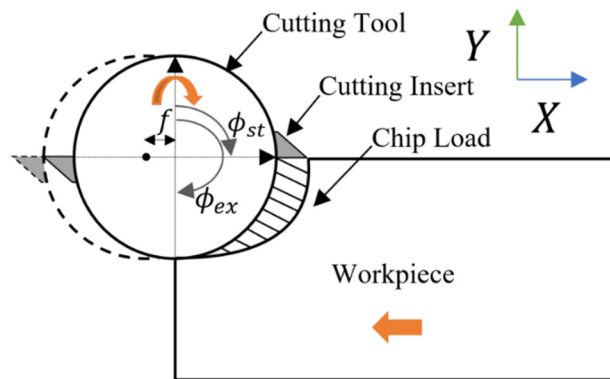


Figure 4-2: Down Milling Kinematics

4-2-1 Assigning Workpiece Material Properties

The workpiece was assigned the material properties of hardened AISI 4340 steel within the material module of the solver. The workpiece general properties are displayed in Table 4-1. The workpiece material was modeled as an elasto-plastic material and J-C materials strength model was adopted. As mentioned in chapter 3, J-C strength material model has the ability to represent the Von Mises flow stress and the thermo-viscous plastic behavior of the workpiece. Constants of J-C strength model are presented in Table 4-2 [21]. Also, the workpiece fracture was modeled by

adopting J-C fracture model and the constants of the J-C fracture model are displayed in Table 4-3 [21].

Table 4-1: Workpiece Material General Properties [54]

Parameter	Value
Young's Modulus (E)	205 GPa
Poisson's Ratio (ν)	0.3
Density	7850 kg/m ³
Specific Heat	475 J/KgK
Thermal Conductivity	44.5 W/mK
Thermal Expansion	13.7 μ m/mK

Table 4-2: Constants of J-C Strength Model [21]

Parameter	Value
A	950 MPa
B	725 MPa
C	0.015
n	0.375
m	0.625
$\dot{\epsilon}_0$	1 s ⁻¹
$T_{Reference}$	20 °C
$T_{Melting}$	1710 °C

Table 4-3: Constants of J-C Fracture Model [21]

Parameter	Value
D_1	- 0.8
D_2	2.1
D_3	- 0.5
D_4	0.002
D_5	0.61
$\dot{\epsilon}_0$	3,500 s^{-1}
$T_{Reference}$	20 °C
$T_{Melting}$	1710 °C

The workpiece consisted of 240889 nodes and 216948 elements. 216590 of the elements were type C3D8RT and 358 of the elements were type C3D6T. The C3D8RT elements are an 8-node thermally coupled brick, trilinear displacement and temperature, with reduced integration and hourglass control. Coupled temperature-displacement elements solve for temperature and displacement simultaneously. In addition, all three-dimensional coupled temperature-displacement elements have the following acronym C3DT. Between C3D and T, additional features of elements are added. For example, the 8 in C3D8RT refers to 8-nodes that each element has, and R is an element reduced integration feature. Meshing in FEA models impact the accuracy and overall computational time; thus, main cutting regions consisted of finer meshes in comparison to the rest of the workpiece. Figure 4-3 displays the meshed workpiece. The finest grade possible of meshing to the workpiece was selected based on the available resources.

Chapter 4: Numerical Simulation and Experimental Investigation

The option of “distortion control” was enabled, which allowed the solver to control excessive distortion problems and prevent elements from having negative volumes. Also, by enabling the “reduced integration” option, computational efficiency was improved. The FEA model required control for hourglassing effects; therefore, an “Enhanced” control was set. Hourglassing is a common numerical problem where elements become very flexible because their normal/shear stresses are equal to zero. Numerical results of elements experienced hourglass effects are considered inaccurate. Unlike continuous chips, the expected serrated chips are not fully connected and separation is required for their generation. Therefore, the “element deletion” option was enabled which allowed the solver to delete an element once the failure criteria is achieved and the element is fully damaged.

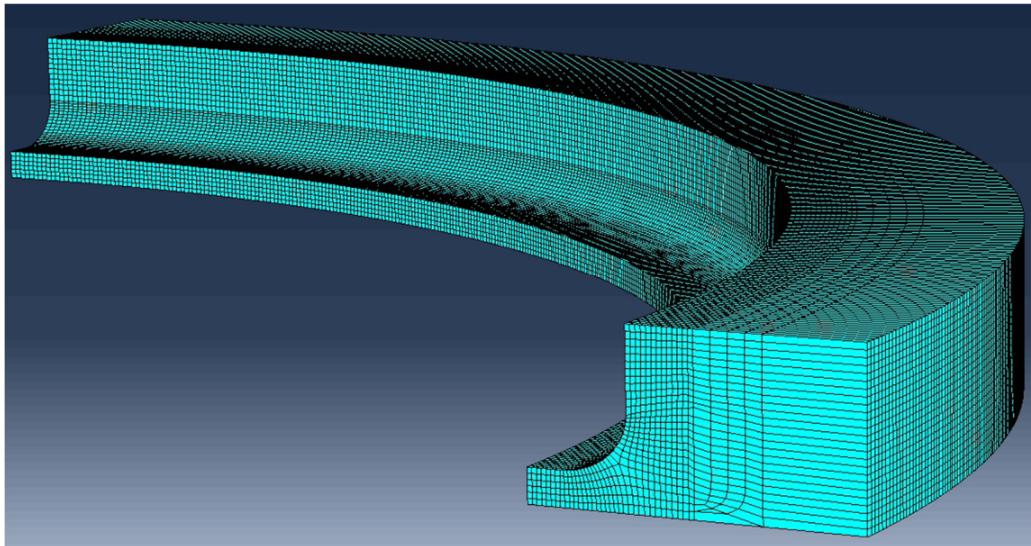


Figure 4-3: Meshed Workpiece in ABAQUS/Explicit™

4-2-2 Modeling of The Cutting Tool

The tool holder is a Sandvik CoroMill R390-020A20-11L cylindrical shank and it has a 20 mm diameter. Cutting inserts are tungsten carbide Sandvik R390-11T3-04M-PM-113 with PVD coating. Tool shank and cutting inserts are displayed in Figure 4-4.

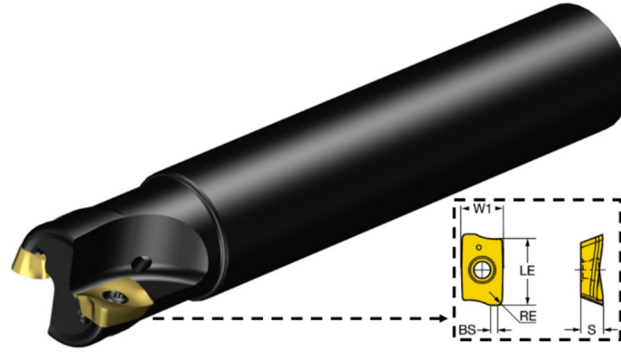


Figure 4-4: Tool Holder and Cutting Insert [55, 56]

The insert was modeled in ABAQUS/Explicit™ FEA solver, because when its STP file was imported into the software from the manufacturer website, meshing issues occurred and the model experienced numerical errors. The main available geometrical parameters of the cylindrical shank and the inserts are displayed in Table 4-4. However, inserts contain additional geometrical parameters that are not available on the manufacturer’s website and the provided catalogues. Therefore, microscopes and drawing techniques with CAD software were utilized to capture the remaining geometrical features.

Table 4-4: Dimensions of Cylindrical Shank and cutting Insert [55, 56]

Parameter	Value
Diameter	20 mm
Number of teeth/inserts (N_t)	2
Width ($W1$)	6.8 mm
Cutting Edge Effective Length (LE)	10 mm
Corner Radius (RE)	0.40 mm
Wiper Edge Length (BS)	0.90 mm
Thickness (S)	3.59 mm

Chapter 4: Numerical Simulation and Experimental Investigation

The provided geometrical features were used as a bench mark during modeling of the insert in ABAQUS/Explicit™. The steps to model the insert were executed in the following order after capturing all the necessary geometrical features from the microscopes and CAD software. (a) Drawing the insert as a block with approximately 60% of the length as displayed in Figure 4-5-a. The full length of the insert was not modeled, because only 10% of the length of cutting insert is in contact with the workpiece. This addition did not impact the structural support of the insert because the cutting insert was set as a rigid body. The thickness and the width were taken from the manufacture website as $S = 3.59 \text{ mm}$ and $W1 = 6.8 \text{ mm}$, respectively. (b) Adding the clearance angle of the insert as shown in Figure 4-5-b. This angle is a geometrical feature of the insert. The axial relief (clearance) angle is the angle that is with respect to the cylindrical shank. The clearance angle of the insert is equal to 21° . (c) Including the angle presented in Figure 4-5-c, which is equal to 7.5° and at a distance of 1.7 mm from the bottom of the indexable insert. (d) Drawing the angle shown in Figure 4-5-d, which is equal to 13.5° . This angle is created with respect with the line parallel to the thickness S of the insert. (e) Adding the angle displayed in Figure 4-5-e, which is equal to 1.3° . This angle is created with respect to the distance of 1.7 mm from the bottom of the indexable insert. (f) Including the corner radius (RE), the wiper edge length (BS) and the remaining geometrical parameters that make up the front section of the insert as shown in Figure 4-5-f. Values of RE and BS were provided by the manufacture. However, the remaining geometrical parameters that make up the front section of the insert were determined using the available measuring tools and microscopes at Ontario Tech's Machining Research Lab. (g) Drawing a 15° angle of the surface perpendicular to the rake face as presented in Figure 4-5-g. (h) Including the edge radius of the indexable insert as displayed in Figure 4-5-h, which is in equal to $35 \mu\text{m}$ for the commercially available inserts.

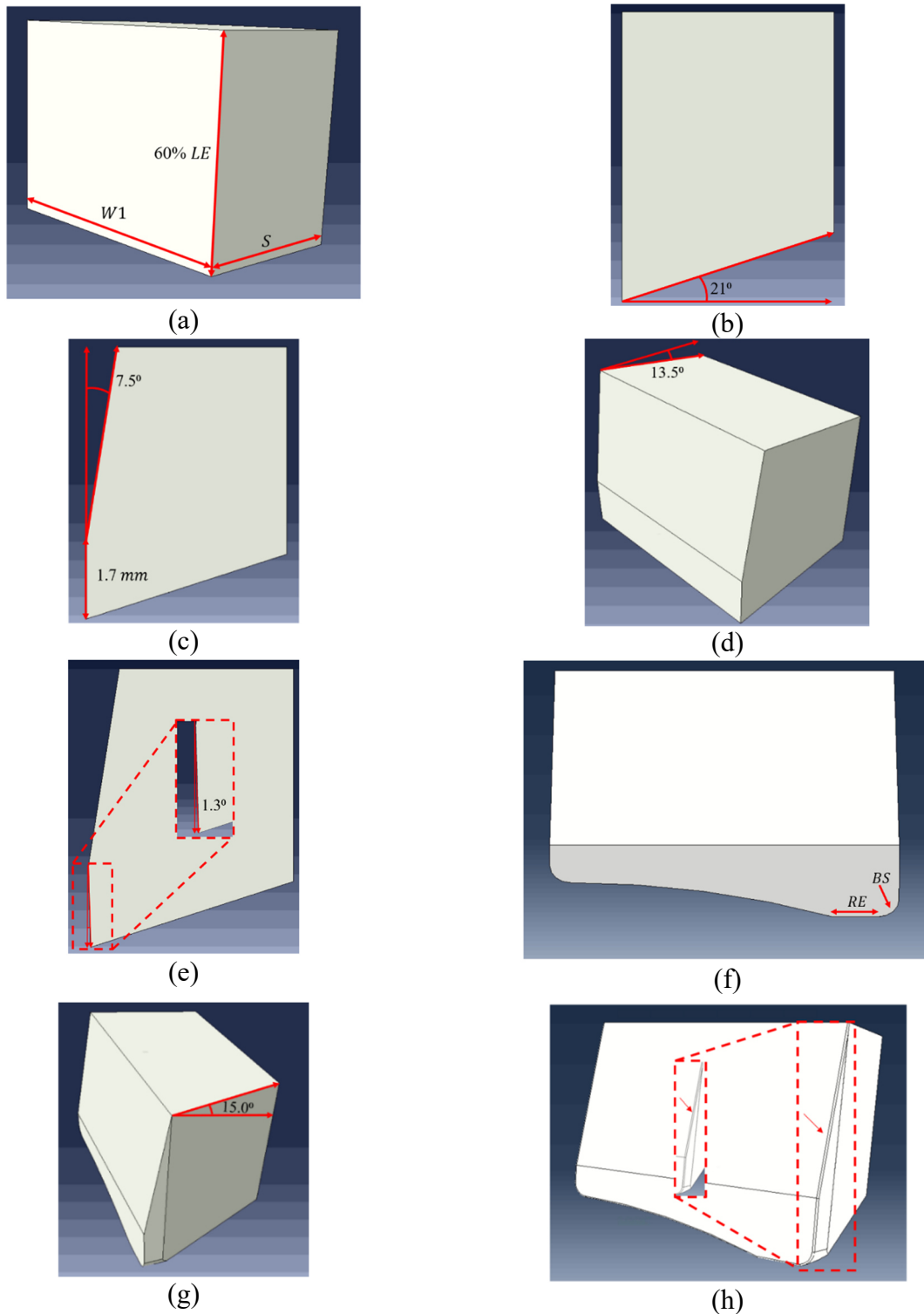


Figure 4-5: Steps Required to Draw the Cutting Insert in ABAQUS/Explicit™

In machining cutting tools are designed and selected to be significantly harder than the workpiece material. Therefore, the cutting tool was selected as a “Rigid Body” in this work. To

properly model the tool as a deformable body, a material model needed to be adopted for the tool. Such models require specific material constants of the tool that are not as widely available as those of the workpiece material. The Rigid insert consisted of 12649 nodes and 8222 C3D10M elements. Figure 4-6 displays the meshed insert.

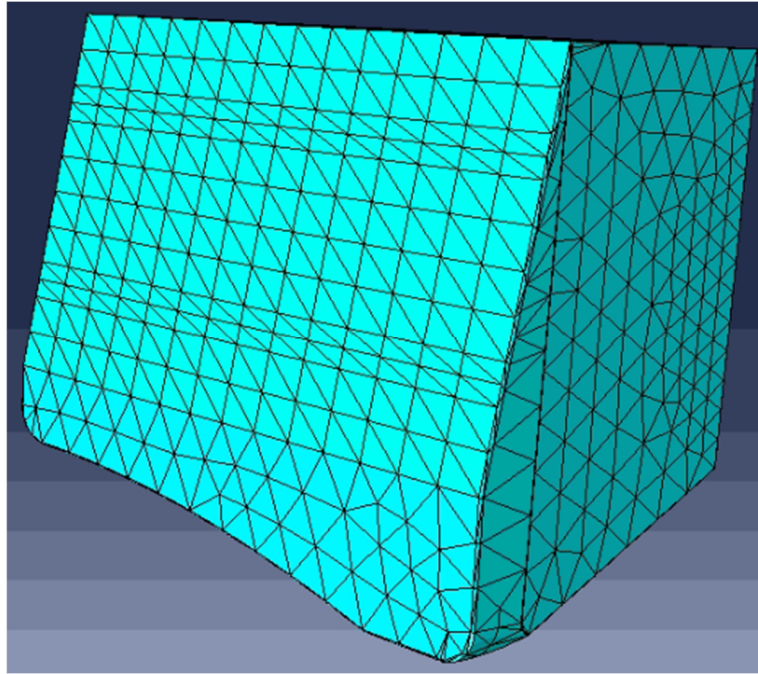


Figure 4-6: Meshed Insert in ABAQUS/Explicit™

4-2-3 Assembling Workpiece and Cutting Insert and Defining Boundary Conditions

The cutting tool and the workpiece were assembled in ABAQUS/Explicit™ to mimic the experimental down milling operation. During the assembly process of the insert with respect to the workpiece, the axial rake angle and the axial relief angles needed to be included. Therefore, a similar approach to capture the geometrical parameters of the insert was used, but those geometrical parameters were set with respect to the position of the insert to the cylindrical shank. The axial rake angle and the axial relief angle were 14.5° and 9° , respectively. During the experiments, the tool has two motions: a linear motion along the feed direction and rotational motion around its axis. In addition, in down milling kinematics, the tool initiates the cut at the

highest chip load and completes the cut at the lowest chip load. Therefore, to duplicate this phenomenon, the insert was assembled to consider the highest chip load for each case as shown in Figure 4-7.

The insert advances during each cut by moving a distance along the feed direction. This distance is known as feed per tooth and/or revolution f , and it is represented by equation (4.1). F is the feed rate, S_{speed} is the spindle speed and N_t is the number of teeth/inserts. Two inserts were used during milling experimental tests. The inserts were not positioned symmetrically with respect to the cylindrical shank. Therefore, one insert was able to remove more material than the other insert. The insert that removed more material was used as a roughing insert, while the insert that removed less material was a finishing insert. To reduce the computational cost (time), the presented FEA model in this work considers the roughing insert only. The spindle speed S_{speed} is obtained from equation (4.2), which is commonly used to calculate the cutting speed V . However, for the purpose of this model, the cutting speed equation was rearranged to calculate for the spindle speed. In equation (4.2) D_{tool} is the diameter of the cylindrical shank. Therefore, πD_{tool} is the circumference of the tool.

$$f = \frac{F}{S_{speed} * N} \quad (4.1)$$

$$N = \frac{V}{\pi D_{tool}} \quad (4.2)$$

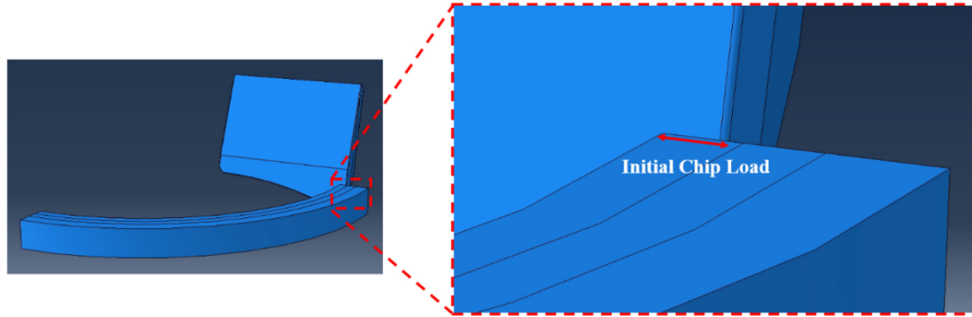


Figure 4-7: Initial Chip Load Formulation in ABAQUS/Explicit™

In order to include the chip thickness variation within the model, the insert was constrained by a “coupling” constraint to a “reference point”. Then, the insert rotated with respect to the axial direction of the reference point. The reference point was placed at a feed per tooth (insert) f distance from the origin as shown in Figure 4-8. This distance is the same distance the insert considers during its assembly to the workpiece, which enabled the model to consider the real chip load during the down milling operation. The same reference point was used to include the “Rigid Body” constraint of the insert. Moreover, regarding boundary conditions, the insert rotated with respect to the axial direction and the workpiece bottom surface was fixed in all six displacements/rotations.

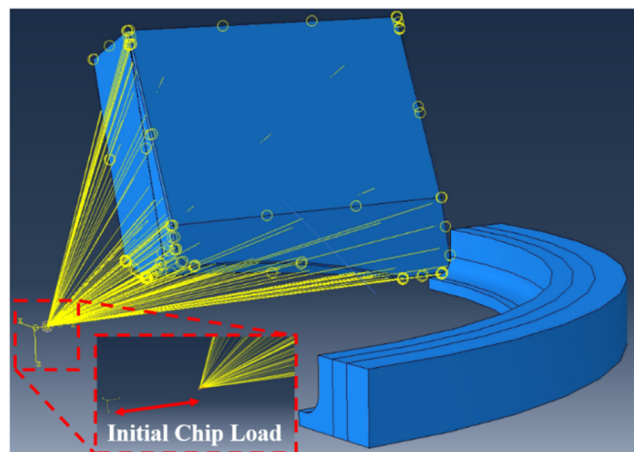


Figure 4-8: Reference Point Location in ABAQUS/Explicit™

4-3 Experimental Setup

Down milling tests were conducted to verify the proposed numerical model. Experiments were performed on a 3-axis HAAS VF-2BYT CNC machining center shown in Figure 4-9. The workpiece material is hardened AISI 4340 steel (47 ± 1 HRC).



Figure 4-9: 3-Axis HAAS VF-2BYT CNC Machining Center

Down milling experiments were conducted on square shaped blocks of workpieces with dimensions of $150 \times 150 \times 25$ mm. Blocks were clamped to the top of a 3-axis Kistler piezoelectric dynamometer Type 9255C, which was used to capture forces in three directions namely feed (x), stepover (y), and axial (z). Forces were captured in *Newtons*. However, the dynamometer cannot be connected directly into a Personal Computer. Therefore, multiple steps were conducted to present forces in *Newtons*. (a) Forces are captured by the Kistler piezoelectric dynamometer Type 9255C. (b) The dynamometer converts forces into a single electrical charge in pC and transforms the data into a distribution box type KDB5407A. (c) The distribution box splits the pC data into signals in three directions (x , y , z). (d) Data is transferred from the distribution box into three charge amplifiers type KCA5010B. Charge amplifiers converts data from pC to

Chapter 4: Numerical Simulation and Experimental Investigation

Volts. (e) Data is then transferred from KCA5010B to a National Instruments DAQ device. (f) The DAQ transfers the data into a personal computer. In the personal computer data is converted from *Volts* to *Newtons* analytically. Devices and tools that make up the experimental setup can be broken down into two sections inside and outside the CNC machine. The experimental setup inside and outside the machine is presented in Figure 4-10-a and b, respectively.

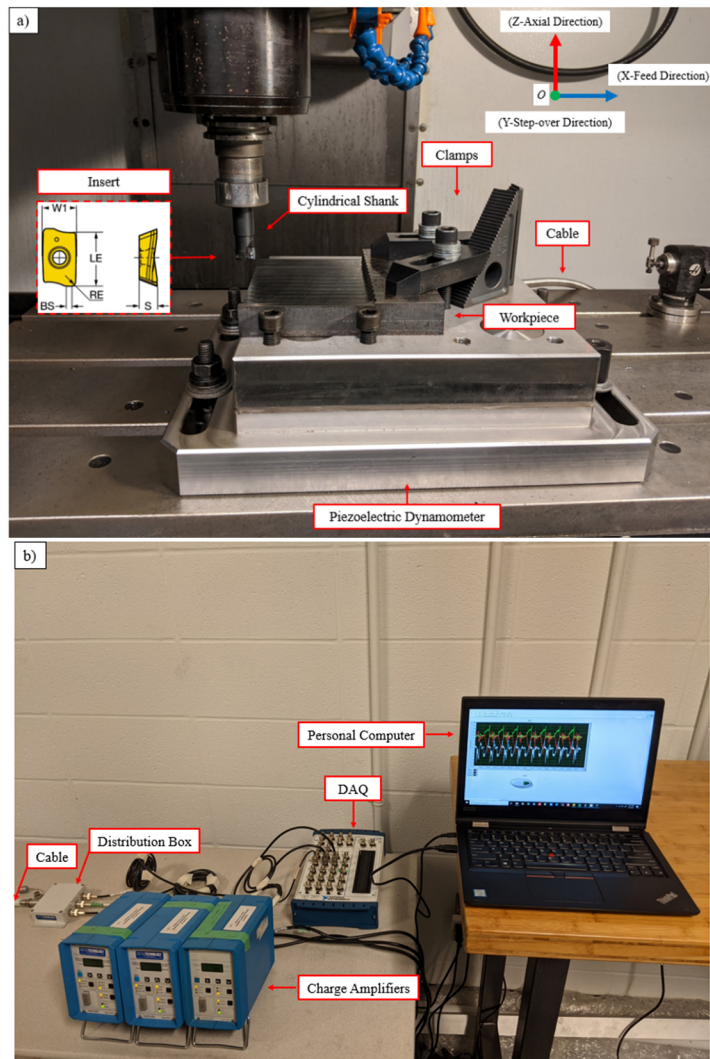


Figure 4-10: Experimental Setup

Six combinations of dry down milling tests were conducted at two levels of feed rate (800, 1000) mm/min and three levels of cutting speed (75, 100, 125) m/min . ADOC, RDOC and

Chapter 4: Numerical Simulation and Experimental Investigation

length cut were kept constant at 1 mm, half immersion and 100 mm, respectively during all experimental tests.

Moreover, experiments were conducted to analyze the impact of edge radii and cutting conditions on cutting forces, and surface integrity. Thus, experiments were conducted on five different edge radii variations. Edge radii were 25 μm , 30 μm , 35 μm , 40 μm , and 45 μm , as shown in Figure 4-11. Multiple inserts of each edge radius cut the workpiece material using the six combinations of cutting conditions. Therefore, a total of 30 experiments were conducted. This approach was employed because experiments conducted in this thesis were part of another research project, that investigated the influence of variable edge radius on the chipping of milling inserts and on the surface integrity of the workpiece material.

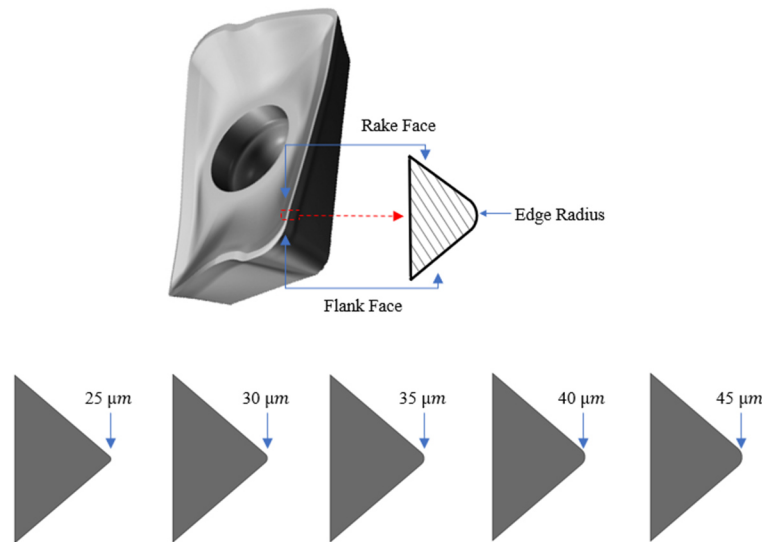


Figure 4-11: Edge Radii Comparison

In terms of experimental cutting forces, the impact of changing the edge radius was not noticeable due to the small variations in size. This phenomenon was also seen in the numerically generated cutting forces as shown in Figure 4-12. Figure 4-12 presents the cutting forces of the 25 μm , 30 μm , 35 μm , 40 μm , and 45 μm edge radii inserts when milling the workpiece at 1000

mm/min , $75 m/min$, $1 mm$, feed rate, cutting speed and ADOC, respectively. Therefore, the FEA model was validated using the $35 \mu m$ edge radius insert, because it is the commercially available cutting insert.

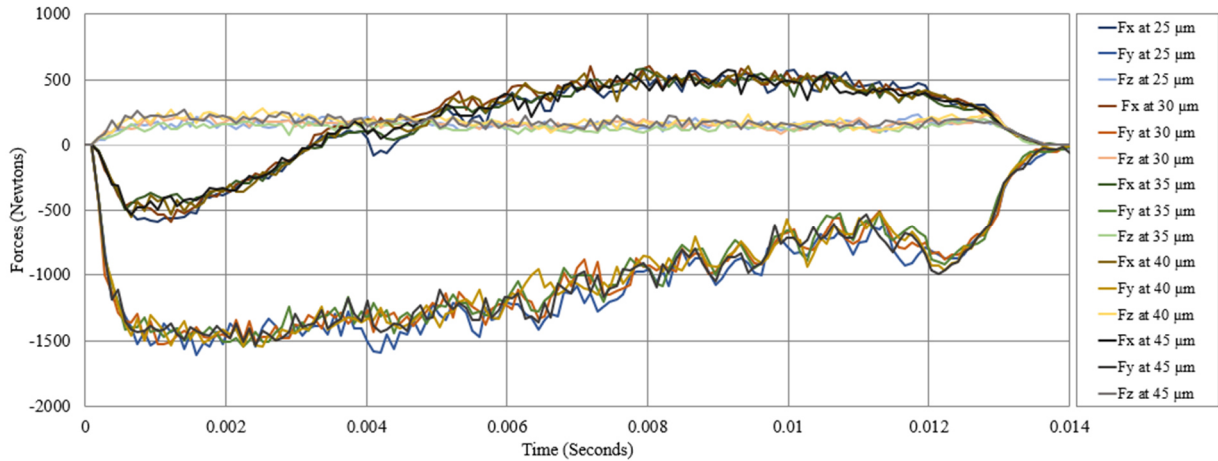


Figure 4-12: Numerical Forces Comparison Between Different Edge Radii

Cutting combinations were chosen to satisfy another research project that occurred concurrently to this research project. The other research project selected cutting conditions that promoted tools chipping and fracture during the milling process. Therefore, down milling was selected to induce higher impact at the beginning of each revolution. Additionally, the RDOC was selected as half immersion which generated the highest chip load at the beginning of each revolution. The intensity of the generated impact mainly depends on the cutting forces magnitude and the size of the cut area during each revolution. Hence, values of feed rates and cutting speeds had to be selected to prompt increasing the possibility of tools fracture within a reasonable machining time. The cutting tool manufacturer recommended a cutting speed of $280 m/min$ and a feed rate of $891 mm/min$. However, the recommended values are chosen for the purpose of multi-optimizing tool life and material removal volume. Therefore, multiple tests of various feed rates and cutting speeds were conducted to select values that allowed to instigate tool fracture within a reasonable machining

time. As a result, the selected values for cutting speeds were below the recommended manufacture’s values which increased the chip load. Increasing the chip load increases the magnitude of cutting forces, causing cutting tools to fracture faster. In addition, values of feed rates were chosen within the recommended manufacture limits because a sudden tool breakage after a short distance of cut was observed when feed rates were chosen slightly above the recommended limits. Therefore, it was found that cutting speeds below the recommended limits and feed rates within the recommended limits, displayed the most consistent method to promote fracture in the inserts. ADOC was selected as 1 *mm* to consider the full impact of nose radius of the cutting inserts, which was 0.4 *mm*. Larger ADOC would have promoted chatter and resulted in process instability. A new set of inserts was used for each cutting combination. Cutting conditions are displayed in Table 4-5.

Table 4-5: Experimental Cutting Conditions

Test	Feed Rate <i>mm/min</i>	Cutting Speed <i>m/min</i>	Length of Cut <i>mm</i>
1	800	75	100
2	800	100	100
3	800	125	100
4	1000	75	100
5	1000	100	100
6	1000	125	100

4-4 Model Verification

4-4-1 Experimental and Numerical Cutting Forces Verification

The proposed numerical model was validated in terms of cutting forces generation and chip formation. Cutting forces are important to validate, because they can be used to evaluate the required power, torque of the machine tool, and various parameters for the machining system [57].

Therefore, the validation of cutting forces was conducted by comparing two parameters: the average resultant forces \bar{F}_r and individual cutting forces components in the x , y and z directions. The resultant force is calculated in terms F_x , F_y , and F_z forces as shown in equation (4.3). Figure 4-13 displays a comparison between the experimental and numerical average resultant cutting forces \bar{F}_r of all six cutting conditions. The numerical model presented an average resultant forces error of 11.3%, between all six cases.

$$F_r = \sqrt{F_x^2 + F_y^2 + F_z^2} \quad (4.3)$$

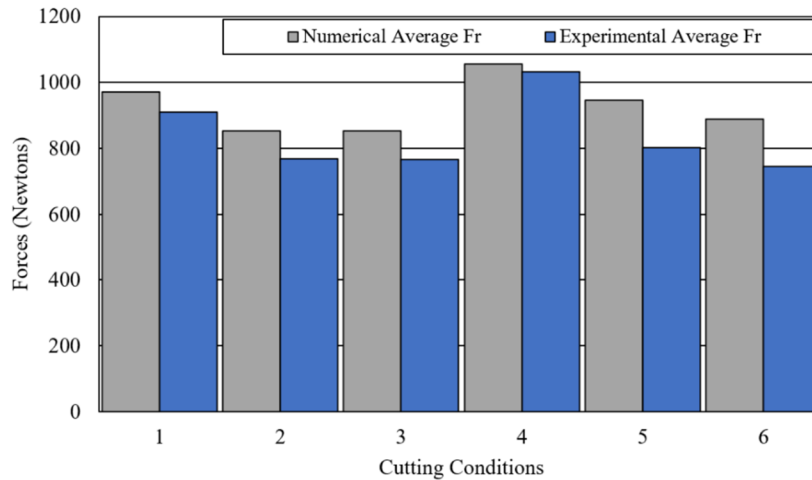


Figure 4-13: Experimental vs. Numerical Average Resultant Cutting Forces \bar{F}_r

- | | |
|--|---|
| 1 $V = 75 \text{ m/min}$ and $F = 800 \text{ mm/min}$ | 4 $V = 75 \text{ m/min}$ and $F = 1000 \text{ mm/min}$ |
| 2 $V = 100 \text{ m/min}$ and $F = 800 \text{ mm/min}$ | 5 $V = 100 \text{ m/min}$ and $F = 1000 \text{ mm/min}$ |
| 3 $V = 125 \text{ m/min}$ and $F = 800 \text{ mm/min}$ | 6 $V = 125 \text{ m/min}$ and $F = 1000 \text{ mm/min}$ |

Presenting the \bar{F}_r alone does not provide a clear explanation for the validity process of the model, because it does not provide a clear representation on the contribution of each force component to the \bar{F}_r . Therefore, bar charts of the absolute average numerical and experimental cutting forces $|\bar{F}_x|$, $|\bar{F}_y|$, $|\bar{F}_z|$ and $|\bar{F}_r|$ were constructed to compare each experimental and numerical cutting force component. Figure 4-14 to Figure 4-19 display the bar charts for six cutting condition.

Chapter 4: Numerical Simulation and Experimental Investigation

The charts display that the absolute average step-over cutting force $|\bar{F}_y|$ is the largest component of cutting force, because mainly along the y -direction a chip begins to form. The second place is occupied by the absolute average feed cutting force $|\bar{F}_x|$, this force component accounts for the advancement of the tool along the feed direction. Moreover, during the tool rotation a chip continuously forms along the y -direction and the x -direction. However, unlike the x and y directions the z -direction component $|\bar{F}_z|$, does not have a direct contact with the workpiece. Therefore, it is the lowest force component. $|\bar{F}_y|$, displayed a close agreement with its experimental counterparts. A slight discrepancy was noticeable when comparing the experimental and numerical $|\bar{F}_x|$. $|\bar{F}_z|$ displayed the largest discrepancy however it had the lowest magnitude. Therefore, its discrepancy had the lowest impact on the overall error. This variation directly influenced the percentage error between the numerical and experimental resultant cutting forces \bar{F}_r . The average percentage error between the numerical and experimental $|\bar{F}_x|$, $|\bar{F}_y|$, $|\bar{F}_z|$ and $|\bar{F}_r|$ for all six cutting conditions was 7.9%, 13.95 %, 26.4 %, and 11.3%, respectively.

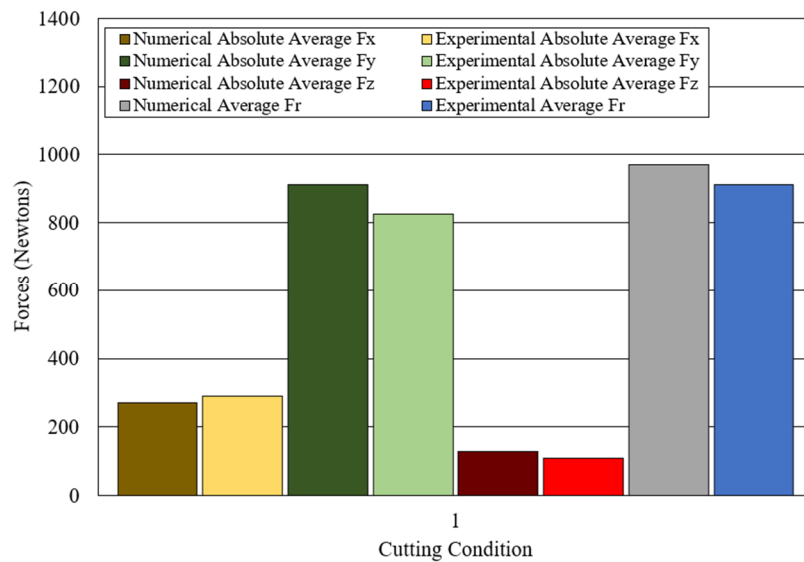


Figure 4-14: Feed Rate = 800 mm/min and Cutting Speed = 75 m/min

Chapter 4: Numerical Simulation and Experimental Investigation

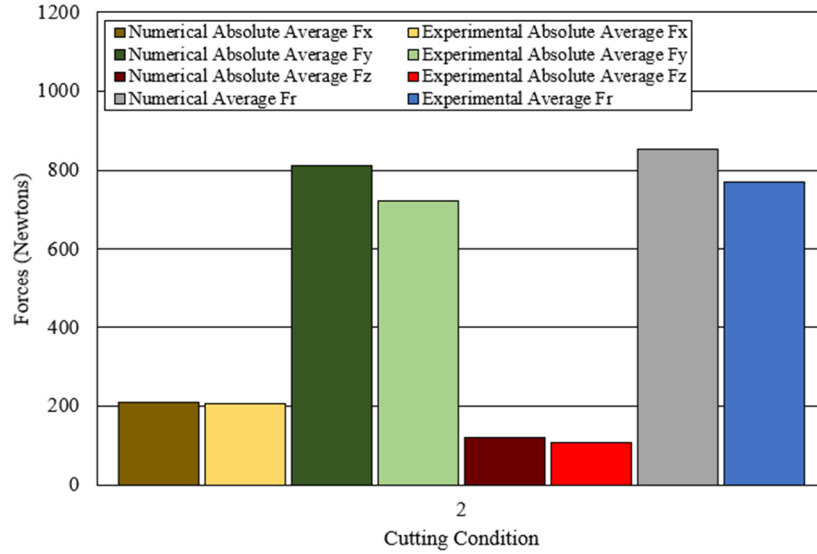


Figure 4-15: Feed Rate = 800 mm/min and Cutting Speed = 100 m/min

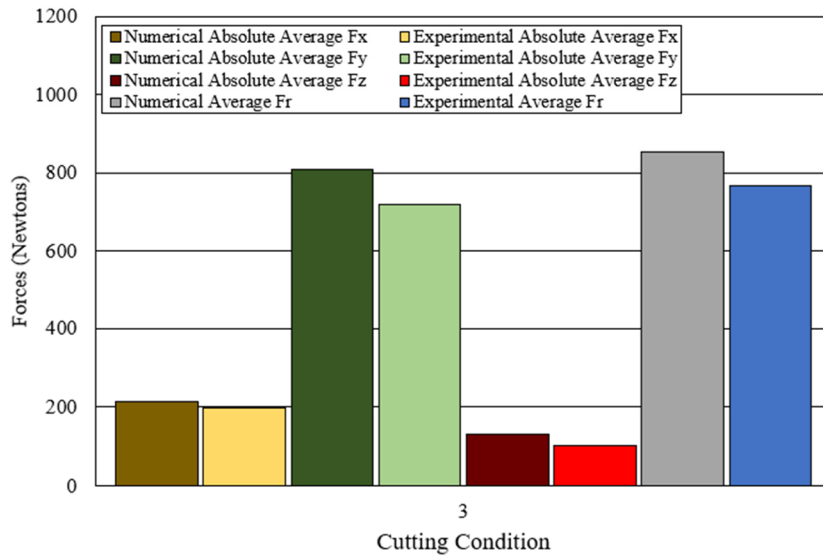


Figure 4-16: Feed Rate = 800 mm/min and Cutting Speed = 125 m/min

Chapter 4: Numerical Simulation and Experimental Investigation

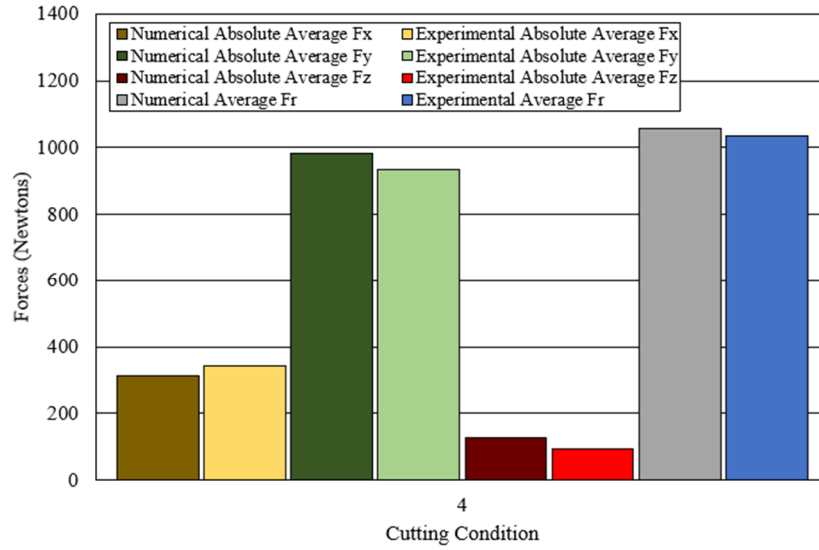


Figure 4-17: Feed Rate = 1000 mm/min and Cutting Speed = 75 m/min

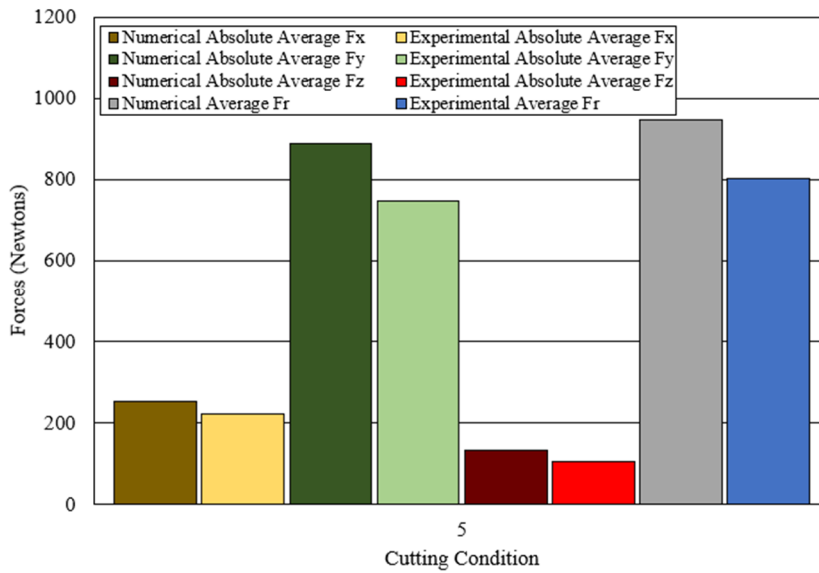


Figure 4-18: Feed Rate = 1000 mm/min and Cutting Speed = 100 m/min

Chapter 4: Numerical Simulation and Experimental Investigation

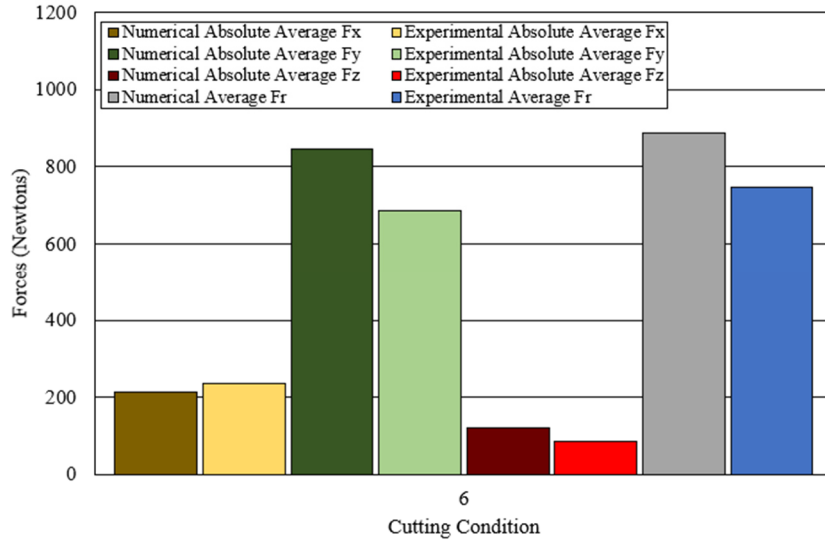


Figure 4-19: Feed Rate = 1000 mm/min and Cutting Speed = 125 m/min

In order to add another layer of validation into the comparison of experimental and numerical cutting forces, multiple plots of cutting forces against time were constructed. Each individual experimental and numerical force for all six combination displayed a clear agreement, which in turn ensure the validity of the model as shown in Figure 4-20 to Figure 4-25. The numerical and experimental cutting forces were compared against each other to validate the model. An agreement in the trends of cutting forces presents the model's ability to describe the process's kinematics and boundary conditions.

Fluctuations in numerical values are due to the element deletion criterion used. The element deletion criterion enhanced the model's ability to mimic the experimental setup, by allowing numerical chips to have variable thicknesses. The experimental setup included the advancement of the cutting tool to the workpiece and the simultaneous rotation of the cutting tool to generates variable chip thickness. Hence, during the generation of a variable chip thickness, elements experience different magnitudes of force from the rotating/advancing cutting tool. Therefore,

numerical elements experience different levels of deformation, which causes the fluctuations within the numerically generated forces over time.

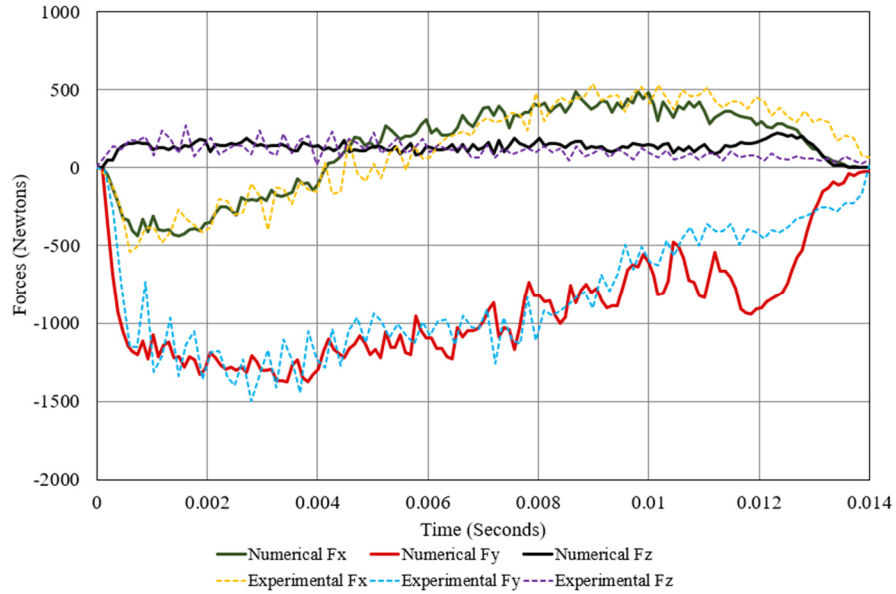


Figure 4-20: Feed Rate = 800 *mm/min* and Cutting Speed = 75 *m/min*

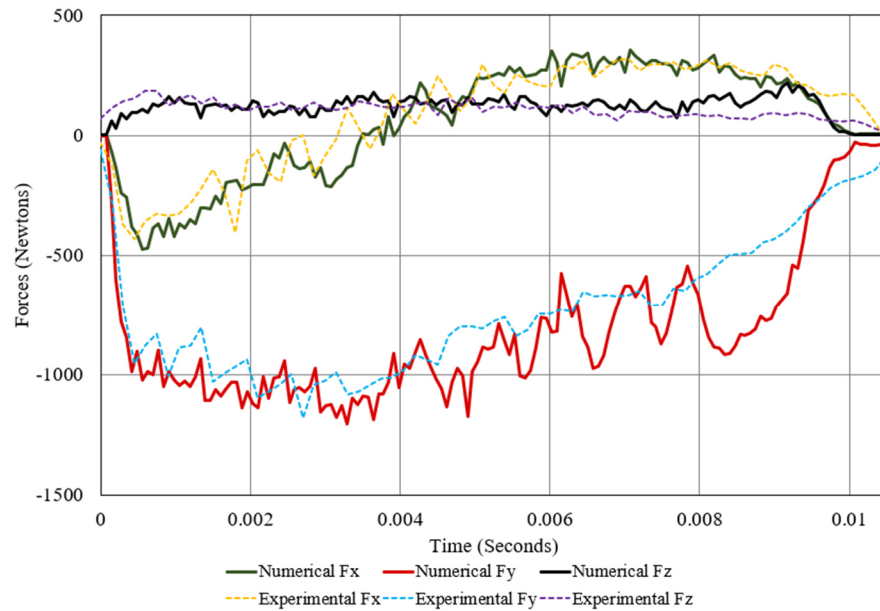


Figure 4-21: Feed Rate = 800 *mm/min* and Cutting Speed = 100 *m/min*

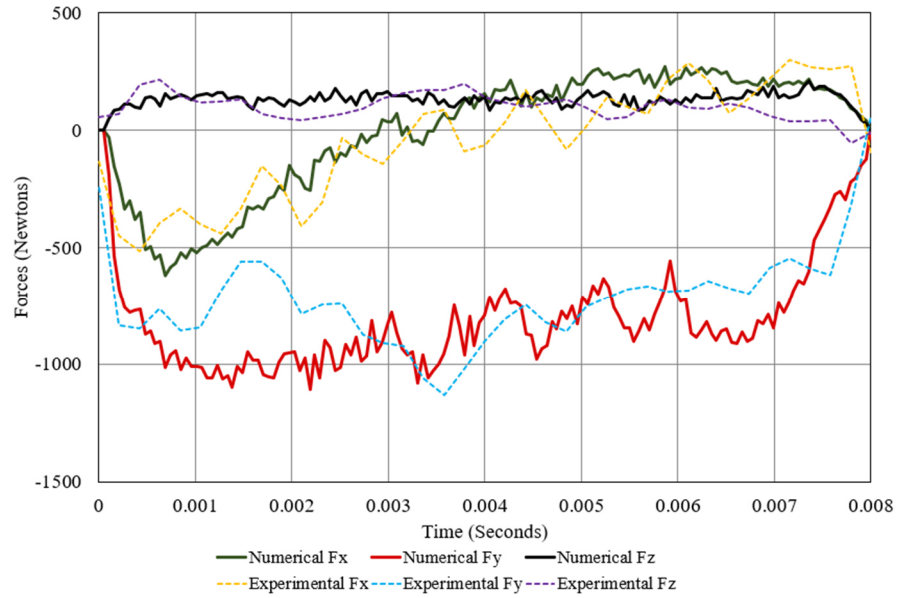


Figure 4-22: Feed Rate = 800 *mm/min* and Cutting Speed = 125 *m/min*

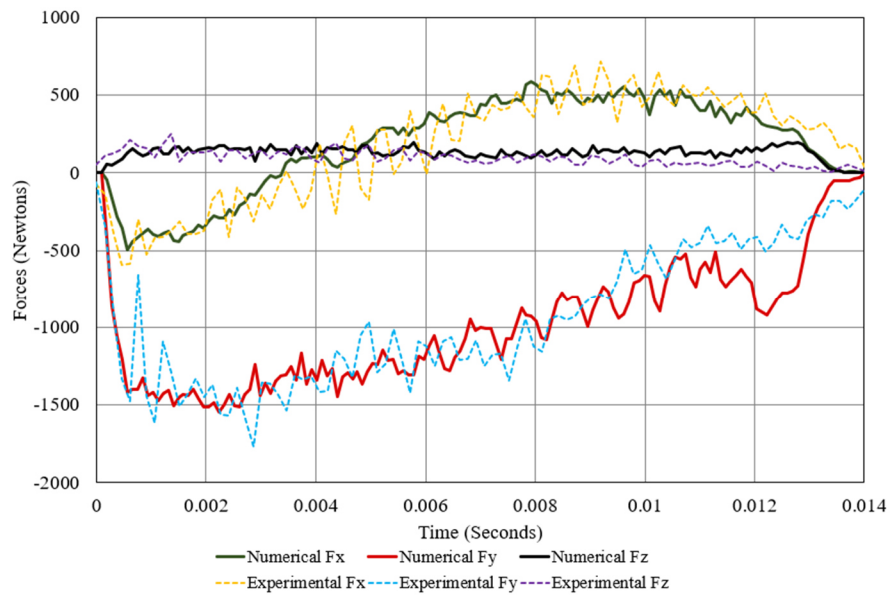


Figure 4-23: Feed Rate = 1000 *mm/min* and Cutting Speed = 75 *m/min*

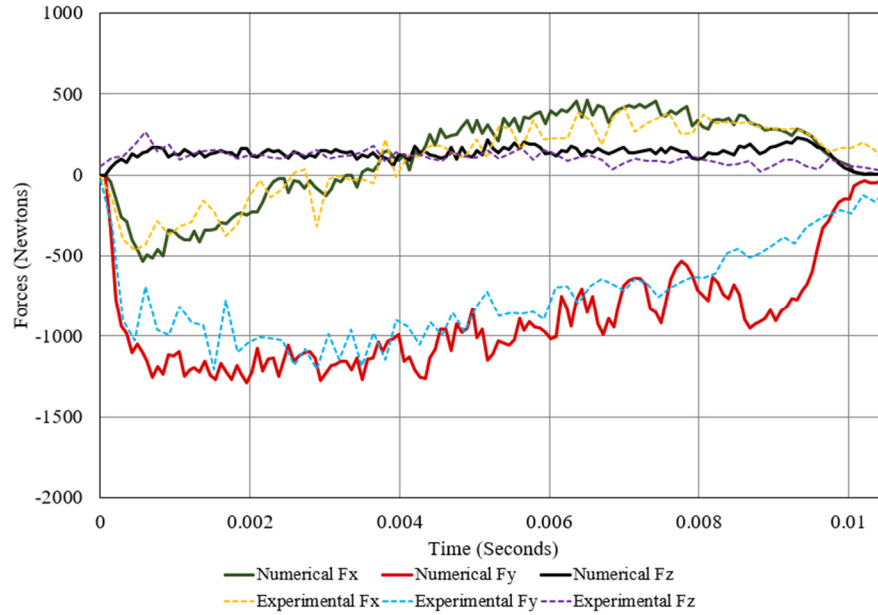


Figure 4-24: Feed Rate = 1000 mm/min and Cutting Speed = 100 m/min

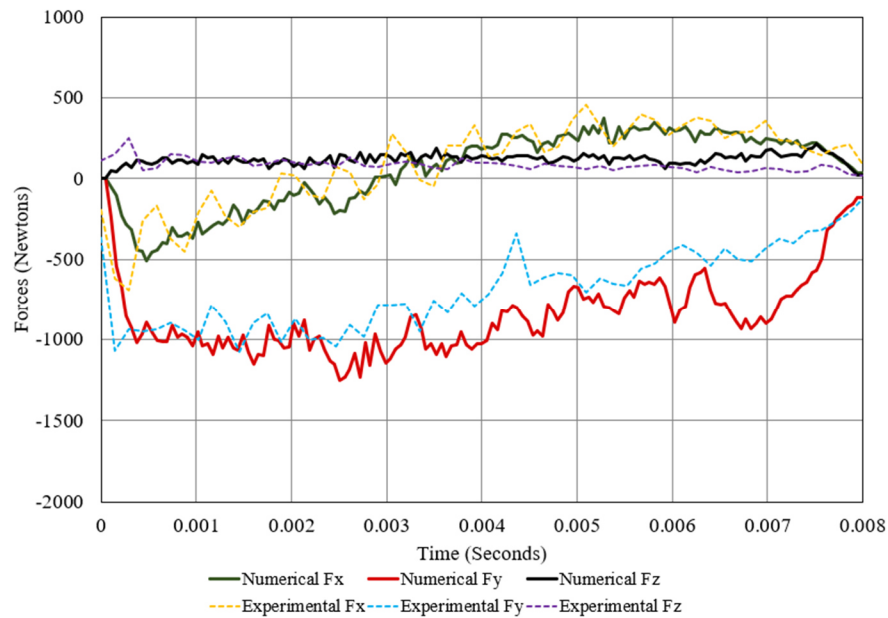


Figure 4-25: Feed Rate = 1000 mm/min and Cutting Speed = 125 m/min

Moreover, in all six cutting conditions, the numerical F_y and F_z deviates from the experimental F_y and F_z at around 85-90% of the engagement between the insert and the workpiece. The

percentage error of the numerical model is mainly influenced by the deviation at the last portion of the cut along the step-over and axial directions.

Hence, the numerical error was thoroughly investigated as shown in Figure 4-26 (a-d) of $F = 1000 \text{ mm/min}$ and $V = 75 \text{ m/min}$. Figure 4-26 (a), displays and relates the average cutting forces, to cutting forces variation through time. The area which contains the largest numerical to experimental F_y and F_z cutting forces deviation is highlighted and it beings at around 11 ms . Figure 4-26. (b, c, and d) highlights the simulation at 11.6 ms , 12.13 ms , and 12.6 ms , respectively. Mentioned simulation times were selected to display the advancement of the insert at the last portion of the cut over time. Despite the attempt of the insert to generate a chip throughout the cut, the insert generates a serrated chip that becomes fully disconnected from the workpiece at around 75% of cutting distance.

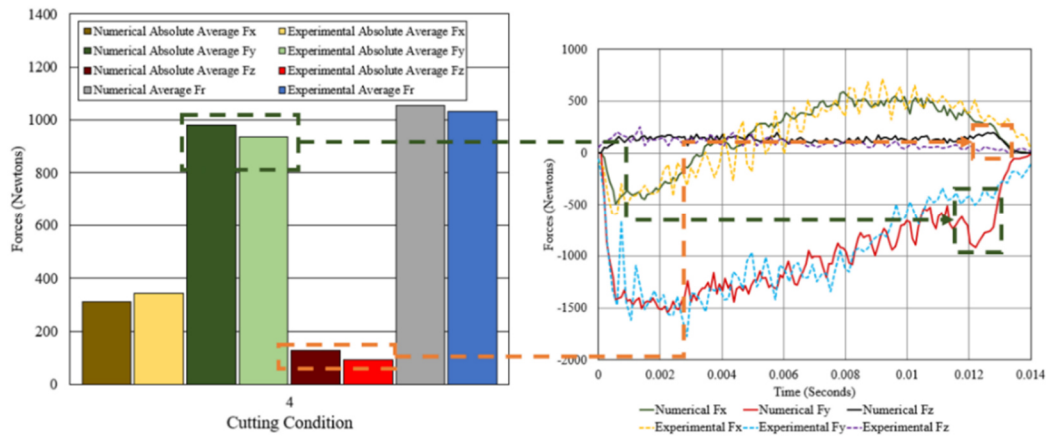
This phenomenon beings to occur at 11 ms (80% of the cut) and onwards, where the cutting insert attempts to remove material from the workpiece after the disconnection of the generated serrated chip from the workpiece. But, the cutting insert cannot seize enough workpiece material to generate a proper chip and only small discontinuous tiny pieces of a chip are formed.

Thus, the insert begins to bend the workpiece elements mainly along the step-over and axial directions. When the cutting tool bends the workpiece elements, the numerically calculated energy of the elements also increases. Any increase in the energy of elements increases their internal stresses and consequently increases the forces along the step-over and axial direction within the simulation.

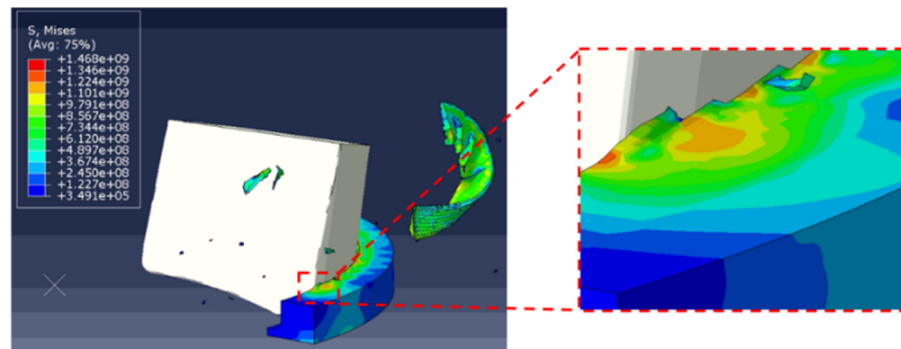
During experimental down milling tests, this phenomenon does not occur, because cutting tools are able to generate a variable chip thickness from the start to the end of each rotation. The

Chapter 4: Numerical Simulation and Experimental Investigation

continuous revolution of cutting tools and its advancement along the feed direction enables the chips generation at every rotation. This is not the case in numerical simulation in which only one revolution of a single insert is modelled and elements are either deleted if their failure criteria is reached when the tool sizes enough material from the workpiece, or bent towards the workpiece if the tool fails to sizes enough material to form a chip, resulting in increasing the internal stresses of the bent in elements. The numerical model simulates a single half immersion down milling cut. If the model was set-up to simulate multiple rotation of a cutting tool it would address the issue of the tool being unable to size enough material. However, that would increase the computational time significantly.

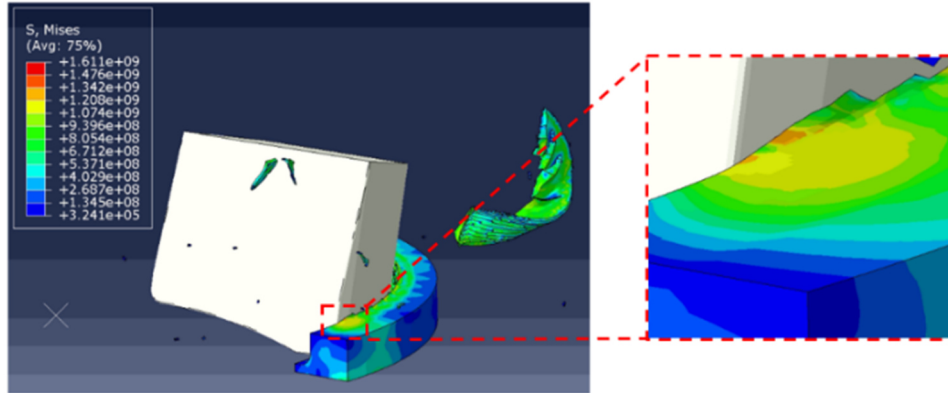


(a) Forces Deviation

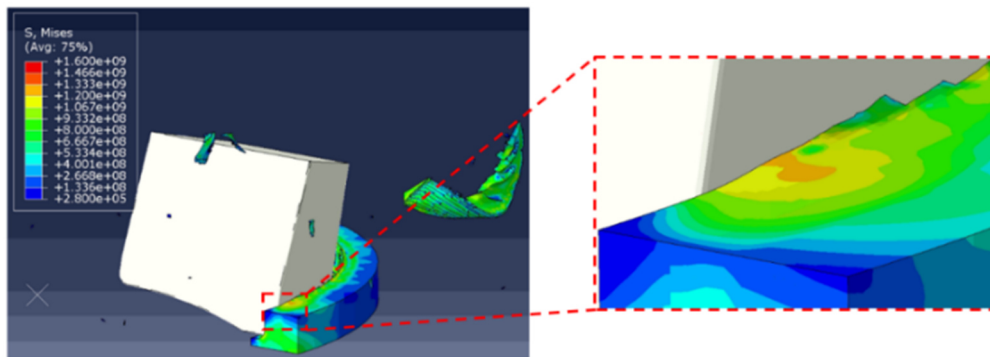


(b)

Figure continues in the next page



(c)



(d)

Figure 4-26: Numerical Model Error Discussion

4-4-2 Experimental and Numerical Chip Formation Validation

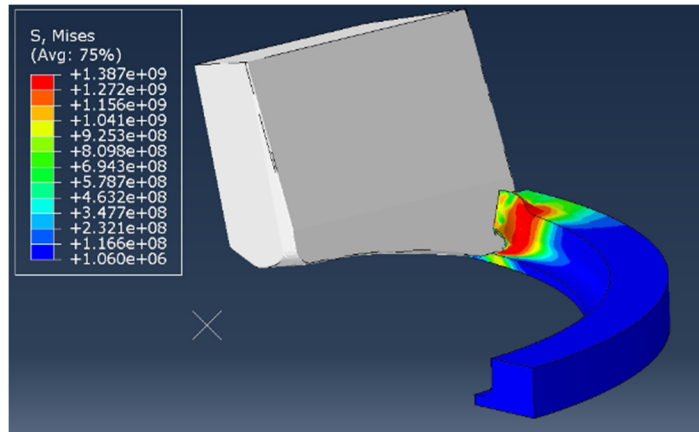
During all experimental tests serrated (saw-toothed) chips were produced. This type of a chip is commonly generated during milling hardened steels [22]. Existence of serrated chips is explained by two theories namely thermos plastic shear instabilities also known as adiabatic shearing and/or cyclic cracking [58]. Adiabatic shearing occurs when the heat generated during the cutting operation does not have enough time to dissipate and remains within the cutting region, which increases the effects of thermal softening and strain hardening. An increase of thermal effects results in a localization of material strain within narrow layers of the primary shear zone.

Chapter 4: Numerical Simulation and Experimental Investigation

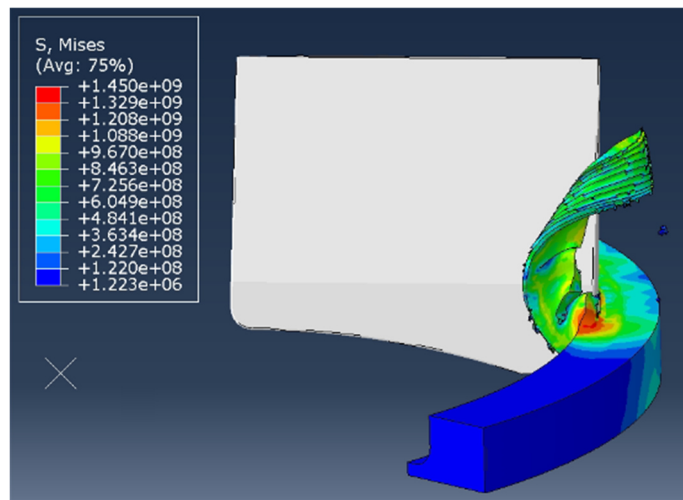
On the other hand, cyclic cracking is fatigue failure of generated chips. Chips continuously experience an increase of structural damage; therefore, cracking occurs when high shearing is localized within the primary shear zone. Also, cracks initiate and propagate within the primary shear zone. A comparison between the collected chip during experiments and the numerically generated chip is displayed in Figure 4-27 and Figure 4-28, respectively when cutting speed is 75 m/min and feed rate is 1000 mm/min . Serrated (saw-toothed) chip is obtained from the experiments. Similarly, a serrated chip is generated by the proposed 3D FEA model. The close agreement between the numerical and experimental chips adds an additional layer of validation to the model.



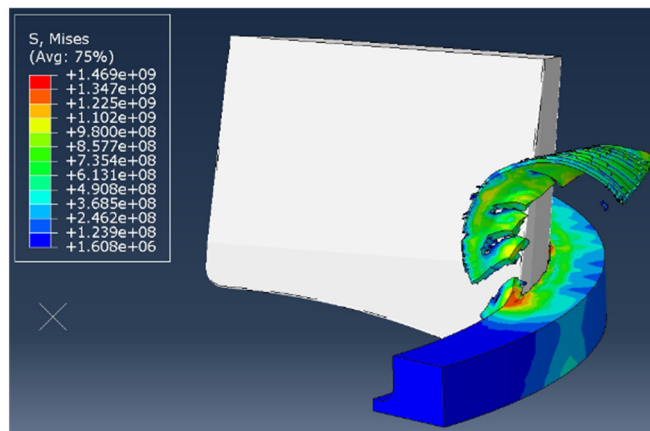
Figure 4-27: Experimentally obtained Serrated Chip



(a) Beginning of the Cut



(b) Middle of the Cut



(c) Ending the cut

Figure 4-28: Generation of a Serrated chip in ABAQUS/Explicit™

4-5 Impact of Cutting Conditions on the Experimental and Numerical Cutting Forces

The impact of feed rate on the resultant force F_r can be investigated when the feed rate is adjustable, while all other geometrical and cutting parameters remain unchanged. This investigation is conducted as presented below in Table 4-6 and Figure 4-29 to Figure 4-34. These figures compare the numerical and experimental resultant force for different cutting speeds and feeds that are outlined in Table 4-6.

Table 4-6: Comparison Between Feed Rates and Cutting Speeds

Cases Type	Feed Rate mm/min	Cutting Speed m/min	Chip Load mm	Average Resultant Force \bar{F}_r N
Numerical	800	75	0.34	972
Experimental	800	75	0.34	911
Numerical	1000	75	0.42	1056
Experimental	1000	75	0.42	1033
Numerical	800	100	0.25	854
Experimental	800	100	0.25	769
Numerical	1000	100	0.31	946
Experimental	1000	100	0.31	802
Numerical	800	125	0.20	854
Experimental	800	125	0.20	767
Numerical	1000	125	0.25	889
Experimental	1000	125	0.25	747

Chapter 4: Numerical Simulation and Experimental Investigation

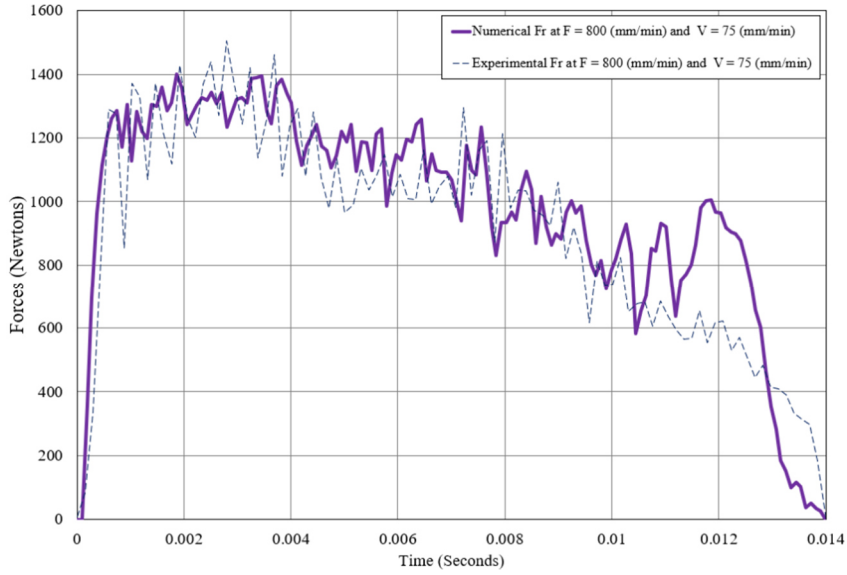


Figure 4-29: Forces at Feed Rate = 800 mm/min and Cutting Speed = 75 m/min

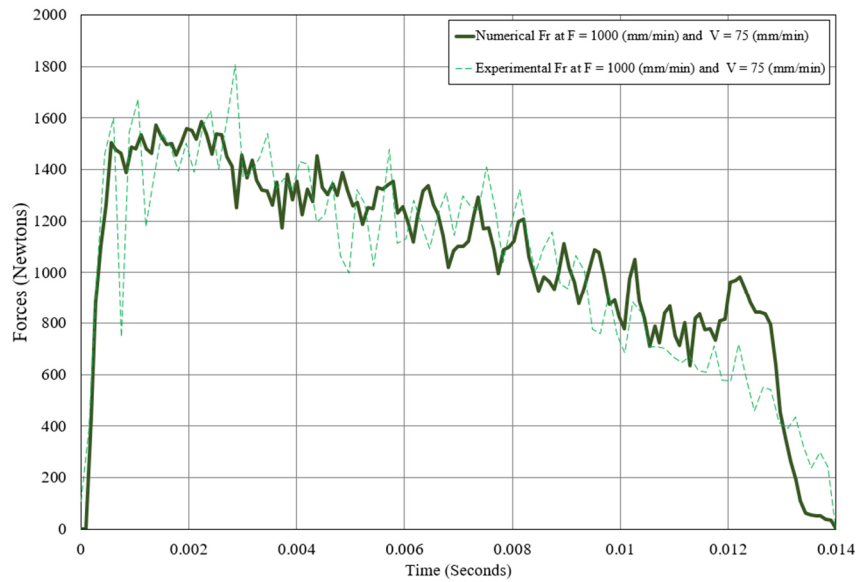


Figure 4-30: Forces at Feed Rate = 1000 mm/min and Cutting Speed = 75 m/min

Chapter 4: Numerical Simulation and Experimental Investigation

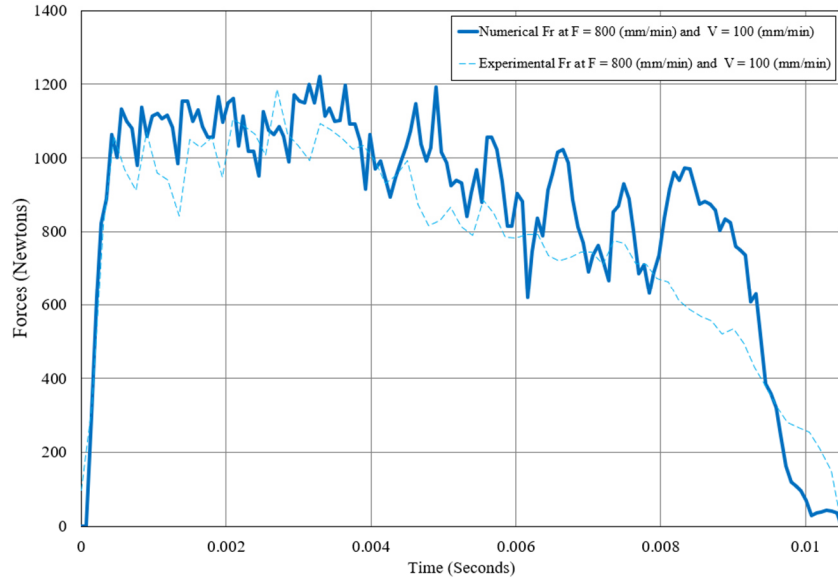


Figure 4-31: Forces at Feed Rate = 800 mm/min and Cutting Speed = 100 m/min

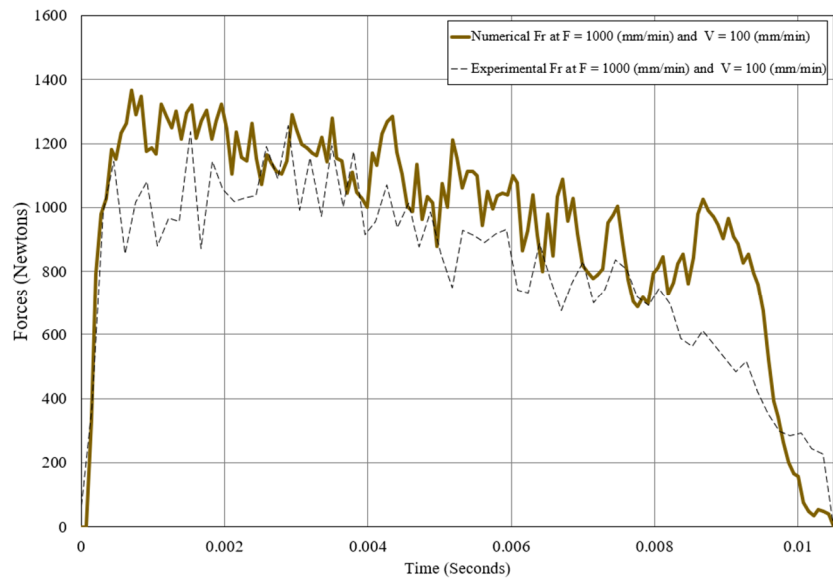


Figure 4-32: Forces at Feed Rate = 1000 mm/min and Cutting Speed = 100 m/min

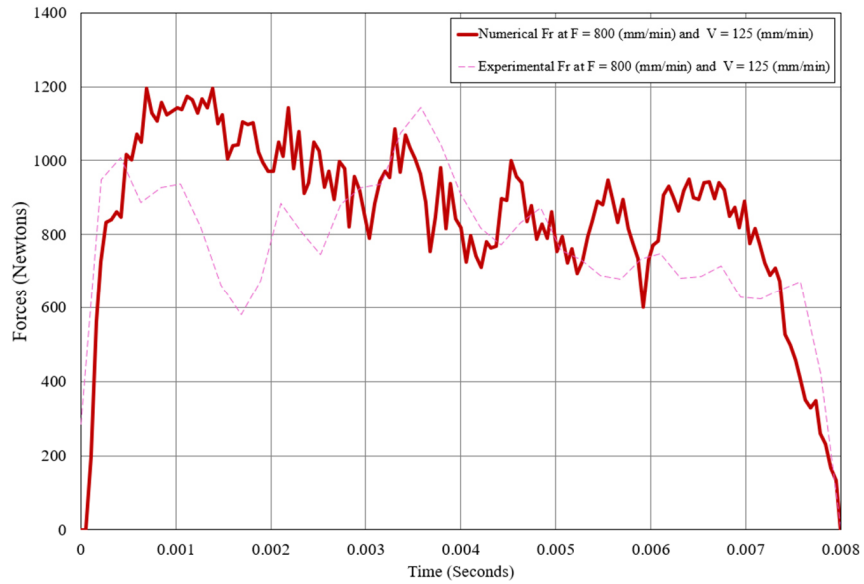


Figure 4-33: Forces at Feed Rate = 800 mm/min and Cutting Speed = 125 m/min

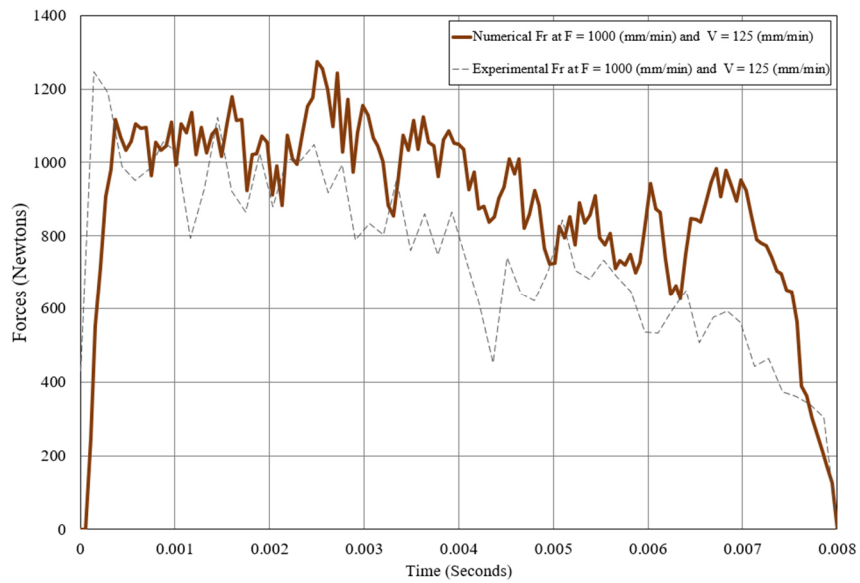


Figure 4-34: Forces at Feed Rate = 1000 mm/min and Cutting Speed = 125 m/min

Experimental and numerical comparisons clearly indicate that an increase in feed rates increases cutting forces, similar phenomenon was reported by [59]. Because, increasing feed rates increases directly the uncut chip thickness (chip load). An increase of uncut chip thickness causes the tool to remove more material, which generates higher forces. Experimental/numerical forces increase significantly when feed rates increase from 800 mm/min to 1000 mm/min , while maintaining

constant cutting speeds. The highest experimental and numerical \bar{F}_r occurred at a feed rate of 1000 mm/min and a cutting speed of 75 m/min and the forces were equal to 1033 N and 1056 N , respectively. Also, chip load was the highest at that cutting condition at 0.42 mm . The lowest experimental and numerical \bar{F}_r occurred at a feed rate of 800 mm/min and a cutting speed of 125 m/min forces were equal to 767 N and 854 N , respectively. Chip load was the lowest at that cutting condition at 0.20 mm . In addition, the maximum resultant cutting force $F_{r_{max}}$ is highest when feed rates increased from 800 mm/min to 1000 mm/min at all cutting conditions as shown in Figure 4-29 to Figure 4-34.

Similarly, the impact of cutting speed on the resultant force F_r can be investigated when the cutting speed is variable, while geometrical and cutting parameters remain constant. This investigation can also be illustrated in Table 4-6 and figures Figure 4-29 to Figure 4-34. A faster tool rotation results in a quicker completion of a milling cut. Similarly, a slower tool rotation results in a slower completion of a cut. An increase of tool rotation decreases the chip load per tooth throughout the cut. Subsequently, decreasing the generated cutting forces. According to Table 4-6 experimental/numerical forces increase when cutting speeds decrease from 125 m/min to 75 m/min , while maintaining constant feed rates. The highest experimental and numerical \bar{F}_r occurred at the lowest cutting speed of 75 m/min and at a feed rate of 1000 mm/min and the corresponding experimental and numerical forces were 1033 N and 1056 N , respectively. Also, chip load was the highest at that cutting condition at 0.42 mm . The lowest experimental and numerical \bar{F}_r and chip load of 0.20 mm occurred at the highest cutting speed of 125 m/min and a feed rate of 800 mm/min , forces were 767 N and 854 N , respectively. The impact of feed rates and cutting speeds was similar for all different scenarios of edge radii. In which forces increase with the increase of feed rates and decrease of cutting speeds and vice versa. This is reasoned to

the small variation in sizes of edge radii the smallest being around 25 μm and the largest being around 45 μm .

4-6 Summary

In chapter 4, a 3D FEA model that duplicated a down milling process was thoroughly setup and validated. A down milling kinematics was selected because cutting tools experience higher initial impact during down milling in comparison to up milling. High Impacts results in tool fracture and in some cases catastrophic tool failure. FEA models allow researchers to investigate the impact of cutting/ tool geometrical conditions intensely and present features that are impossible/ or difficult to capture analytically and experimentally.

The 3D model of the commercially available 35 μm edge radius cutting insert displayed close agreement to the experimental tests of the same cutting/geometrical conditions. The validation of the model was broken down into cutting forces and chip shape validations. Both validations of the model displayed acceptable results. In terms of cutting forces and chip shapes all edge radii displayed very similar results, and a clear differentiation was not noticeable between cutting inserts of different edge radii at the same cutting conditions, because of the small difference in edge radius sizes between the inserts. This is reasoned to the fact that the performance of inserts could not be measured after single revolution, which is what the 3D model simulated. Therefore, the presented model is able to provide tool designers with an apparatus to predict the average performance of cutting inserts during a single revolution without considering the failure of these inserts. Cutting inserts failure, occurs after many revolutions, which is near impossible to numerically simulate.

Also, within this chapter the impact of cutting conditions in terms of feed rates and cutting speeds on cutting forces was investigated. It was concluded that for all different variation of edge

Chapter 4: Numerical Simulation and Experimental Investigation

radii of cutting inserts an increase of feed rates and a decrease in cutting speeds, increases the chip load (feed per tooth) which directly increases cutting forces. The next chapter investigates the impact of cutting and geometrical conditions on the surface integrity of the experimentally machined workpiece.

Chapter 5: Effect of Tool Microgeometry and Cutting

Conditions on the Surface Integrity

5-1 Preamble

This chapter presents and discusses the results of investigating the impact of milling inserts microgeometry in terms of edge radius and cutting conditions, on the workpiece surface integrity during the milling of hardened AISI 4340 steel alloy. The quality of Machined parts is directly influenced by their surface integrity parameter. Therefore, it is crucial to study its impact to enhance the overall efficiency of the milling process. The research conducted in this thesis analyzes the surface integrity in terms of: 2D surface roughness, generated feed marks, subsurface plastic deformation, and subsurface microhardness.

5-2 The Significance of Surface Integrity and Experimental Analysis

Hardened AISI 4340 steel is widely employed in the automotive and aerospace industries, because of its desirable properties when heat treated to high hardness. Properties include high fatigue strength and high toughness and good resistance to corrosion and wear. This material composition contains iron, carbon, manganese, phosphorus, sulfur, silicon, nickel, chromium, and molybdenum. This combination of elements enhances the hardness of the steel along with its chemical and wear resistance. The surface quality of machined hardened AISI 4340 steel parts in the automotive and aerospace industries such as valves, vessels, various screws, etc. is crucial. Manufacturers always aim to produce high quality products at minimum cost. Machining processes affect the surface quality and integrity of parts; thus, studying the impact of machining parameters on the surface integrity of machined parts is extremely important.

Chapter 5: Effect of Tool Microgeometry and Cutting Conditions on The Surface Integrity

Surface integrity analysis was conducted on the machined surface obtained after each set of the previously described machining tests. Total of 30 machining tests were performed using five cutting tools with different edge radius ($25\ \mu\text{m}$, $30\ \mu\text{m}$, $35\ \mu\text{m}$, $40\ \mu\text{m}$, and $45\ \mu\text{m}$), two feed rates ($800\ \text{mm}/\text{min}$ and $1000\ \text{mm}/\text{min}$) and three cutting speeds ($75\ \text{m}/\text{min}$, $100\ \text{m}/\text{min}$, and $125\ \text{m}/\text{min}$). Each experiment included multiple runs on $150 \times 150 \times 25\ \text{mm}$ block shaped workpieces.

Inserts chipping and/or cutting distance were the constraints used to determine the number of runs for each experiment. Experiments of each cutting insert of a different edge radius began with the highest chip load, which occurred at a feed rate of $1000\ \text{mm}/\text{min}$ and a cutting speed of $75\ \text{m}/\text{min}$. Mainly, because high chip loads increase the chances of chipping. Then, when an insert is chipped it sets the maximum number of runs other inserts of the same edge radius must complete during the other five cutting combinations. But, if chipping occurs at under 30 runs which is around a distance of $3.0\ \text{m}$. Then, the other five cutting combinations of inserts of the same edge radius must complete a maximum of 30 runs if not chipped prior to 30 runs.

The 2D surface roughness was the first surface integrity parameter investigated. Measurements of the machined workpiece surface were performed using a Mitutoyo SJ-201 surface roughness tester. Figure 5-1 displays the tester measuring the newly machined workpiece. Each of the 30 experiments included a minimum of 30 runs (if the tool did not chip prior to that). Therefore, the cutting was paused every five runs to conduct 2D surface roughness measurements. Three measurements were taken at each run to check its reliability and repeatability. In addition, after every five runs the cutting inserts were examined for chipping /fracture and flank wear values were recorded using a Mitutoyo toolmaker's microscope (176-811A).

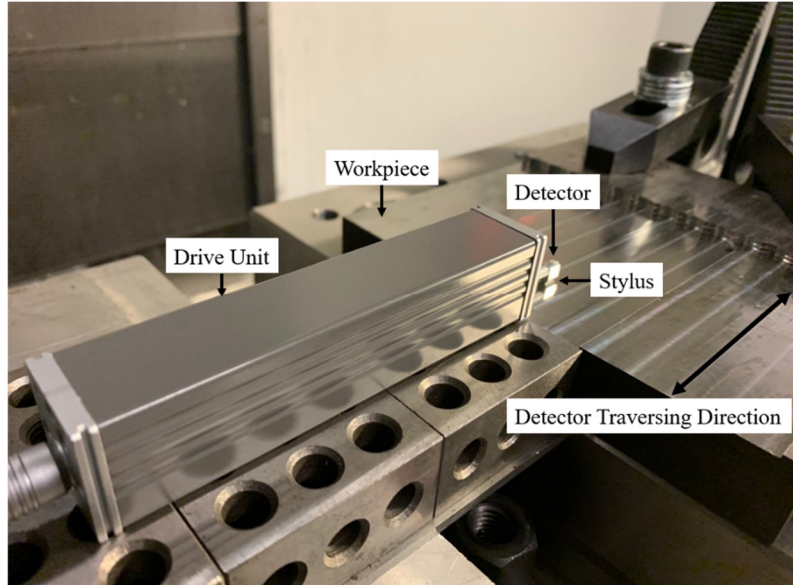


Figure 5-1: Surface Roughness Measurements Setup

To examine the machined surface and its subsurface, small rectangular specimens of $10 \times 10 \times 25 \text{ mm}$ were taken from the workpieces using wire electrical discharge machining (Wire EDM) to reduce the subsequent damage on the machined surface due to the sample removal. 18 samples were prepared all of which were from the cutting condition of 1000 mm/min feed rate and 75 m/min cutting speed, because to examine the impact of edge radius other geometrical parameters and cutting conditions must remain the same, while the edge radius is variable. Additionally, this specific cutting condition was chosen because it had the highest chip load per tooth and it presented the benchmark for the maximum number of runs other cutting conditions of the same edge radius needed complete.

Four specimens were taken from the workpiece of each edge radius. However, the $25 \mu\text{m}$ edge radius cutting insert had two specimens only because it chipped at the sixth run. Specimens were selected from each workpiece in a systematic order in which three to five runs separated each specimen. Figure 5-2 displays the Wire EDM cut specimens of the $45 \mu\text{m}$ edge radius milling

insert. This insert chipped at run 32. Therefore, small rectangular specimens were cut from runs: 18, 23, 28, and 32.

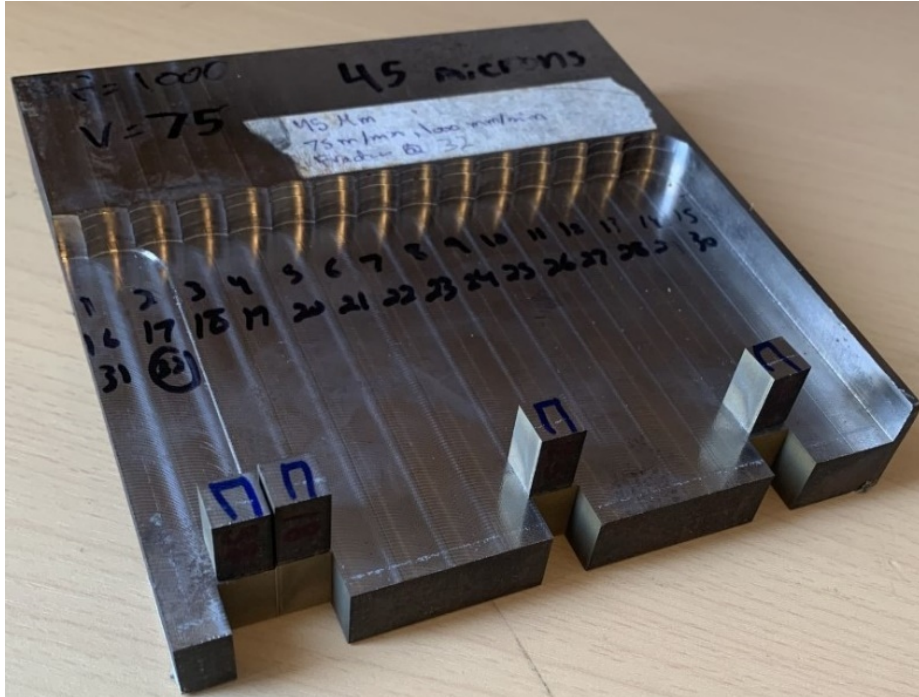


Figure 5-2: Specimens Cut Via Wire EDM

The impact of edge radius on the machined surface in terms of feed marks was captured using Leica DVM6 digital microscope shown in Figure 5-3. Then, specimens were cold mounted, polished, and etched to examine the subsurface plastic deformation (depth of cold working). Each specimen was mounted for 12 hours in struers epoxy, then progressively polished. The final polishing step was performed using 1 μm diamond slurry. Etching was conducted with a 4% nital for 5 seconds. Figure 5-4 presents a schematic of cold mounting a specimen.



Figure 5-3: Leica DVM6 Digital Microscope [60]

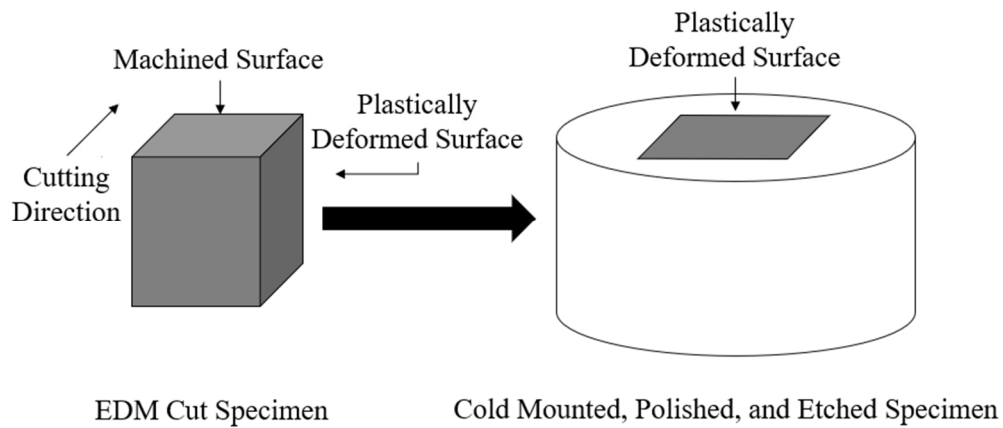


Figure 5-4: Schematic of a Wire EDM cut to Cold Mounted, Polished and Etched Specimen

The subsurface plastic deformation (depth of cold working) was analyzed using an XJP-403JT optical microscope as shown in Figure 5-5. Finally, the microhardness of specimens was measured using a SMHV-1000A digital microhardness tester. The tester is shown in Figure 5-6, and Figure 5-7 displays the placement of a cold mounted specimen on the tester.



Figure 5-5: XJP-403JT Optical Microscope



Figure 5-6: SMHV-1000A Digital Microhardness Tester

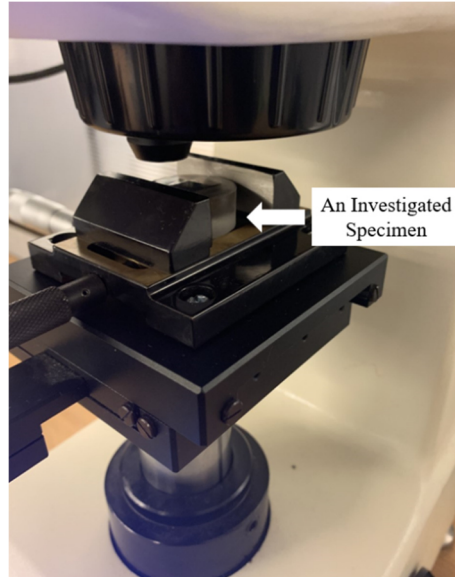


Figure 5-7: A Specimen in SMHV-1000A Digital Microhardness Tester

5-3 Effects of Edge Radius and Cutting Conditions on The Surface Roughness and Tool Flank Wear

Surface roughness is a major parameter that impacts the surface integrity of a machined surface [44]. Thoroughly investigating it allows manufacturers to run their machines at the highest production rate, while maintaining the required surface quality. Generally, surface roughness is described by two methods: The Arithmetic Mean Value (R_a) and the Root-Mean-Square Average (R_q). R_a , is the absolute average of the peaks and valleys heights across a sampling length (L_{sample}) measured from the mean line (M_L). While R_q , is the root mean square average of the profile height deviation from M_L over L_{sample} . The mathematical representation of both methods is presented in equations (5-1) and (5-2), q is a single sample measurement taken from the mean line M_L and j is the number of samples taken over the length L_{sample} . The relationship between R_a , R_q , M_L , and L_{sample} is displayed in Figure 5-8.

R_a is widely used more than R_q , because a single large peak flaw within the surface texture has greater effects on R_q than R_a . Therefore, R_a was selected to represent the surface roughness in this work.

$$R_a = q_a + q_b + q_c + \dots + q_j = \frac{1}{j} \sum_{i=1}^j q_i = \frac{1}{L_{sample}} \int_0^{L_{sample}} |q| dx \quad (5-1)$$

$$R_q = \sqrt{\frac{q_a^2 + q_b^2 + q_c^2 + \dots + q_j^2}{j}} = \sqrt{\frac{1}{j} \sum_{i=1}^j q_i^2} = \sqrt{\frac{1}{L_{sample}} \int_0^{L_{sample}} q^2 dx} \quad (5-2)$$

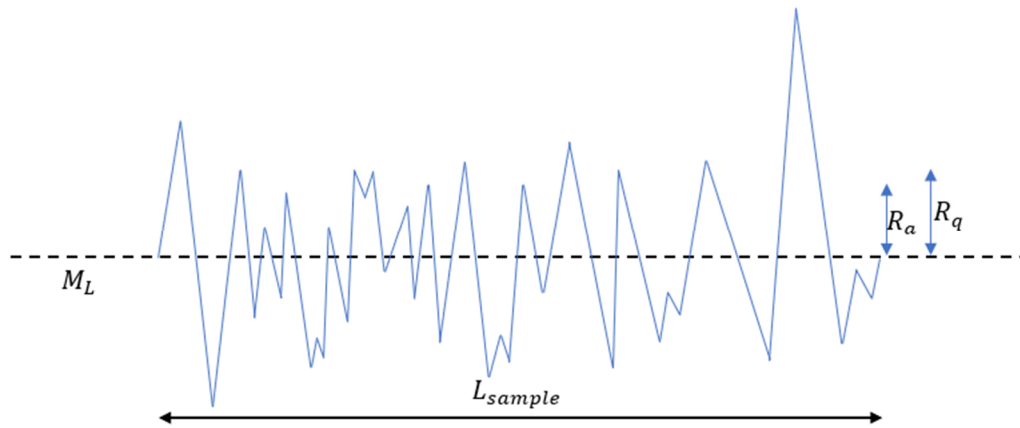


Figure 5-8: The Relationship of R_a , R_q , M_L , and L_{sample}

Measurements of R_a and tool flank wear (VB) were taken during down milling experimental tests. The cutoff length was 0.8 mm and at a measuring speed of 0.25 mm/s . For each run of every combination of edge radius and cutting conditions three R_a values were recorded. Then, the average value of the three measurements ($\overline{R_a}$) represented the roughness for that specific measurement. $\overline{R_a}$ and VB values in μm are displayed in Table 5-1 and Table 5-2. Each table presents $\overline{R_a}$ of five runs and measured value of VB . The flank wear value is measured at runs 5 and 20 in Table 5-1 and Table 5-2, respectively.

Chapter 5: Effect of Tool Microgeometry and Cutting Conditions on The Surface Integrity

Moreover, each surface roughness measurement at Table 5-1 is the average value of five total runs, which is the average of 15 measurements. Table 5-1 displays measurements taken for runs 1 to 5. Table 5-2 displays measurements taken for runs 16-20. Data was selected to be presented in this format to investigate the impact of cutting conditions and VB increase over time on $\overline{R_a}$.

Table 5-1: R_a μm (Runs 1-5) and VB μm (Run 5) Measurements

Feed Rate <i>mm/min</i>	Cutting Speed <i>m/min</i>	25 μm		30 μm		35 μm		40 μm		45 μm	
		$\overline{R_a}$	VB								
800	75	N/A	N/A	1.8	35	1.34	10	1.34	31	1.44	57
800	100	1.33	31	1.15	38	1.37	11	0.88	36	1.24	41
800	125	1.22	39	1.24	32	N/A	7	1.11	35	1.15	50
1000	75	1.34	35	2.08	31	1.49	29	1.63	38	1.78	40
1000	100	2.72	37	2.01	34	1.53	15	1.37	41	1.43	40
1000	125	0.99	38	1.55	41	1.29	32	1.27	39	1.03	53

Table 5-2: R_a μm (Runs 16-20) and VB μm (Run 20) Measurements

Feed Rate <i>mm/min</i>	Cutting Speed <i>m/min</i>	25 μm		30 μm		35 μm		40 μm		45 μm	
		$\overline{R_a}$	VB								
800	75	N/A	N/A	2.11	49	1.28	30	1.47	48	1.46	73
800	100	1.35	46	1.67	53	1.53	32	1.37	54	1.06	66
800	125	1.10	51	1.33	44	N/A	22	1.09	50	0.98	56
1000	75	N/A	N/A	2.01	42	1.53	48	1.79	61	1.59	52
1000	100	1.90	49	1.90	50	1.34	40	1.39	55	1.49	55
1000	125	1.77	62	1.70	63	0.96	52	0.76	59	1.24	72

Chapter 5: Effect of Tool Microgeometry and Cutting Conditions on The Surface Integrity

Missing measurements from both tables, indicated by N/A were due to tool chipping or failure prior capturing $\overline{R_a}$. However, at 800 *mm/min* and 125 *m/min* of the 35 μm edge radius inserts the first 50 measurements were not taken because, that workpiece was not leveled when all the other workpieces were leveled prior to the start of the experiments. Therefore, after that realization the 800 *mm/min* and 125 *m/min* of the 35 μm edge radius inserts workpiece was leveled and surface roughness measurements resumed.

Results from both tables indicate that in majority of cases, the $\overline{R_a}$ increases with increase of feed rates and decrease of cutting speeds. Also, increasing cutting speed increases *VB*, because higher cutting temperatures are observed at higher cutting speeds. Increasing feed rates increases chip loads which increase cutting forces. Increasing the cutting speed decrease the $\overline{R_a}$. Higher cutting speed prompt thermal softening effects, which makes it easier for the cutting insert to penetrate through the workpiece at higher temperatures. Also, lower forces are observed during higher cutting speed, because of the lower chip load.

Unlike feed rates and cutting speeds, fluctuating the edge radius did not have a great impact on $\overline{R_a}$ and a direct relationship between increasing and/or decrease the edge radius and $\overline{R_a}$ was not established. Which may be reason to the fact that the edge radius varies at maximum of 20 μm between the 25 μm and the 45 μm edge radii inserts. Thus, a 20 μm varying is not enough to display a significant change on the workpiece $\overline{R_a}$.

The increase in the distance of cut increased *VB* for every tool and each cutting condition. However, a noticeable change in the $\overline{R_a}$ between all cutting conditions was not observed, indicating the robustness of these inserts. Then, to further investigate the robustness of these inserts the milling insert of the 35 μm at 800 *mm/min* and 125 *m/min* cutting condition completed more

than 70 runs by travelling a cutting distance over 7.0 m. Then $\overline{R_a}$ and VB recorded at 1 μm and 65 μm , respectively. Results indicate that VB increased by 43 μm but $\overline{R_a}$ did not vary significantly in comparison to other $\overline{R_a}$ measurements of different edge radii tools of the same cutting conditions.

5-4 Effects of Edge Radius on the Feed Marks left on the machined Surface

Images of generated Feed marks were captured by a Leica DVM6 digital microscope. Specimens were chosen specifically to investigate the impact of edge radius on the surface integrity. Therefore, specimens were taken from workpieces that was machined using five different edge radii at the same cutting condition of 1000 mm/min and 75 m/min . Figure 5-9 to Figure 5-13 display the top view of the first run of the 25 μm edge radius insert, 31st run of the 30 μm edge radius insert, 35th run of the 35 μm edge radius insert, 22nd run of the 40 μm edge radius insert, and 23rd run of the 45 μm edge radius insert, respectively. Different runs are presented from each edge radius, because cutting inserts fractured after different number of runs.

Figures of all 18 specimens are presented in the order of increasing edge radius in Appendix A. In addition, Appendix A contains an additional 18 figures that display an enlarged portion of the generated feed marks, similar to Figure 5-14 of the 22nd run of the 40 μm edge radius insert. Figures of the zoomed-in portion enhanced the analysis by gaining a better understanding the size and distance of feed marks.

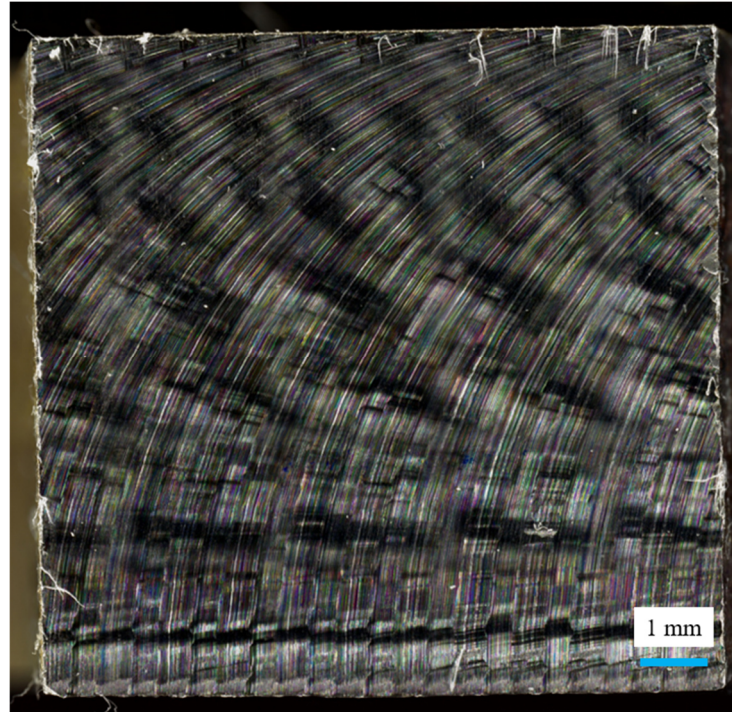


Figure 5-9: Run 1 Top View of a Machined Specimen Using a 25 μm Edge Radius Insert



Figure 5-10: Run 31 Top View of a Machined Specimen Using a 30 μm Edge Radius Insert

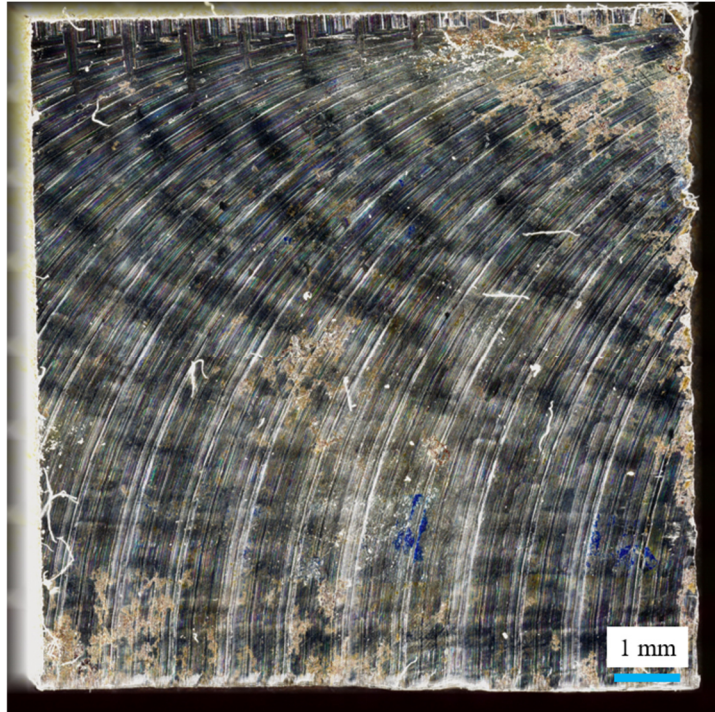


Figure 5-11: Run 31 Top View of a Machined Specimen Using a 35 μm Edge Radius Insert

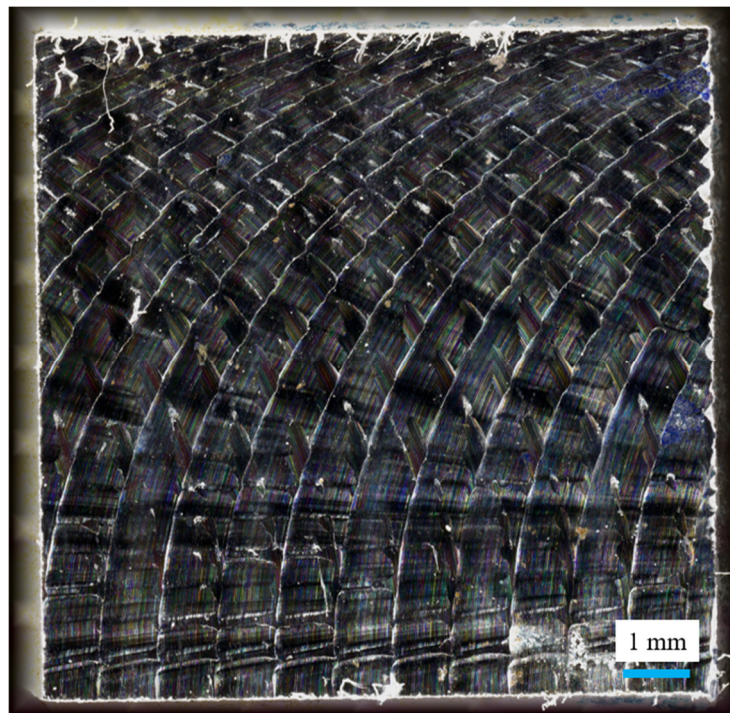


Figure 5-12: Run 22 Top View of a Machined Specimen Using a 40 μm Edge Radius Insert

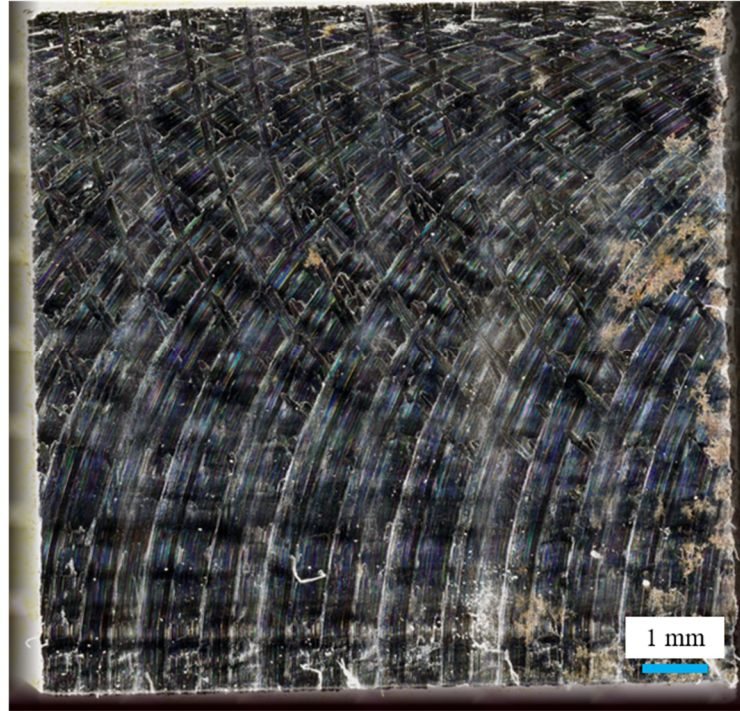


Figure 5-13: Run 23 Top View of a Machined Specimen Using a $45\ \mu\text{m}$ Edge Radius Insert

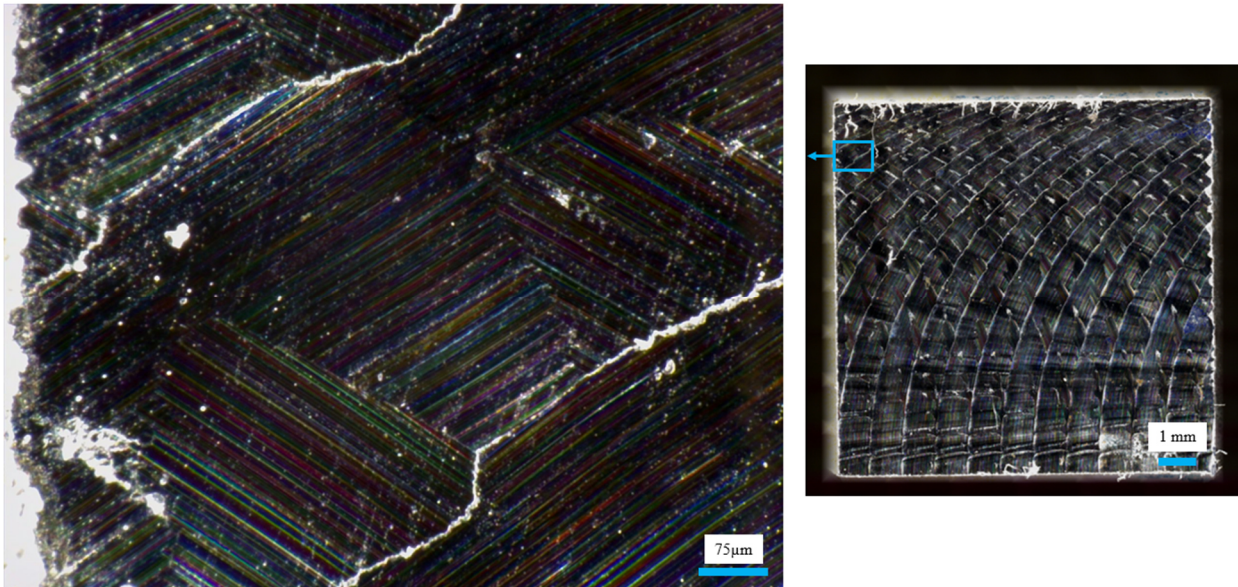


Figure 5-14: Zoomed-in Image of Run 22 Top View of a Machined Specimen Using a $40\ \mu\text{m}$ Edge Radius Insert

During the cutting process part of the workpiece material that is deforming elastically and plastically, reaches to a point in which it springs back after the cutting edge passes over it. Thus, the larger the edge radius the later the material arrives to this point [42]. Therefore, the visibility of feed marks increases with the increase of edge radius.

5-5 Effects of Edge Radius on The Subsurface Plastic Deformation and Subsurface Microhardness

Analyzing a machined workpiece subsurface after cutting provides the necessary information to investigate the elongation of grains, metallurgical changes, and the generated depth of cold working. Specimens were analyzed using an XJP-403JT optical microscope. Figure 5-16, Figure 5-17, Figure 5-18, and Figure 5-19 display the microstructure of fifth run of the 25 μm edge radius insert, 31st run of the 30 μm edge radius insert, 31st run of the 35 μm edge radius insert, 22nd run of the 40 μm edge radius insert, and 32nd run of the 45 μm edge radius insert, respectively. Figures of all 18 specimens are presented in the order of increasing edge radius in Appendix B.

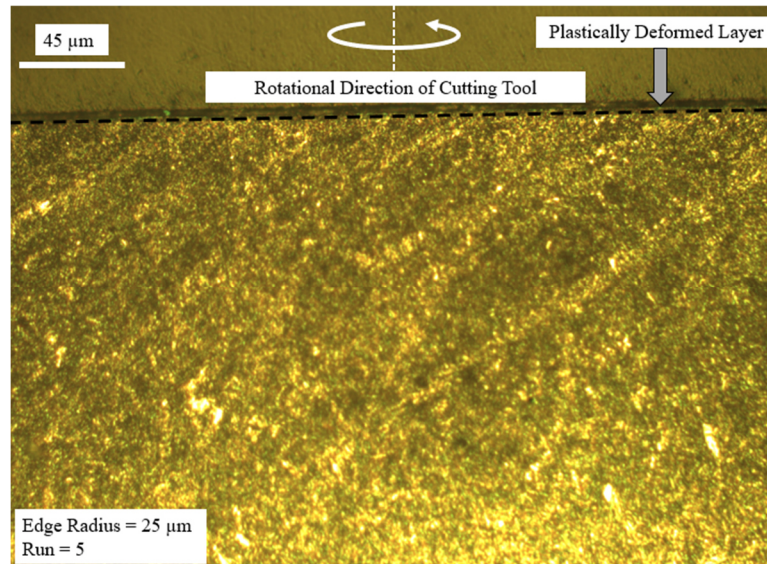


Figure 5-15: Subsurface Microstructure of a Machined Specimen Using a 25 μm Edge Radius Insert

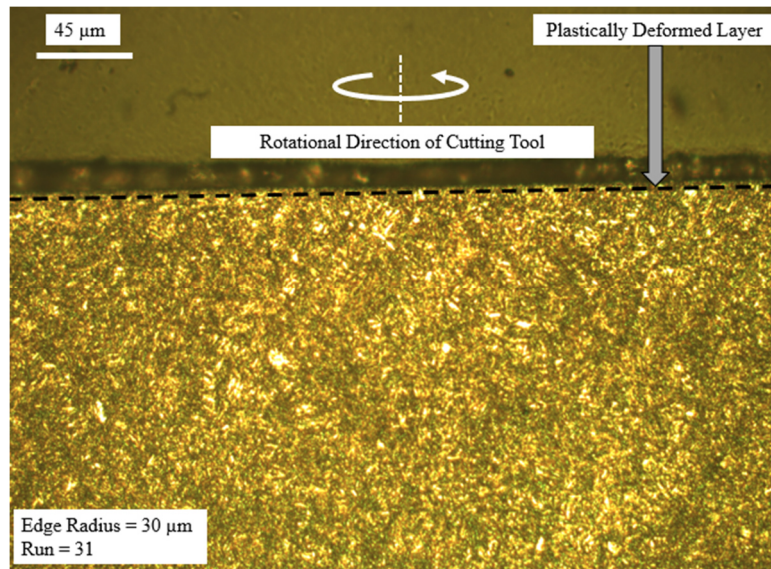


Figure 5-16: Subsurface Microstructure of a Machined Specimen Using a 30 μm Edge Radius Insert

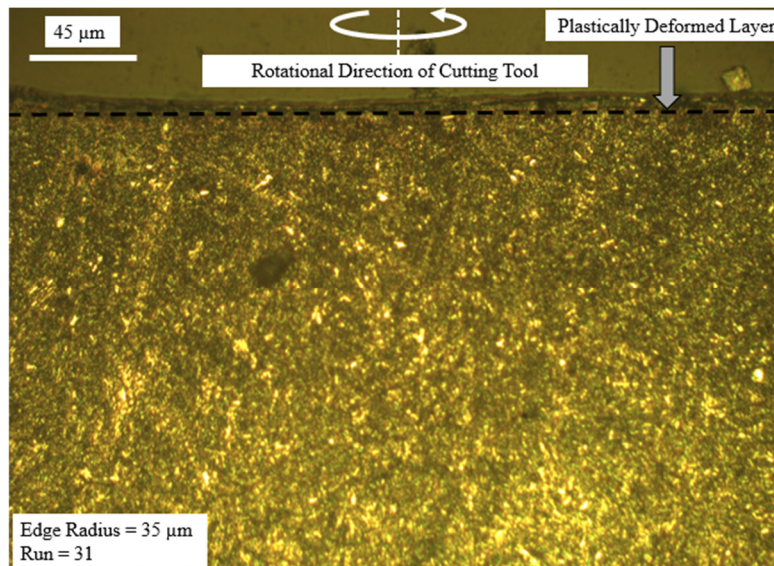


Figure 5-17: Subsurface Microstructure of a Machined Specimen Using a 35 μm Edge Radius Insert

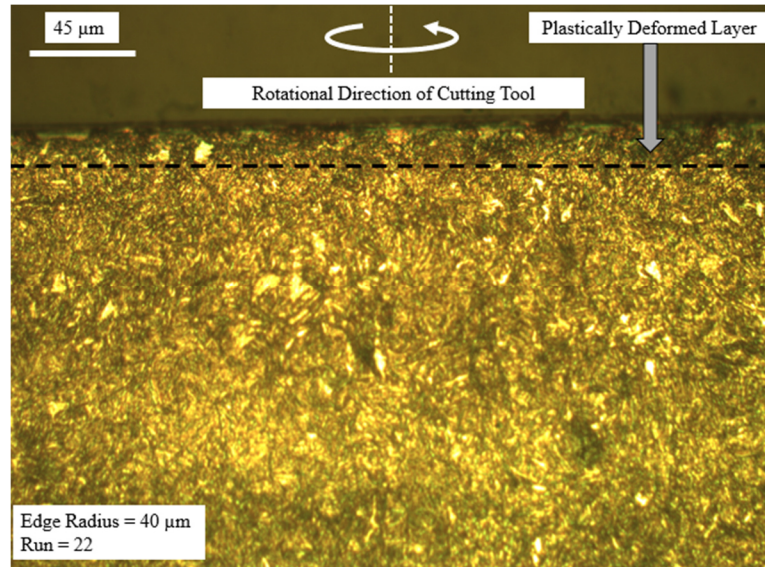


Figure 5-18: Subsurface Microstructure of a Machined Specimen Using a 40 μm Edge Radius Insert

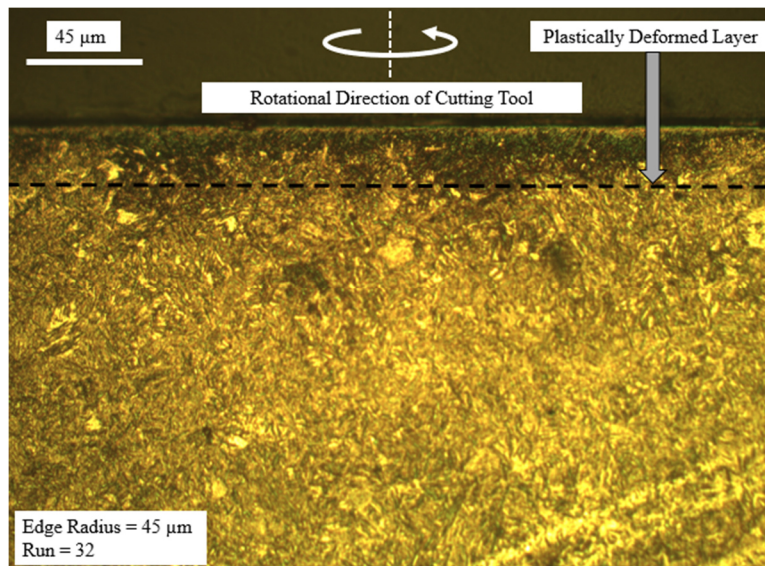


Figure 5-19: Subsurface Microstructure of a Machined Specimen Using a 45 μm Edge Radius Insert

Images taken of all 18 specimens display martensite crystalline structure. Martensite crystalline structure was expected, because of the workpiece material hardening process. In addition, analyzed results show that depth of cold working increases with the increase of edge radius. This phenomenon occurs because as the edge radius increases the contact length between the tool flank

face and the workpiece surface also increases, compressing larger amount of material. Milling the workpiece with the 25 μm edge radius milling insert did not result in significant strain hardening deformation. However, a considerable depth of cold working was generated when the workpiece material was cut by the 45 μm milling insert. The average measured depth of cold working was approximately 20 μm for the workpiece Machined by the 45 μm radius.

Microhardness readings beneath the cut surface of specimens that were machined by different edge radii are presented in Figure 5-20. It displays the recorded measurements and their trends. Approximately 15 measurements were recorded for each specimen, starting from a depth of around 10 μm from beneath the Machined surface. Measurements were taken at an indentation time of 15 s and a load of 0.5 kg. All measurements were crosschecked by taking different sets of measurements at the same depth.

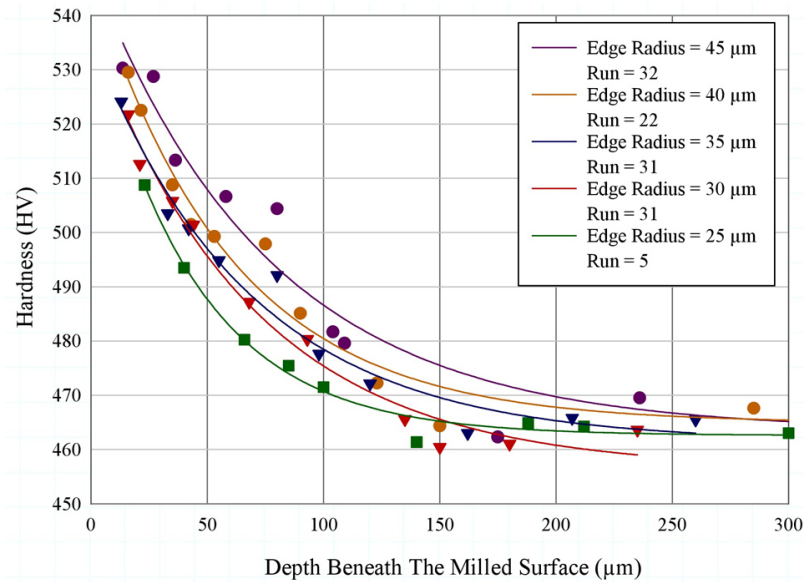


Figure 5-20: Experimentally Captured and Recorded Microhardness Readings

Findings indicate that microhardness readings for all edge radii are much higher right beneath the machined subsurface in comparison to measurements taken further in the bulk of material, implying the impact of work hardening generated by the shear plastic strain of material. Additionally, increasing the edge radius increases the microhardness readings beneath the machined surface. This is attributed to the fact that larger edge radius increases the contact between the insert's flank face and the newly generated surface. Then, due to the ploughing effect, the material compresses significantly, resulting in higher microhardness readings for higher edge radii inserts. Moreover, at around 120 μm below the surface microhardness, readings from all specimens begin to neutralize to around 460-470 HV. That is equivalent to 47 ± 1 (HRC), which is the original hardness of the workpiece material prior to milling. Indicating that the impact of work hardening is mainly significant right below the machined surface.

5-6 Summary

Workpiece surface integrity was analyzed in terms of: 2D surface roughness, generated feed marks, subsurface plastic deformation, and subsurface microhardness. Impact of cutting conditions and milling insert edge radius indicated that the roughness increases with increasing the feed rate and decreasing the cutting speed, and vice versa. However, changes in edge radius did not present a significant impact on the surface roughness. Moreover, varying the edge radius had a notable impact on generated feed marks, subsurface plastic deformation, and subsurface microhardness. Feed marks became more visible with increasing the edge radius, while depth of cold working and microhardness increased with the increase of edge radius.

Chapter 6: Conclusions and Future works

6-1 Conclusions

The main objective of this thesis is focused on the simulation of milling operations and investigation the impact of edge radius and cutting conditions on the Machined workpiece surface integrity. Main findings and contributions of this thesis are summarized in this chapter and a road map for future works is outlined.

This thesis developed and presented a 3D FEA model of milling operations, and an extensive analysis on the impact of edge radius and cutting conditions on the surface integrity of Machined hardened steels.

Tool designers and manufactures can utilize FEA models to investigate the impact of cutting/ tool geometrical conditions properly, and capture results that are impossible/ or difficult to capture analytically and experimentally. Such as: stress distribution, temperature distribution, tool/chip contact length, cutting forces, etc. Initially, the importance of metal cutting simulation models was discussed, and gaps within the literature were highlighted by conducting an in-depth literature review of available FEA models. Then, methodologies utilized within the metal cutting field were reviewed exhaustively. These methods make up the bases for the development of FEA models. Methodologies included: formulation types, time integration schemes, material models, chip generation techniques, J-C fracture model, friction models and widely used FEA packages. Main concluding remarks of the FEA model development are:

- A 3D FEA model that duplicated a down milling process was thoroughly setup and validated. Down milling was selected because experiments conducted in this work were

Chapter 6: Conclusions and Future Works

the experimental parameters used in another research project that occurred parallel to this research project. The other research project studied milling inserts failure by chipping. Which, is enhanced during down milling due to the high impact inserts experience during each rotation.

- The validation process of the model was conducted in terms of cutting forces and chip morphology. A close agreement of 11.3% was observed between the average numerical and experimental cutting resultant forces.
- Serrated (saw-toothed) chip shape was observed in numerical simulations and experimental tests, providing an additional layer of validation.

Afterwards, the impact of edge radius on the surface integrity of hardened steels was analyzed experimentally. Since, proper analyzation of the edge radius impact on the surface integrity can provide tool designers, with information to select the proper edge radius for their specific conditions. Investigated characteristics of surface integrity were: 2D surface roughness, feed marks visibility, subsurface plastic deformation (depth of cold working), and microhardness. Impact of cutting conditions was also explored when examining 2D surface roughness measurements. Main concluding remarks of investigating of process parameters on the surface integrity are:

- The surface roughness increases with increasing the feed rate and decreasing the cutting speed, and vice versa. Nevertheless, varying edge radii did not present significant impact on the surface roughness.
- Changing the edge radius generated an obvious impact on the generated feed marks, subsurface plastic deformation, and subsurface microhardness. Feed marks became

more visible with increasing the edge radius, while depth of cold working and microhardness increased with the increase of edge radius.

6-2 Future Works

Future works of this research should be focused on the following items:

1. Expanding and evolving the 3D FEA model to include characteristics of tool wear and surface integrity in terms of depth of cold working.
2. Investigated 3D FEA model and the surface integrity analysis were done using dry conditions. However, majority of industrial metal cutting operations are conducted while using coolant. Therefore, works may be expanded by including the impact of coolant within the developed 3D FEA model and the analyzed parameters.

References

- [1] A. Hosseini and H. Kishawy, "On the optimized design of broaching tools," *Journal of Manufacturing Science and Engineering*, vol. 136, no. 1, 2014.
- [2] S. Kalpakjian and S. R. Schmid, *Manufacturing processes for engineering materials*, 6th ed. Pearson Education 2017.
- [3] Y. N. Zarif, "Cutting Edge Microgeometry, Modeling and EE-Honing," 2012.
- [4] S. A. Hosseini, "Model based simulation of broaching operation: cutting mechanics, surface integrity, and process optimization," 2013.
- [5] L. Pang, A. Hosseini, H. Hussein, I. Deiab, and H. Kishawy, "Application of a new thick zone model to the cutting mechanics during end-milling," *International Journal of Mechanical Sciences*, vol. 96, pp. 91-100, 2015.
- [6] S. M. Tanu Halim, "Finite element modeling of the orthogonal metal cutting process: modeling the effects of coefficient of friction and tool holding structure on cutting forces and chip thickness," 2008.
- [7] N. Yussefian, A. Hosseini, K. Hosseinkhani, and H. Kishawy, "Design for Manufacturing of Variable Microgeometry Cutting Tools," *Journal of Manufacturing Science and Engineering*, vol. 140, no. 1, p. 011014, 2018.
- [8] M. Padmakumar, "Effect of cutting edge form factor (K-factor) on the performance of a face milling tool," *CIRP Journal of Manufacturing Science and Technology*, 2020.
- [9] T. Zhao, J. Zhou, V. Bushlya, and J. Ståhl, "Effect of cutting edge radius on surface roughness and tool wear in hard turning of AISI 52100 steel," *The International Journal of Advanced Manufacturing Technology*, vol. 91, no. 9-12, pp. 3611-3618, 2017.
- [10] G. M. Pittalà and M. Monno, "3D finite element modeling of face milling of continuous chip material," *The International Journal of Advanced Manufacturing Technology*, vol. 47, no. 5-8, pp. 543-555, 2010.
- [11] T. Özel and E. Zeren, "Finite element modeling the influence of edge roundness on the stress and temperature fields induced by high-speed machining," *The International Journal of Advanced Manufacturing Technology*, vol. 35, no. 3-4, pp. 255-267, 2007.
- [12] A. Ramesh and S. N. Melkote, "Modeling of white layer formation under thermally dominant conditions in orthogonal machining of hardened AISI 52100 steel," *International Journal of Machine Tools and Manufacture*, vol. 48, no. 3-4, pp. 402-414, 2008.
- [13] G. Chen, C. Ren, X. Yang, X. Jin, and T. Guo, "Finite element simulation of high-speed machining of titanium alloy (Ti-6Al-4V) based on ductile failure model," *The International Journal of Advanced Manufacturing Technology*, vol. 56, no. 9-12, pp. 1027-1038, 2011.

References

- [14] Y. Xi, M. Bermingham, G. Wang, and M. Dargusch, "Finite element modeling of cutting force and chip formation during thermally assisted machining of Ti6Al4V alloy," *Journal of Manufacturing Science and Engineering*, vol. 135, no. 6, 2013.
- [15] A. Ghandehariun, M. Nazzal, H. Kishawy, and U. Umer, "On modeling the deformations and tool-workpiece interactions during machining metal matrix composites," *The International Journal of Advanced Manufacturing Technology*, vol. 91, no. 5-8, pp. 1507-1516, 2017.
- [16] C. Maranhão and J. P. Davim, "Finite element modelling of machining of AISI 316 steel: numerical simulation and experimental validation," *Simulation Modelling Practice and Theory*, vol. 18, no. 2, pp. 139-156, 2010.
- [17] L. Jiang and D. Wang, "Finite-element-analysis of the effect of different wiper tool edge geometries during the hard turning of AISI 4340 steel," *Simulation Modelling Practice and Theory*, vol. 94, pp. 250-263, 2019.
- [18] T. Özel and T. Altan, "Process simulation using finite element method—prediction of cutting forces, tool stresses and temperatures in high-speed flat end milling," *International Journal of Machine Tools and Manufacture*, vol. 40, no. 5, pp. 713-738, 2000.
- [19] C. Wang, F. Ding, D. Tang, L. Zheng, S. Li, and Y. Xie, "Modeling and simulation of the high-speed milling of hardened steel SKD11 (62 HRC) based on SHPB technology," *International Journal of Machine Tools and Manufacture*, vol. 108, pp. 13-26, 2016.
- [20] Y.-C. Yen, A. Jain, and T. Altan, "A finite element analysis of orthogonal machining using different tool edge geometries," *Journal of materials processing technology*, vol. 146, no. 1, pp. 72-81, 2004.
- [21] E.-G. Ng, T. I. El-Wardany, M. Dumitrescu, and M. A. Elbestawi, "Physics-based simulation of high speed machining," *Machining science and technology*, vol. 6, no. 3, pp. 301-329, 2002.
- [22] S. Soo, D. Aspinwall, and R. Dewes, "3D FE modelling of the cutting of Inconel 718," *Journal of Materials Processing Technology*, vol. 150, no. 1-2, pp. 116-123, 2004.
- [23] X. Zhang, S. Wu, H. Wang, and C. R. Liu, "Predicting the effects of cutting parameters and tool geometry on hard turning process using finite element method," *Journal of Manufacturing Science and Engineering*, vol. 133, no. 4, 2011.
- [24] R. Li and A. J. Shih, "Finite element modeling of 3D turning of titanium," *The International Journal of Advanced Manufacturing Technology*, vol. 29, no. 3-4, p. 253, 2006.
- [25] J. Ma, N. H. Duong, and S. Lei, "3D numerical investigation of the performance of microgroove textured cutting tool in dry machining of Ti-6Al-4V," *The international journal of advanced manufacturing technology*, vol. 79, no. 5-8, pp. 1313-1323, 2015.

References

- [26] J. Aurich and H. Bil, "3D finite element modelling of segmented chip formation," *CIRP annals*, vol. 55, no. 1, pp. 47-50, 2006.
- [27] T. Özel, "Computational modelling of 3D turning: Influence of edge micro-geometry on forces, stresses, friction and tool wear in PcBN tooling," *Journal of Materials Processing Technology*, vol. 209, no. 11, pp. 5167-5177, 2009.
- [28] R. K. Yadav, K. Abhishek, and S. S. Mahapatra, "A simulation approach for estimating flank wear and material removal rate in turning of Inconel 718," *Simulation Modelling Practice and Theory*, vol. 52, pp. 1-14, 2015.
- [29] S. L. Soo, R. C. Dewes, and D. K. Aspinwall, "3D FE modelling of high-speed ball nose end milling," *The International Journal of Advanced Manufacturing Technology*, vol. 50, no. 9-12, pp. 871-882, 2010.
- [30] B. Rao, C. R. Dandekar, and Y. C. Shin, "An experimental and numerical study on the face milling of Ti-6Al-4V alloy: Tool performance and surface integrity," *Journal of Materials Processing Technology*, vol. 211, no. 2, pp. 294-304, 2011.
- [31] H. Wu and S. Zhang, "3D FEM simulation of milling process for titanium alloy Ti6Al4V," *The International Journal of Advanced Manufacturing Technology*, vol. 71, no. 5-8, pp. 1319-1326, 2014.
- [32] T. Thepsonthi and T. Özel, "3-D finite element process simulation of micro-end milling Ti-6Al-4V titanium alloy: experimental validations on chip flow and tool wear," *Journal of Materials Processing Technology*, vol. 221, pp. 128-145, 2015.
- [33] A. Davoudinejad, D. Li, Y. Zhang, and G. Tosello, "Optimization of corner micro end milling by finite element modelling for machining thin features," *Procedia CIRP*, vol. 82, pp. 362-367, 2019.
- [34] G. Bolar and S. N. Joshi, "Three-dimensional numerical modeling, simulation and experimental validation of milling of a thin-wall component," *Proceedings of the Institution of Mechanical Engineers, Part B: Journal of Engineering Manufacture*, vol. 231, no. 5, pp. 792-804, 2017.
- [35] Q. Zhang, S. Zhang, and J. Li, "Three dimensional finite element simulation of cutting forces and cutting temperature in hard milling of AISI H13 steel," *Procedia Manufacturing*, vol. 10, pp. 37-47, 2017.
- [36] J. T. Black and R. A. Kohser, *DeGarmo's materials and processes in manufacturing*, 11 ed. John Wiley & Sons, 2011.
- [37] J. P. Davim, *Surface integrity in machining*. Springer, 2010.
- [38] J. Hughes, A. Sharman, and K. Ridgway, "The effect of tool edge preparation on tool life and workpiece surface integrity," *Proceedings of the Institution of Mechanical Engineers, Part B: Journal of Engineering Manufacture*, vol. 218, no. 9, pp. 1113-1123, 2004.

References

- [39] Z. Pu, J. Outeiro, A. Batista, O. Dillon, D. Puleo, and I. Jawahir, "Surface integrity in dry and cryogenic machining of AZ31B Mg alloy with varying cutting edge radius tools," *Procedia Engineering*, vol. 19, pp. 282-287, 2011.
- [40] B. Denkena, T. Grove, and O. Maiss, "Influence of the cutting edge radius on surface integrity in hard turning of roller bearing inner rings," *Production Engineering*, vol. 9, no. 3, pp. 299-305, 2015.
- [41] B. Denkena, J. Koehler, and M. Rehe, "Influence of the honed cutting edge on tool wear and surface integrity in slot milling of 42CrMo4 steel," *Procedia CIRP*, vol. 1, pp. 190-195, 2012.
- [42] C.-F. Wyen, D. Jaeger, and K. Wegener, "Influence of cutting edge radius on surface integrity and burr formation in milling titanium," *The International Journal of Advanced Manufacturing Technology*, vol. 67, no. 1-4, pp. 589-599, 2013.
- [43] J. Fulemova and Z. Janda, "Influence of the cutting edge radius and the cutting edge preparation on tool life and cutting forces at inserts with wiper geometry," *Procedia Engineering*, vol. 69, pp. 565-573, 2014.
- [44] B. Li, S. Zhang, Z. Yan, and D. Jiang, "Influence of edge hone radius on cutting forces, surface integrity, and surface oxidation in hard milling of AISI H13 steel," *The International Journal of Advanced Manufacturing Technology*, vol. 95, no. 1-4, pp. 1153-1164, 2018.
- [45] T. T. Opoz and X. Chen, "Chip formation mechanism using finite element simulation," *Strojniški vestnik-Journal of Mechanical Engineering*, vol. 62, no. 11, 2016.
- [46] G. R. Johnson, "A constitutive model and data for materials subjected to large strains, high strain rates, and high temperatures," *Proc. 7th Int. Sympo. Ballistics*, pp. 541-547, 1983.
- [47] F. J. Zerilli and R. W. Armstrong, "Dislocation-mechanics-based constitutive relations for material dynamics calculations," *Journal of applied physics*, vol. 61, no. 5, pp. 1816-1825, 1987.
- [48] G. R. Johnson and W. H. Cook, "Fracture characteristics of three metals subjected to various strains, strain rates, temperatures and pressures," *Engineering fracture mechanics*, vol. 21, no. 1, pp. 31-48, 1985.
- [49] K. Wang, "Calibration of the Johnson-Cook failure parameters as the chip separation criterion in the modelling of the orthogonal metal cutting process," 2016.
- [50] A. Hillerborg, M. Modéer, and P.-E. Petersson, "Analysis of crack formation and crack growth in concrete by means of fracture mechanics and finite elements," *Cement and concrete research*, vol. 6, no. 6, pp. 773-781, 1976.
- [51] N. Zorev, "Inter-relationship between shear processes occurring along tool face and shear plane in metal cutting," *International research in production engineering*, vol. 49, pp. 143-152, 1963.

References

- [52] A. Priyadarshini, S. K. Pal, and A. K. Samantaray, "Influence of the Johnson Cook material model parameters and friction models on simulation of orthogonal cutting process," *Journal of Machining and Forming Technologies*, vol. 4, no. 1/2, pp. 59-83, 2012.
- [53] J. Rodríguez, J. Carbonell, and P. Jonsen, "Numerical methods for the modelling of chip formation," *Archives of Computational Methods in Engineering*, pp. 1-26, 2018.
- [54] R. T. Coelho, E.-G. Ng, and M. Elbestawi, "Tool wear when turning hardened AISI 4340 with coated PCBN tools using finishing cutting conditions," *International Journal of Machine Tools and Manufacture*, vol. 47, no. 2, pp. 263-272, 2007.
- [55] "CoroMill® 390 insert for milling-R390-11 T3 04M-PM 1130." SANDVIK Coromant. https://www.sandvik.coromant.com/en-gb/products/pages/productdetails.aspx?c=r390-11%20t3%2004m-pm%201130&gclid=EAIaIQobChMIzonGwf_g5wIVj-NkCh1pxggqEAAYASAAEgKP_PD_BwE (accessed 2020).
- [56] "CoroMill® 390 square shoulder milling cutter-R390R390-020A20-11L." SANDVIK Coromant. https://www.sandvik.coromant.com/en-gb/products/pages/productdetails.aspx?c=R390-020A20-11L&gclid=EAIaIQobChMIspiw5v7g5wIVsSCtBh2NVA5REAAAYASAAEgKhEvD_BwE (accessed 2020).
- [57] H. A. Kishawy, T. DesRoches, A. Hosseini, T. El-Wardany, and C. Guo, "Generic method to determine coefficients of mechanistic milling force model," *International Journal of Manufacturing Research*, vol. 8, no. 1, pp. 43-63, 2013.
- [58] H. A. Kishawy and A. Hosseini, *Machining Difficult-to-Cut Materials: Basic Principles and Challenges*. Springer, 2018.
- [59] A. Hosseini, B. Moetakef-Imani, and H. Kishawy, "Mechanistic modelling for cutting with serrated end mills—a parametric representation approach," *Proceedings of the Institution of Mechanical Engineers, Part B: Journal of Engineering Manufacture*, vol. 225, no. 7, pp. 1019-1032, 2011.
- [60] L. Microsystems. "Digital Microscope Leica DVM6." <https://www.leica-microsystems.com/products/digital-microscopes/p/leica-dvm6/> (accessed 2020).

Appendix A. Feed Marks Figures

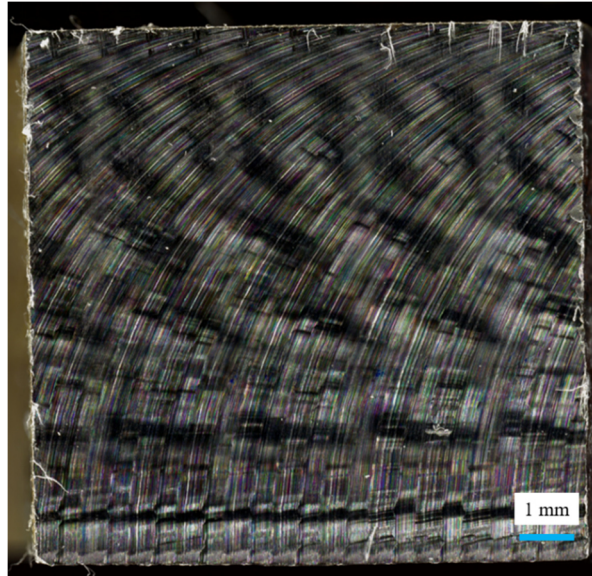


Figure A-1: Run 1 Top View of a Machined Specimen Using a 25 μm Edge Radius Insert

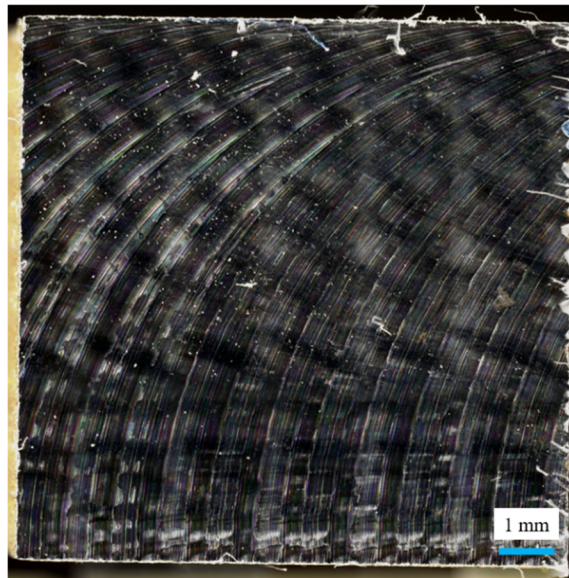


Figure A-2: Run 5 Top View of a Machined Specimen Using a 25 μm Edge Radius Insert

Appendix A. Feed Marks Figures

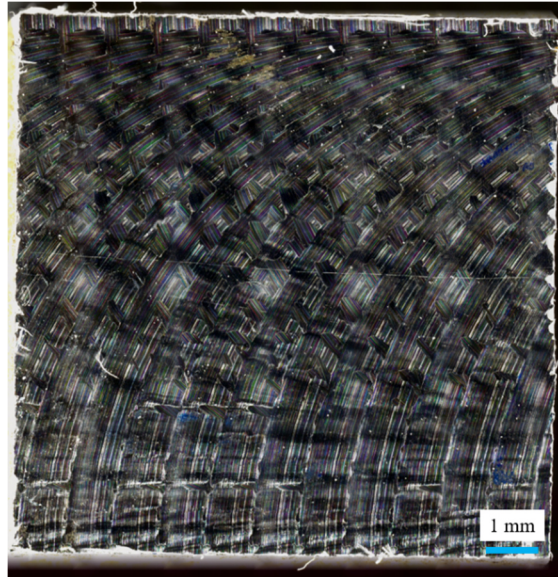


Figure A-3: Run 21 Top View of a Machined Specimen Using a 30 μm Edge Radius Insert

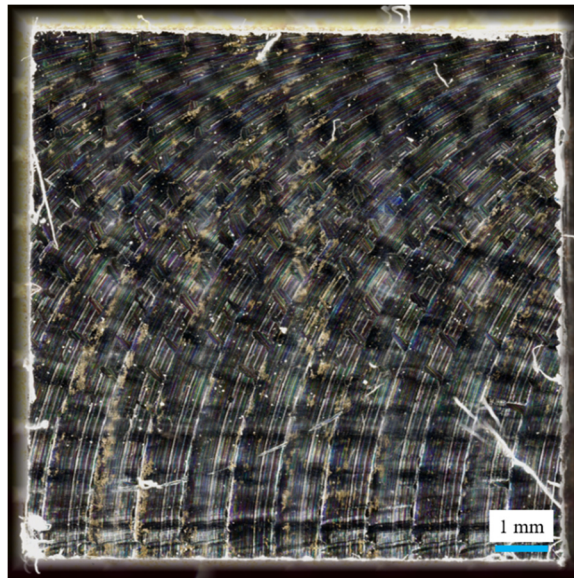


Figure A-4: Run 26 Top View of a Machined Specimen Using a 30 μm Edge Radius Insert

Appendix A. Feed Marks Figures



Figure A-5: Run 31 Top View of a Machined Specimen Using a $30\ \mu\text{m}$ Edge Radius Insert

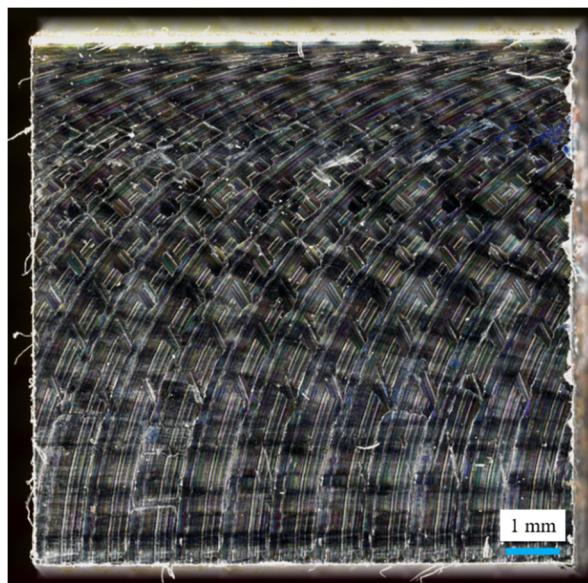


Figure A-6: Run 35 Top View of a Machined Specimen Using a $30\ \mu\text{m}$ Edge Radius Insert

Appendix A. Feed Marks Figures

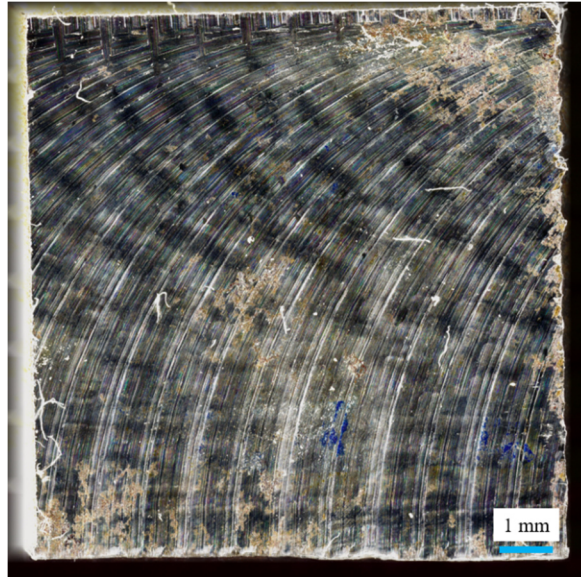


Figure A-7: Run 31 Top View of a Machined Specimen Using a $35\ \mu\text{m}$ Edge Radius Insert

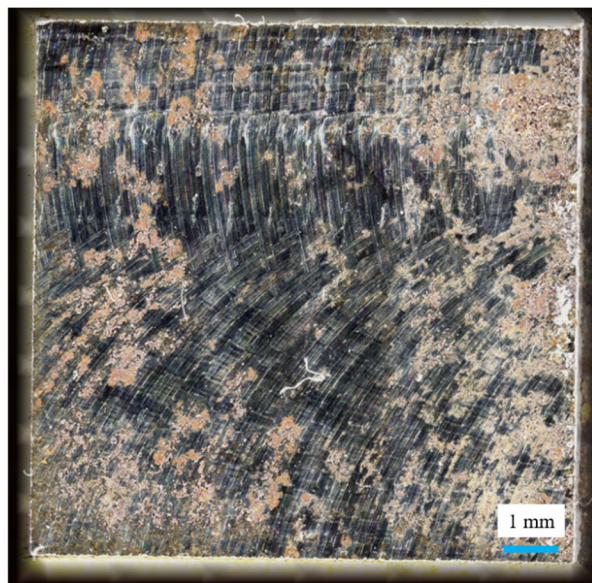


Figure A-8: Run 36 Top View of a Machined Specimen Using a $35\ \mu\text{m}$ Edge Radius Insert

Appendix A. Feed Marks Figures

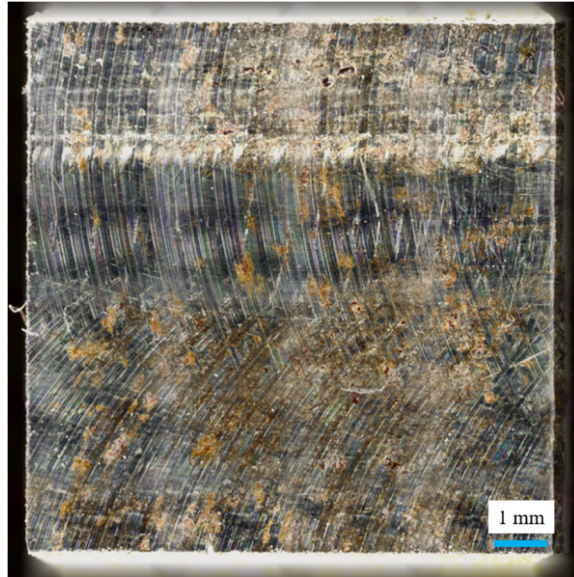


Figure A-9: Run 41 Top View of a Machined Specimen Using a 35 μm Edge Radius Insert

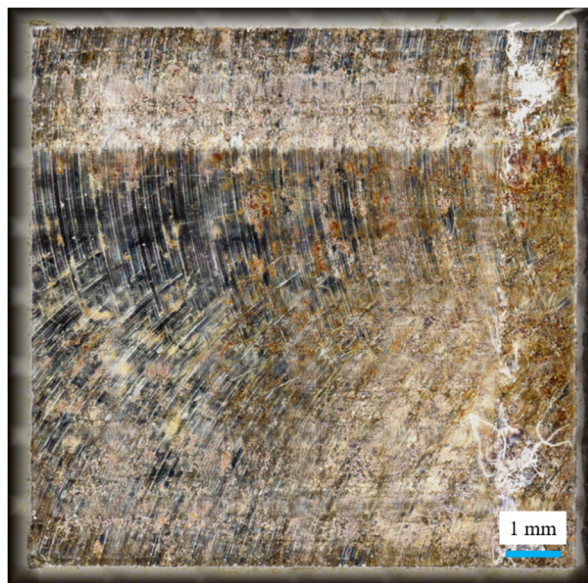


Figure A-10: Run 45 Top View of a Machined Specimen Using a 35 μm Edge Radius Insert

Appendix A. Feed Marks Figures

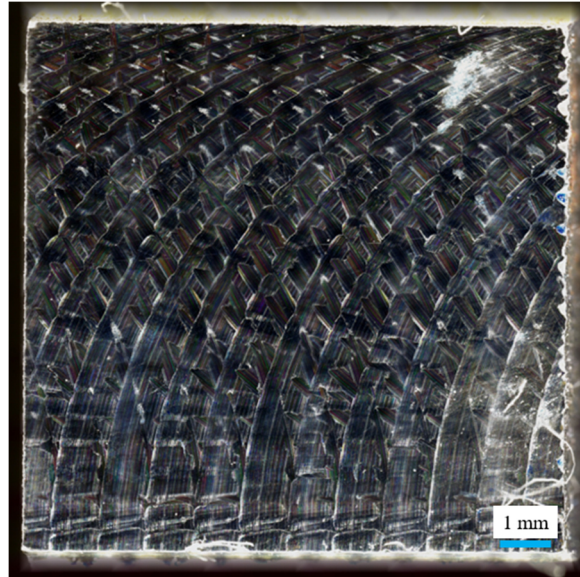


Figure A-11: Run 8 Top View of a Machined Specimen Using a 40 μm Edge Radius Insert

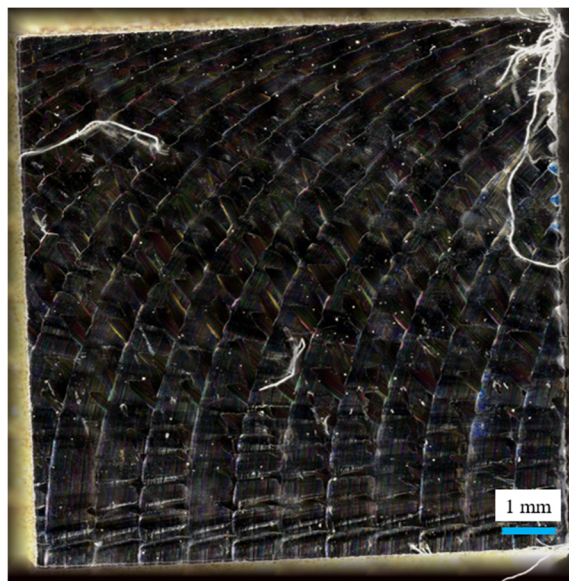


Figure A-12: Run 13 Top View of a Machined Specimen Using a 40 μm Edge Radius Insert

Appendix A. Feed Marks Figures

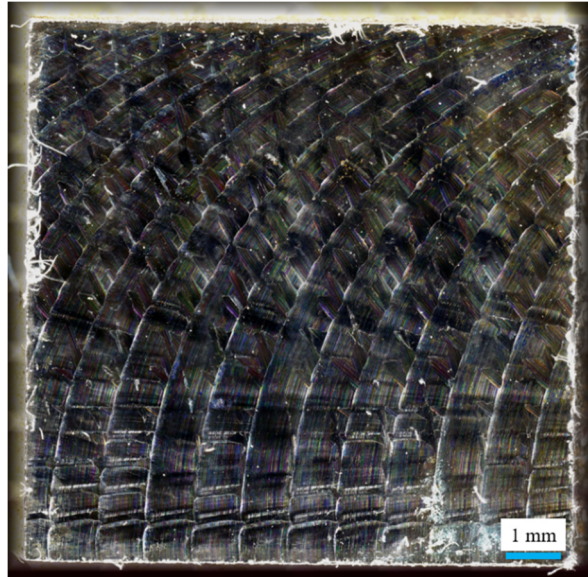


Figure A-13: Run 18 Top View of a Machined Specimen Using a 40 μm Edge Radius Insert

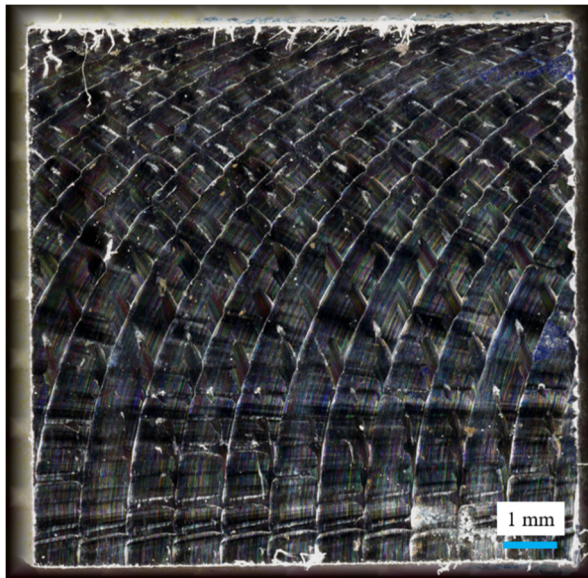


Figure A-14: Run 22 Top View of a Machined Specimen Using a 40 μm Edge Radius Insert

Appendix A. Feed Marks Figures

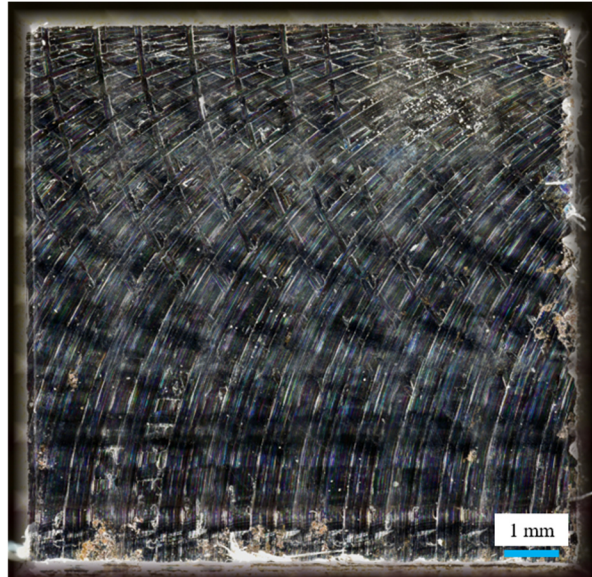


Figure A-15: Run 18 Top View of a Machined Specimen Using a $45\ \mu\text{m}$ Edge Radius Insert

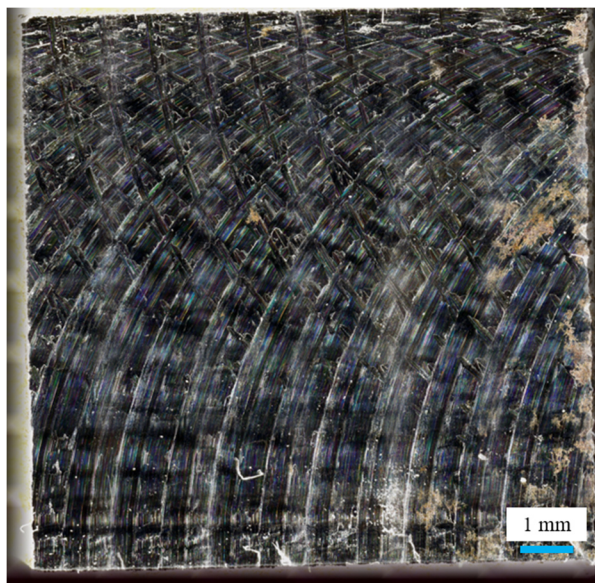


Figure A-16: Run 23 Top View of a Machined Specimen Using a $45\ \mu\text{m}$ Edge Radius Insert

Appendix A. Feed Marks Figures

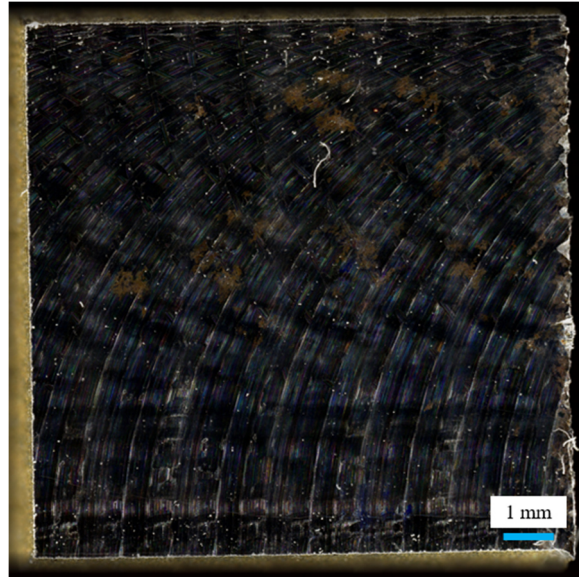


Figure A-17: Run 28 Top View of a Machined Specimen Using a $45\ \mu\text{m}$ Edge Radius Insert

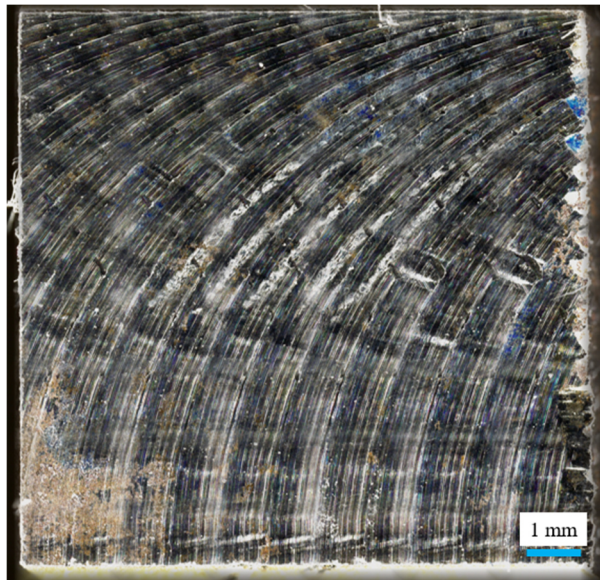


Figure A-18: Run 32 Top View of a Machined Specimen Using a $45\ \mu\text{m}$ Edge Radius Insert

Appendix A. Feed Marks Figures

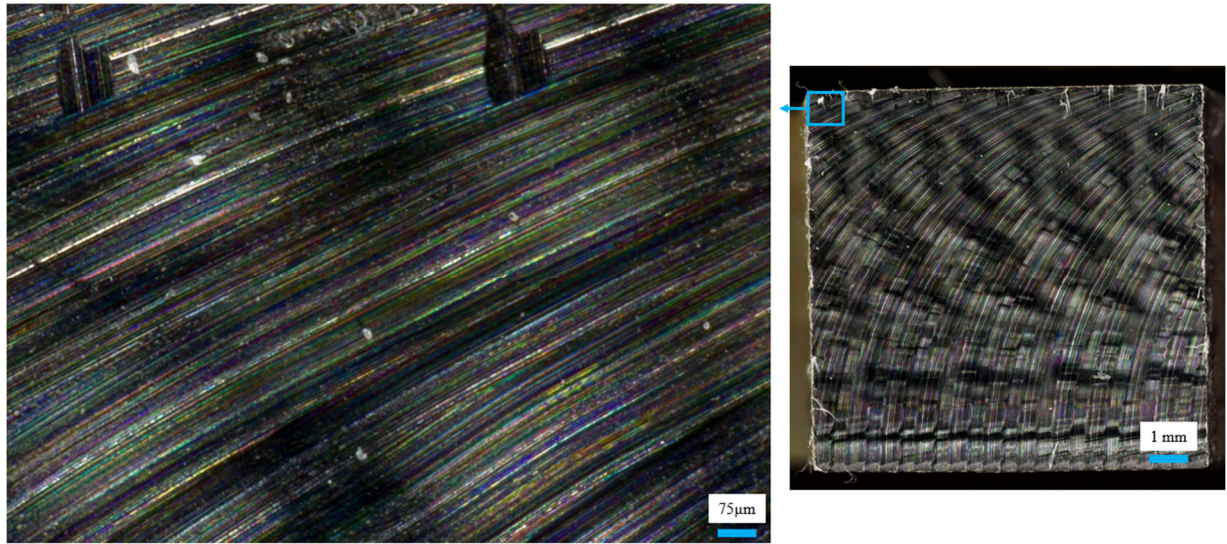


Figure A-19: Zoomed-in Image of Run 1 Top View of a Machined Specimen Using a 25 μm Edge Radius Insert

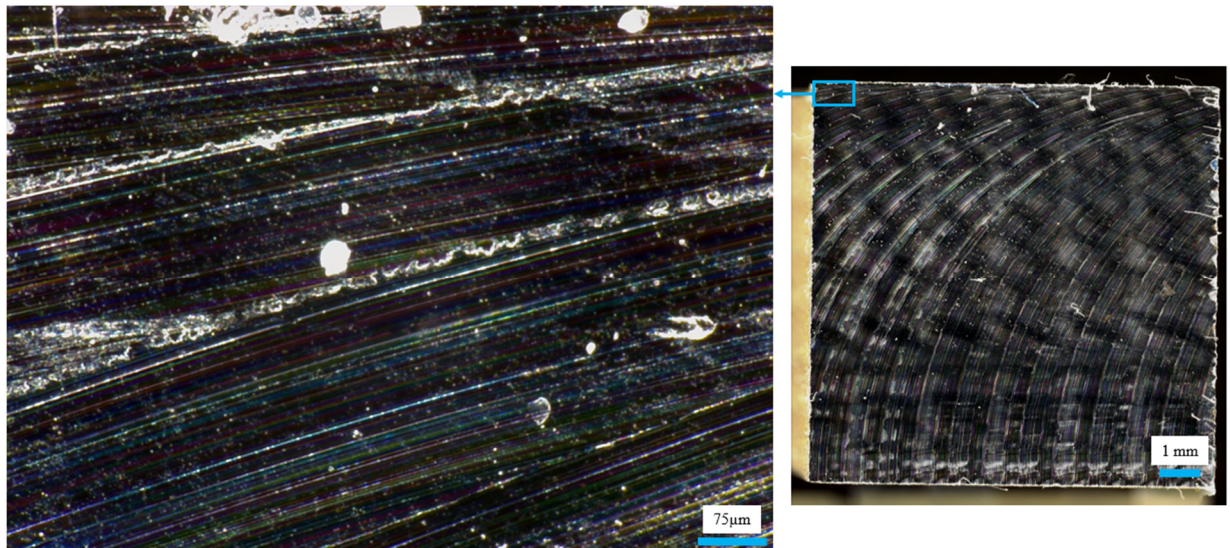


Figure A-20: Zoomed-in Image of Run 5 Top View of a Machined Specimen Using a 25 μm Edge Radius Insert

Appendix A. Feed Marks Figures

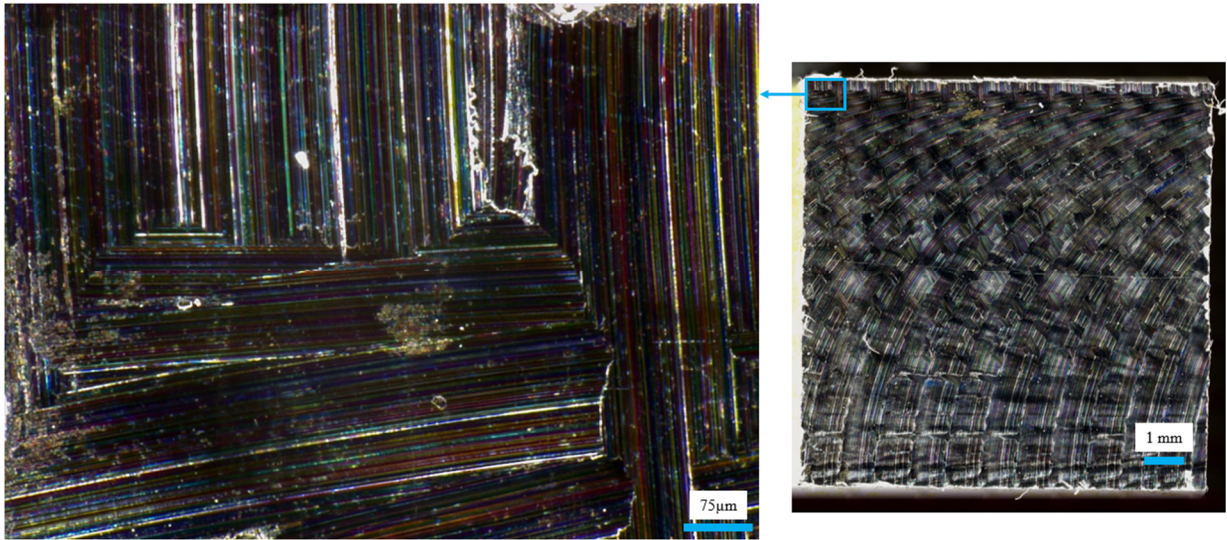


Figure A-21: Zoomed-in Image of Run 21 Top View of a Machined Specimen Using a 30 μm Edge Radius Insert

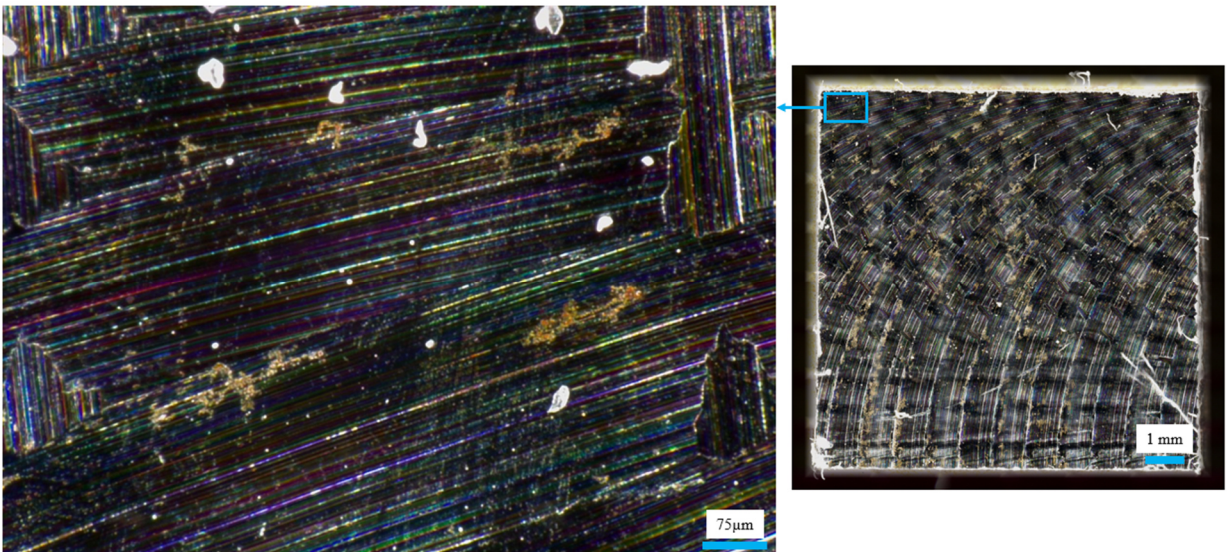


Figure A-22: Zoomed-in Image of Run 26 Top View of a Machined Specimen Using a 30 μm Edge Radius Insert

Appendix A. Feed Marks Figures

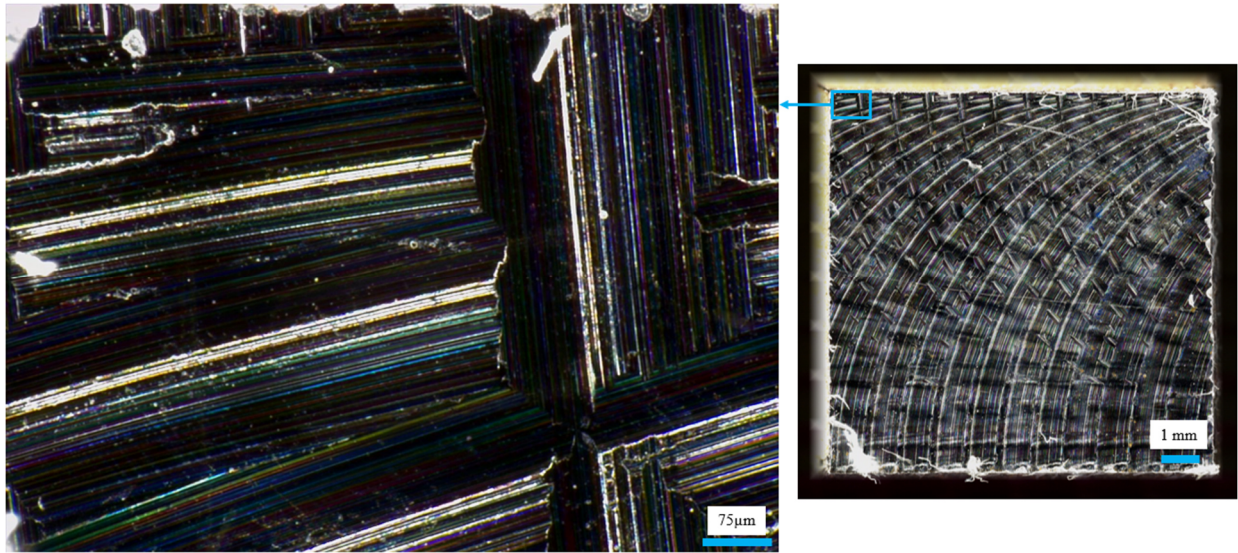


Figure A-23: Zoomed-in Image of Run 31 Top View of a Machined Specimen Using a 30 μm Edge Radius Insert

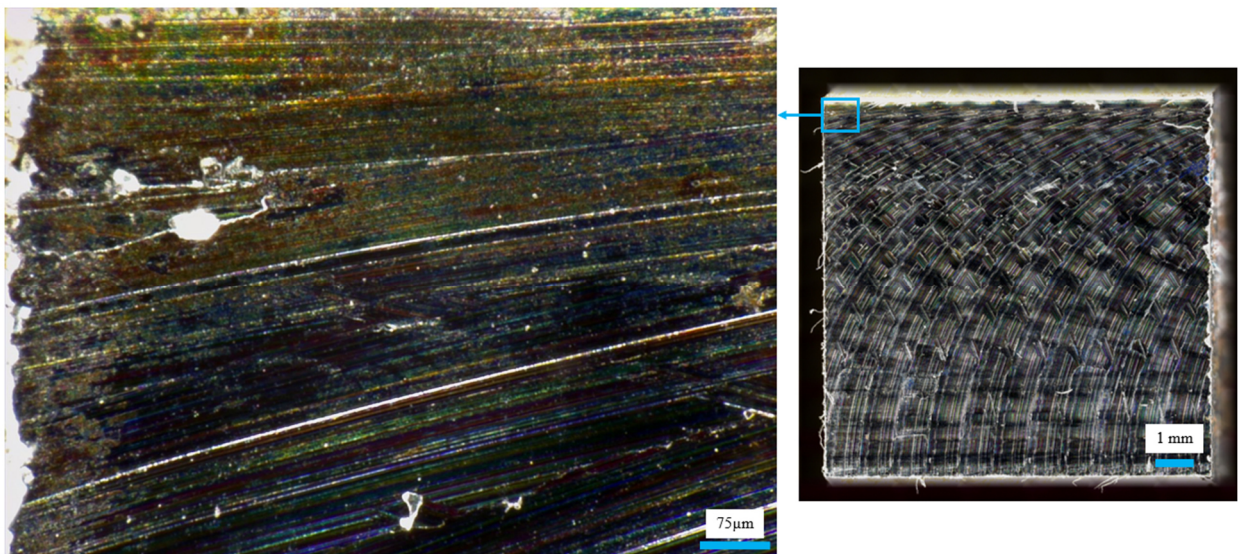


Figure A-24: Zoomed-in Image of Run 35 Top View of a Machined Specimen Using a 30 μm Edge Radius Insert

Appendix A. Feed Marks Figures

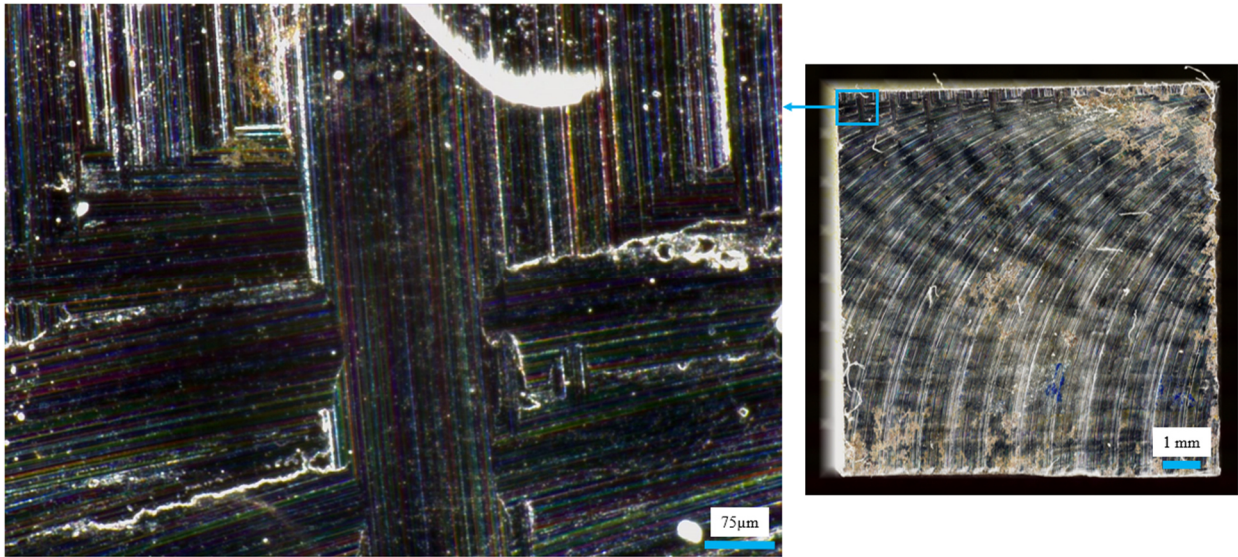


Figure A-25: Zoomed-in Image of Run 31 Top View of a Machined Specimen Using a 35 µm Edge Radius Insert

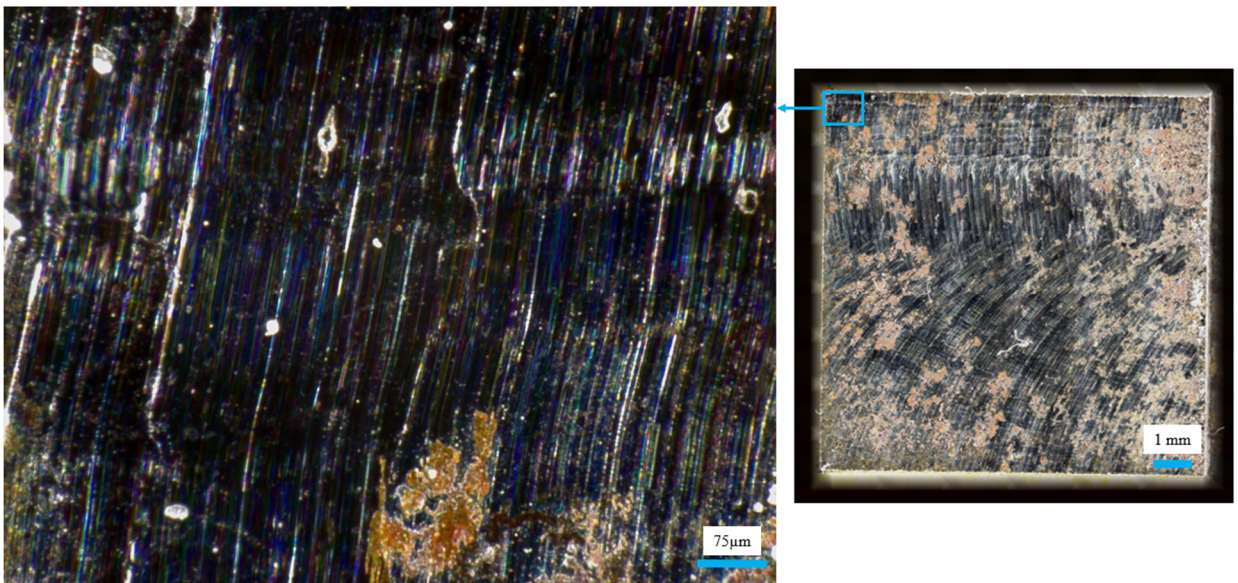


Figure A-26: Zoomed-in Image of Run 36 Top View of a Machined Specimen Using a 35 µm Edge Radius Insert

Appendix A. Feed Marks Figures

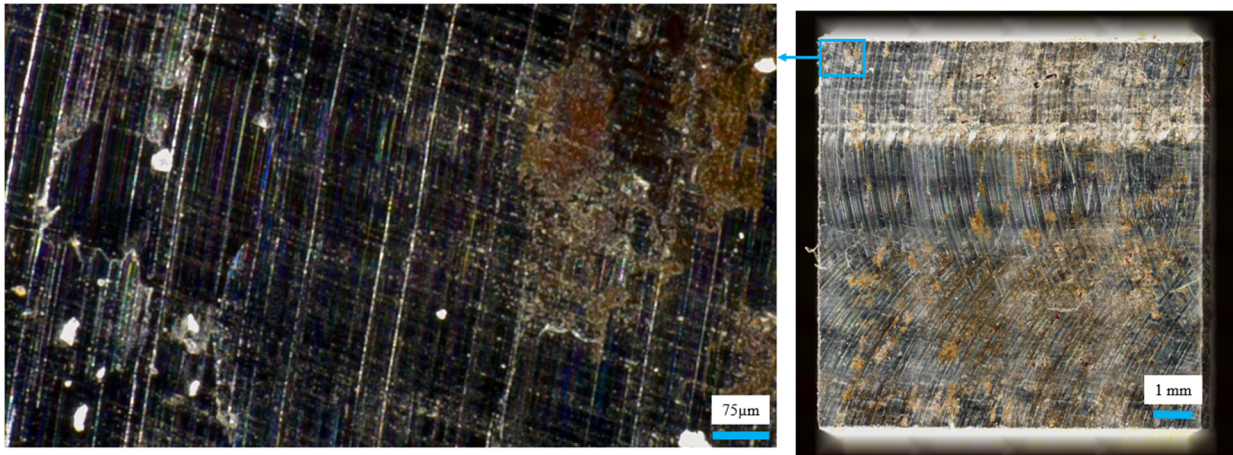


Figure A-27: Zoomed-in Image of Run 41 Top View of a Machined Specimen Using a 35 μm Edge Radius Insert

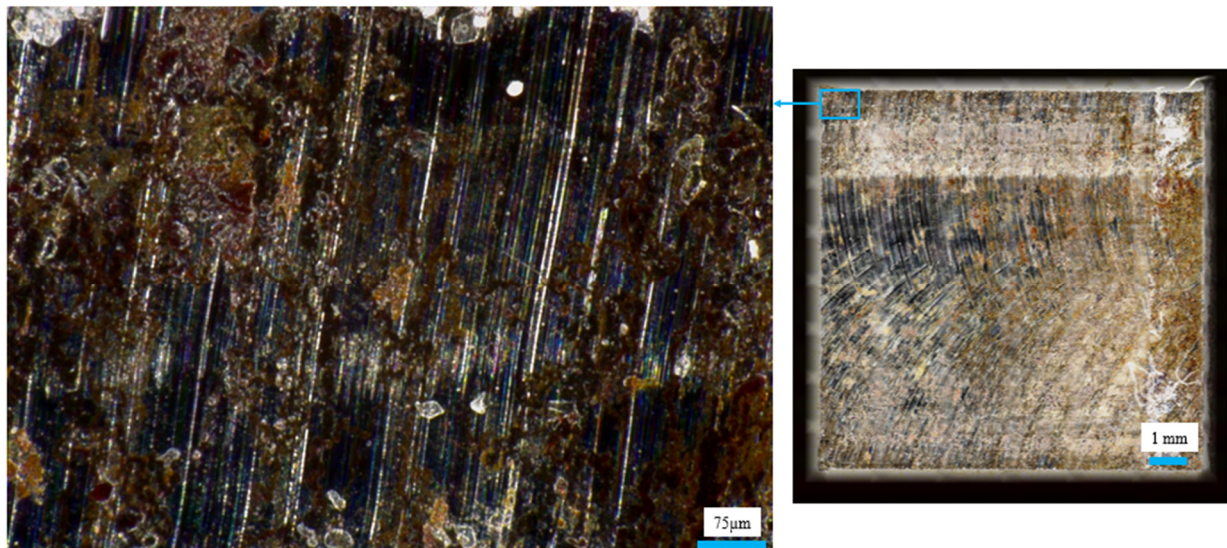


Figure A-28: Zoomed-in Image of Run 45 Top View of a Machined Specimen Using a 35 μm Edge Radius Insert

Appendix A. Feed Marks Figures

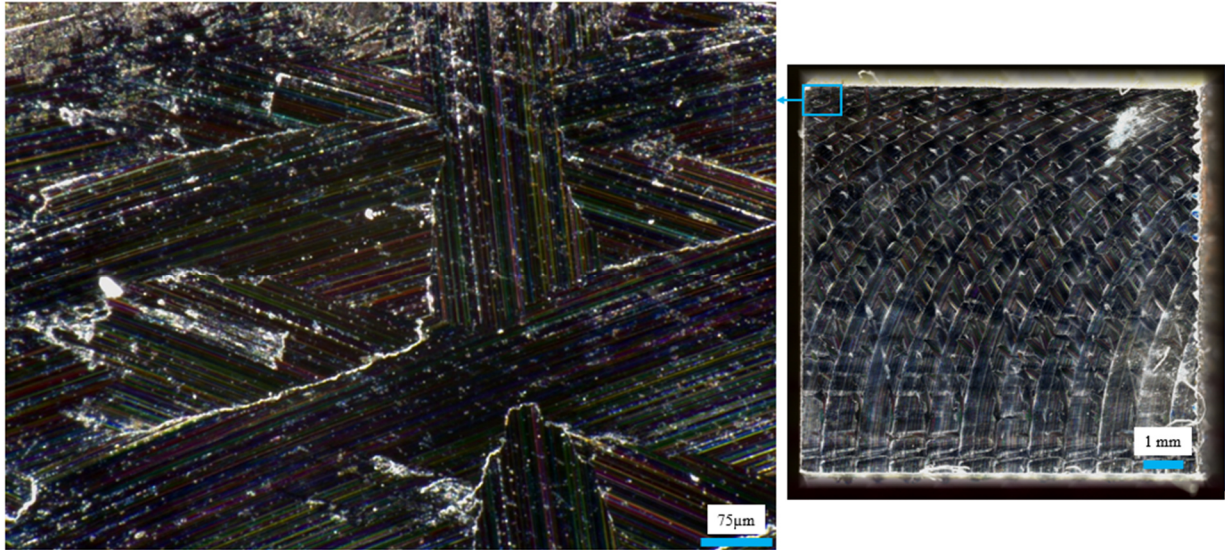


Figure A-29: Zoomed-in Image of Run 8 Top View of a Machined Specimen Using a 40 μm Edge Radius Insert

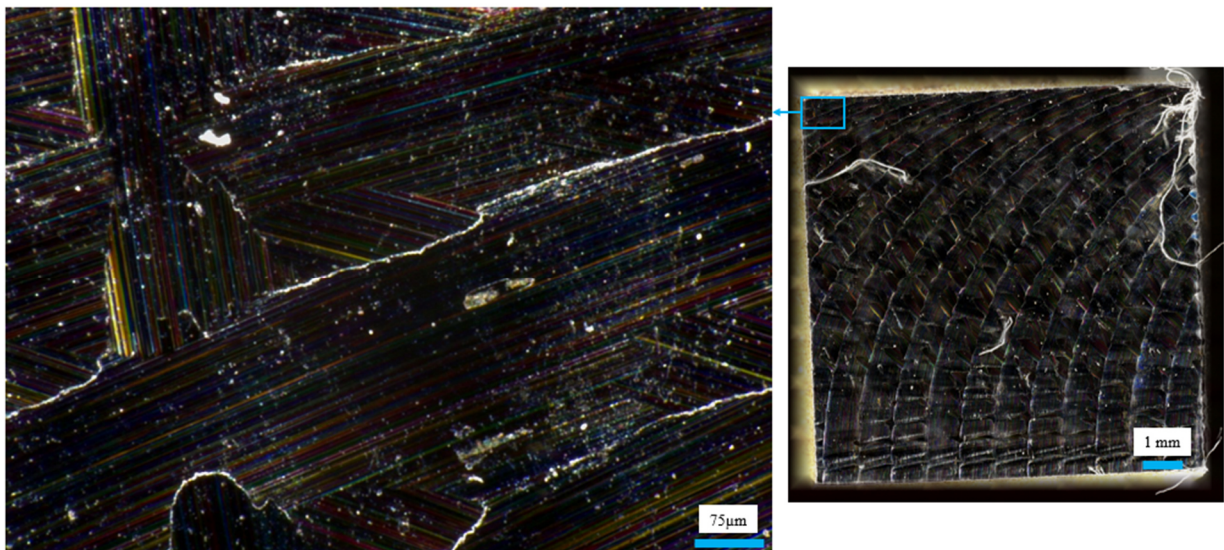


Figure A-30: Zoomed-in Image of Run 13 Top View of a Machined Specimen Using a 40 μm Edge Radius Insert

Appendix A. Feed Marks Figures

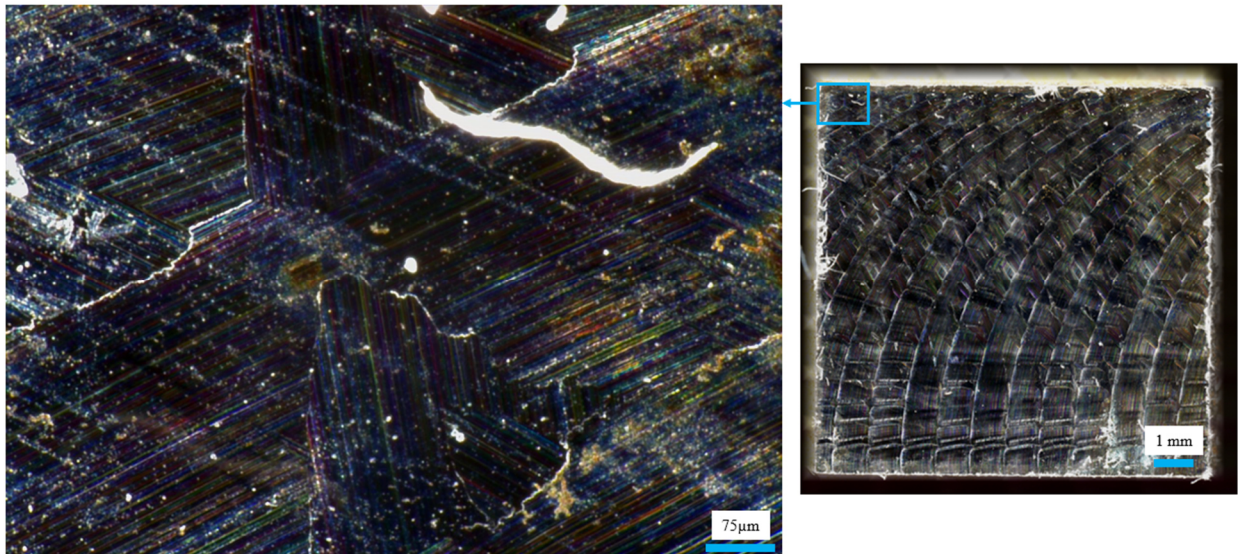


Figure A-31: Zoomed-in Image of Run 18 Top View of a Machined Specimen Using a 40 μm Edge Radius Insert

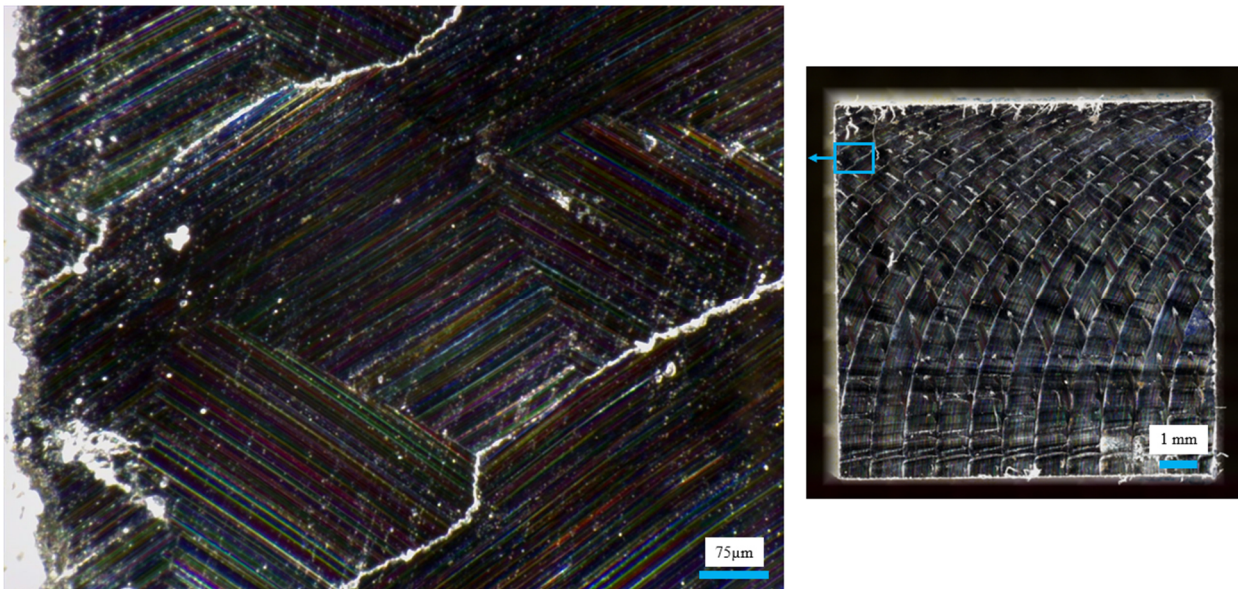


Figure A-32: Zoomed-in Image of Run 22 Top View of a Machined Specimen Using a 40 μm Edge Radius Insert

Appendix A. Feed Marks Figures

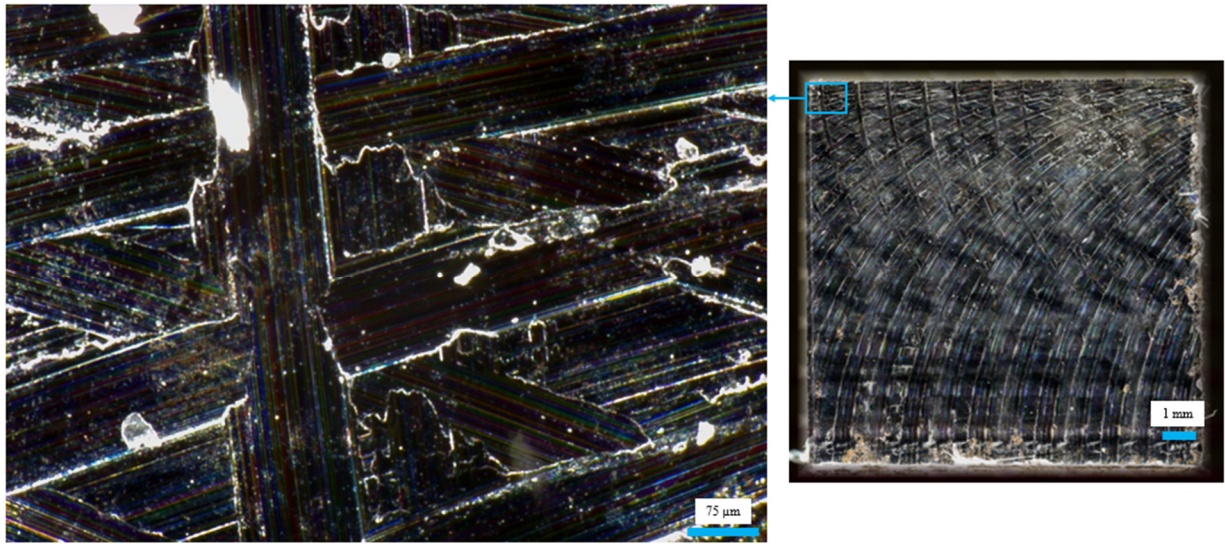


Figure A-33: Zoomed-in Image of Run 18 Top View of a Machined Specimen Using a $45\ \mu\text{m}$ Edge Radius Insert

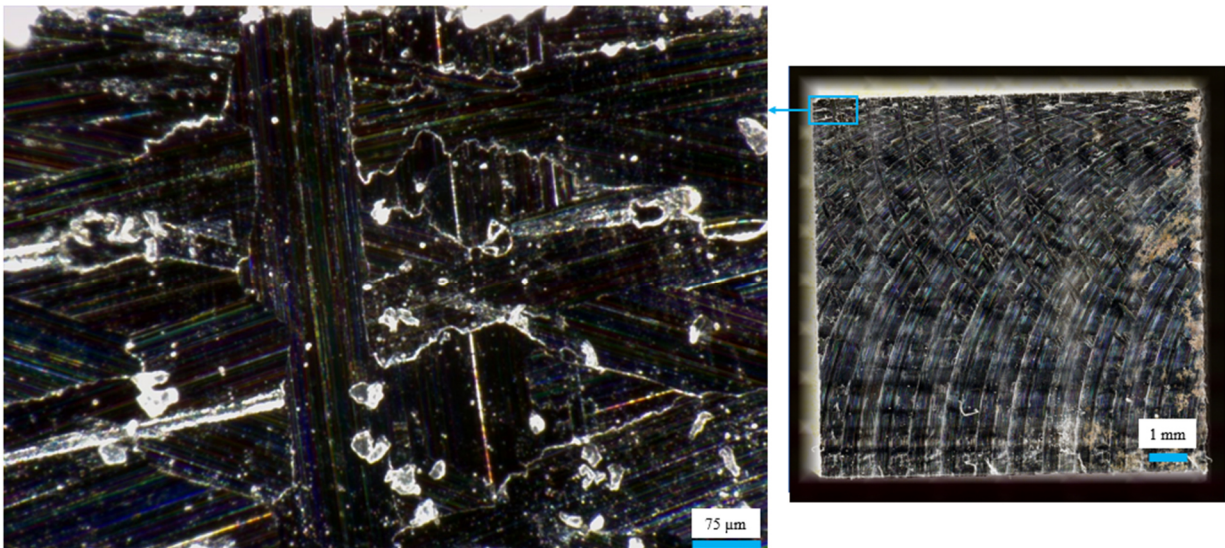


Figure A-34: Zoomed-in Image of Run 23 Top View of a Machined Specimen Using a $45\ \mu\text{m}$ Edge Radius Insert

Appendix A. Feed Marks Figures

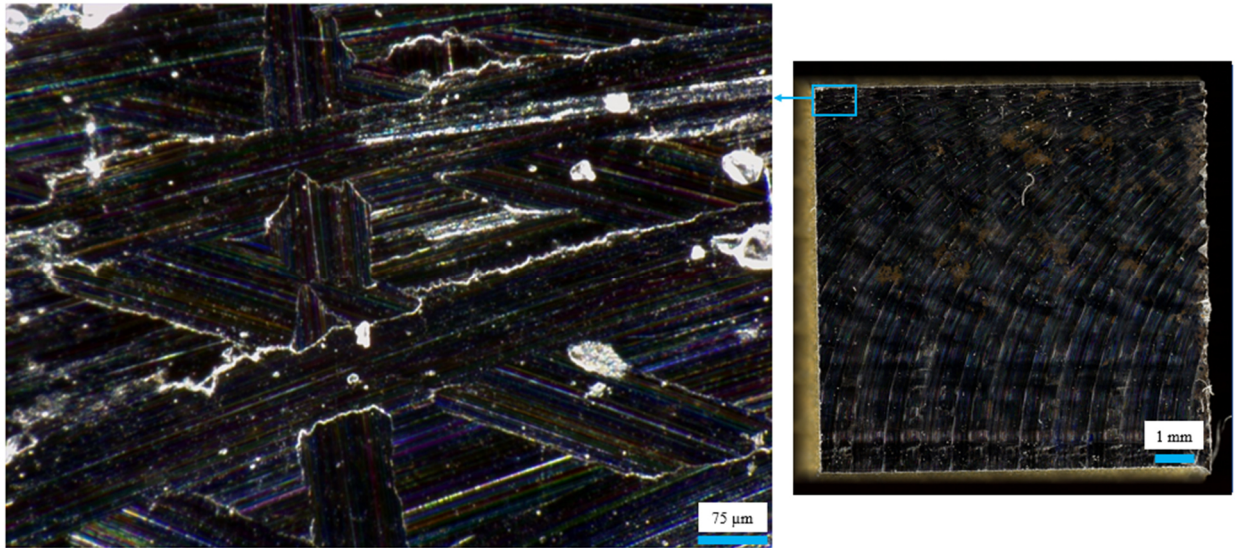


Figure A-35: Zoomed-in Image of Run 28 Top View of a Machined Specimen Using a 45 μm Edge Radius Insert

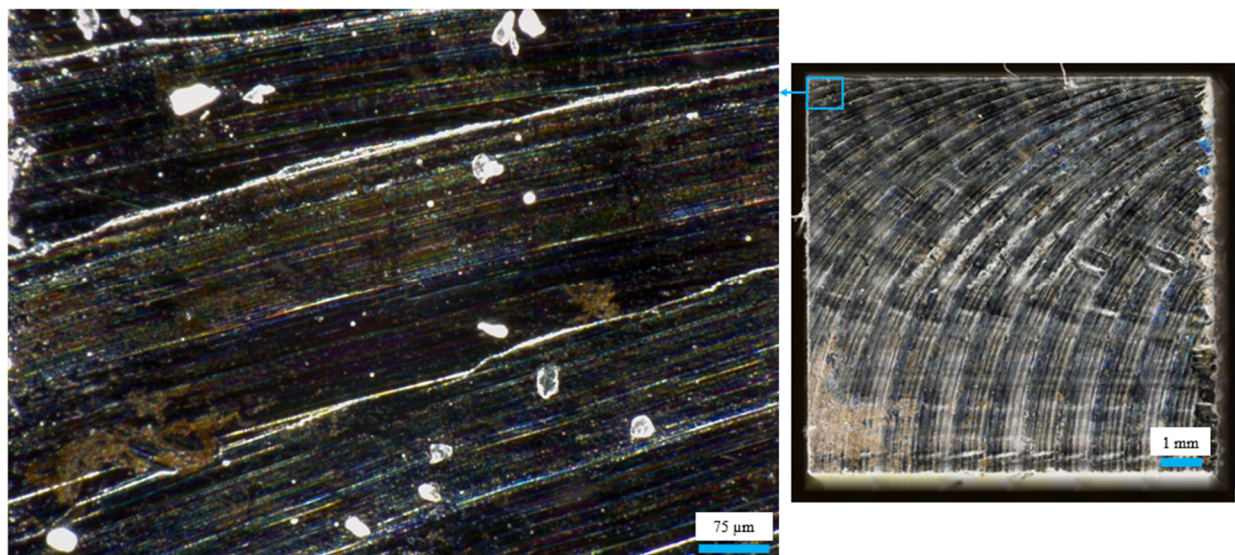


Figure A-36: Zoomed-in Image of Run 32 Top View of a Machined Specimen Using a 45 μm Edge Radius Insert

Appendix B. Subsurface Plastic Deformation Figures

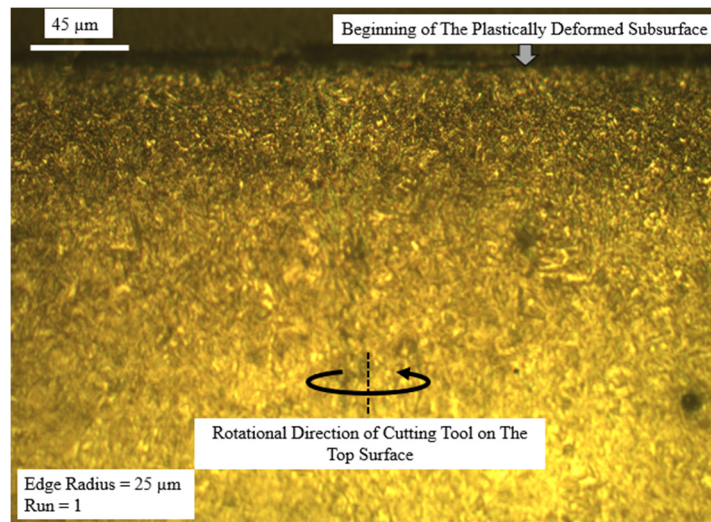


Figure B-1: Subsurface Microstructure of a Machined Specimen Using a 25 μm Edge Radius Insert at Run 1

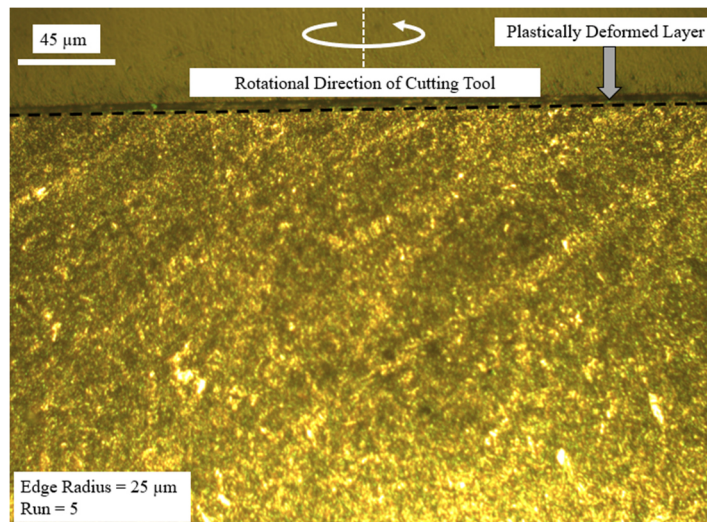


Figure B-2: Subsurface Microstructure of a Machined Specimen Using a 25 μm Edge Radius Insert at Run 5

Appendix B. Subsurface Plastic Deformation Figures

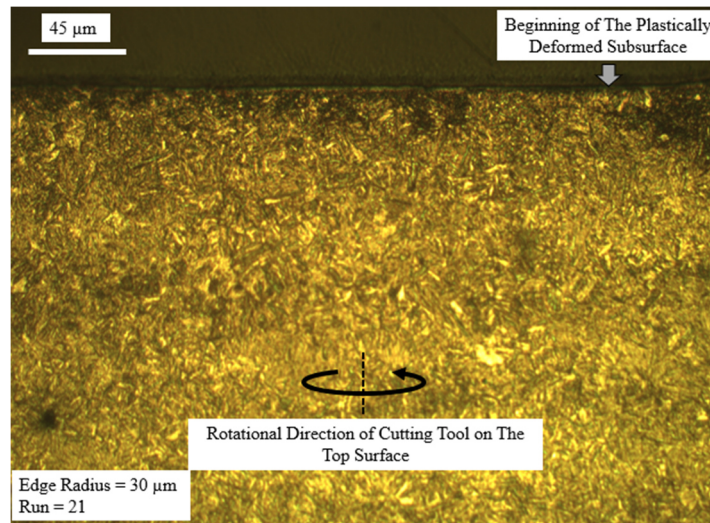


Figure B-3: Subsurface Microstructure of a Machined Specimen Using a 30 μm Edge Radius

Insert at Run 21

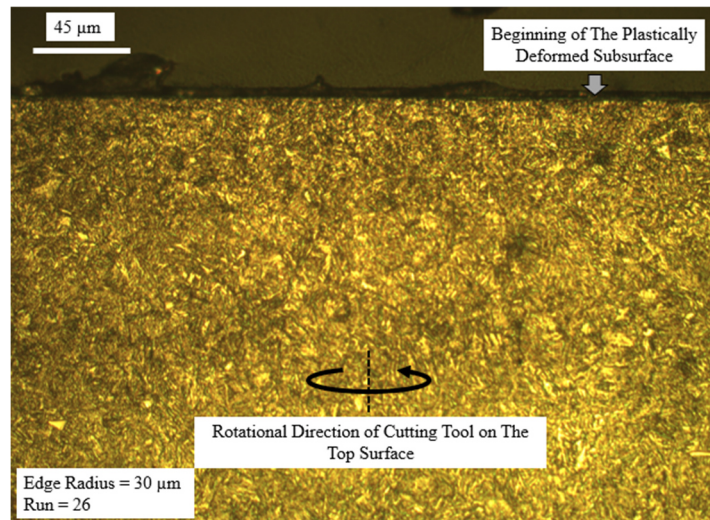


Figure B-4: Subsurface Microstructure of a Machined Specimen Using a 30 μm Edge Radius

Insert at Run 26

Appendix B. Subsurface Plastic Deformation Figures

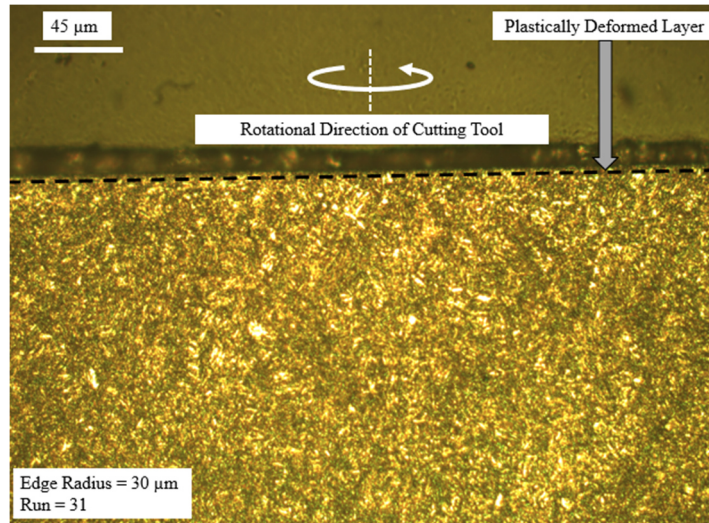


Figure B-5: Subsurface Microstructure of a Machined Specimen Using a 30 μm Edge Radius Insert at Run 31

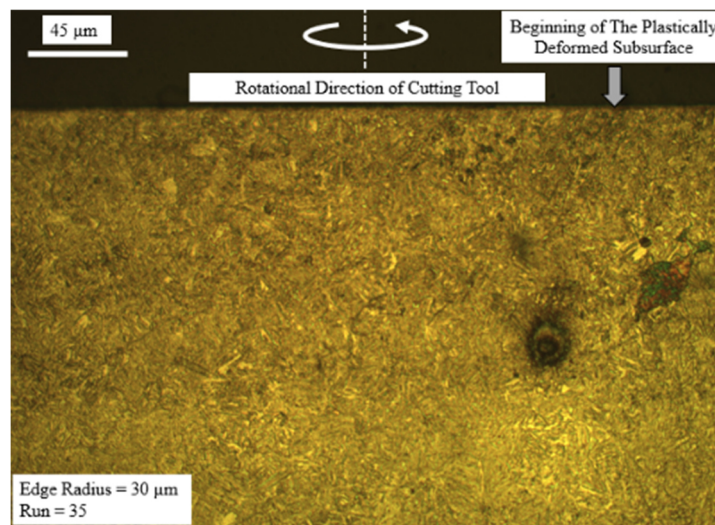


Figure B-6: Subsurface Microstructure of a Machined Specimen Using a 30 μm Edge Radius Insert at Run 35

Appendix B. Subsurface Plastic Deformation Figures

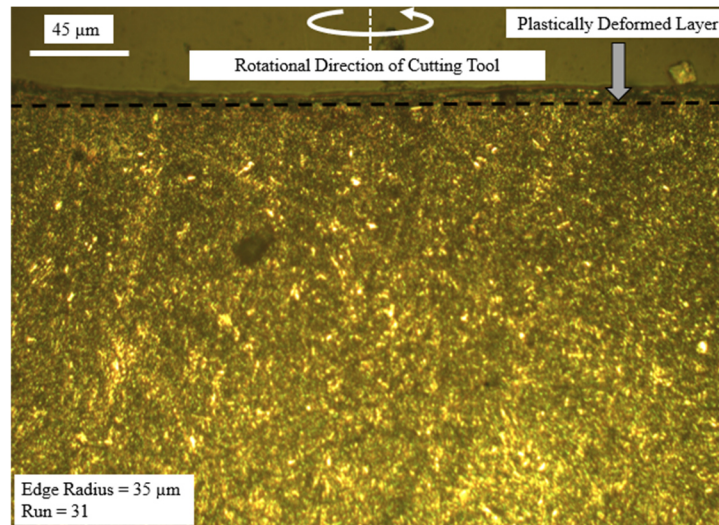


Figure B-7: Subsurface Microstructure of a Machined Specimen Using a 35 μm Edge Radius Insert at Run 31

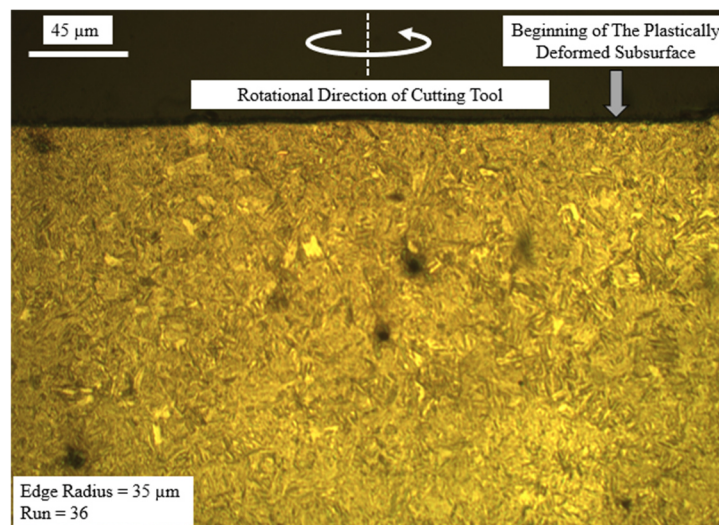


Figure B-8: Subsurface Microstructure of a Machined Specimen Using a 35 μm Edge Radius Insert at Run 36

Appendix B. Subsurface Plastic Deformation Figures

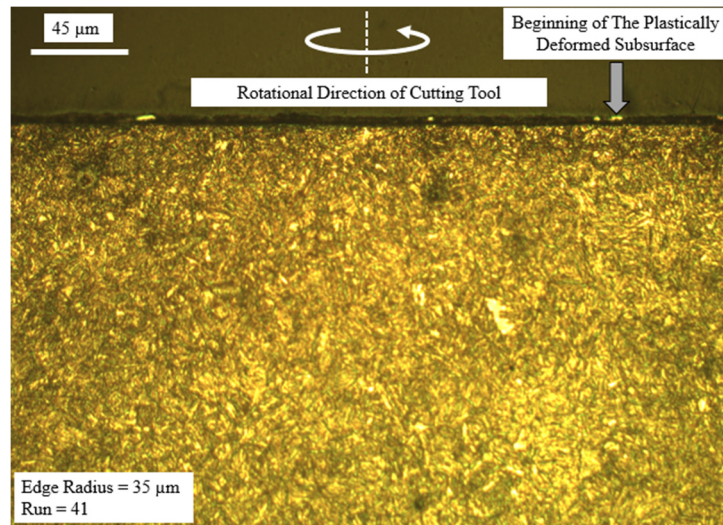


Figure B-9: Subsurface Microstructure of a Machined Specimen Using a 35 μm Edge Radius Insert at Run 41

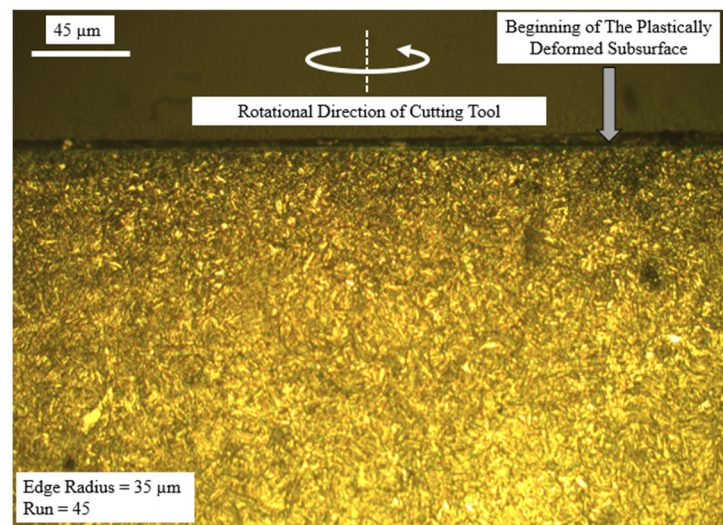


Figure B-10: Subsurface Microstructure of a Machined Specimen Using a 35 μm Edge Radius Insert at Run 45

Appendix B. Subsurface Plastic Deformation Figures

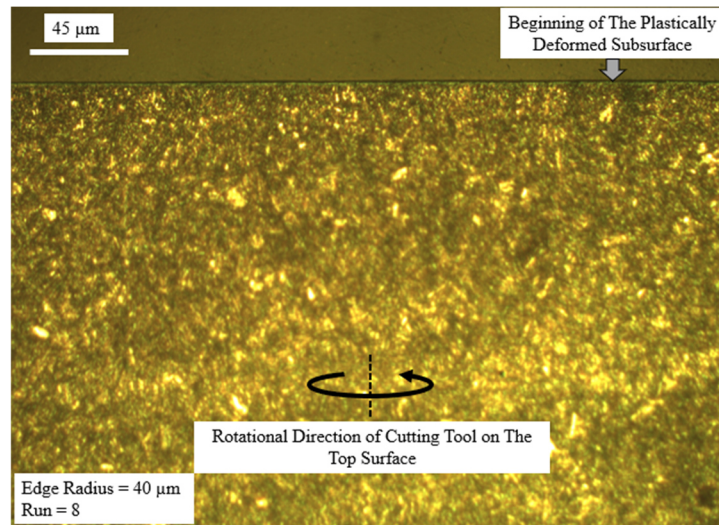


Figure B-11: Subsurface Microstructure of a Machined Specimen Using a 40 μm Edge Radius Insert at Run 8

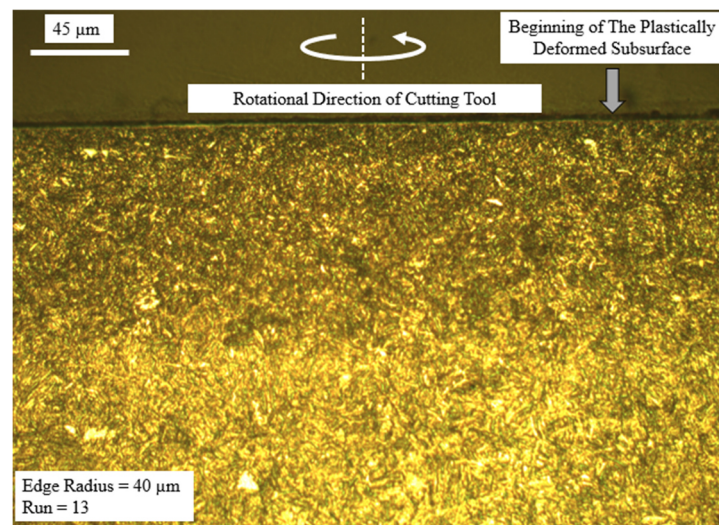


Figure B-12: Subsurface Microstructure of a Machined Specimen Using a 40 μm Edge Radius Insert at Run 13

Appendix B. Subsurface Plastic Deformation Figures

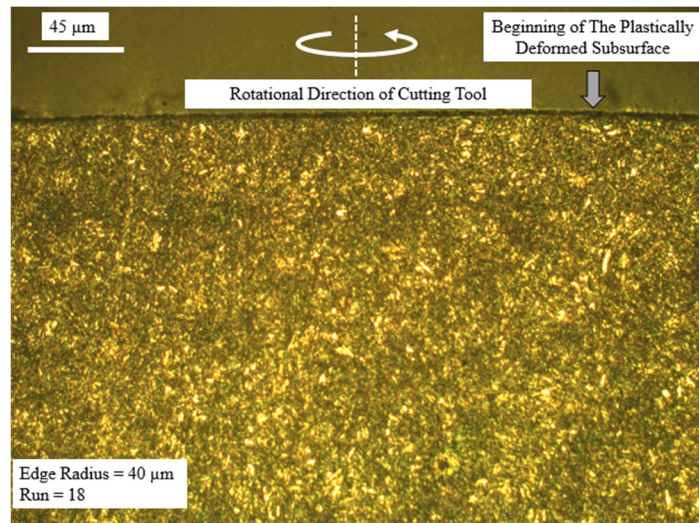


Figure B-13: Subsurface Microstructure of a Machined Specimen Using a 40 μm Edge Radius Insert at Run 18

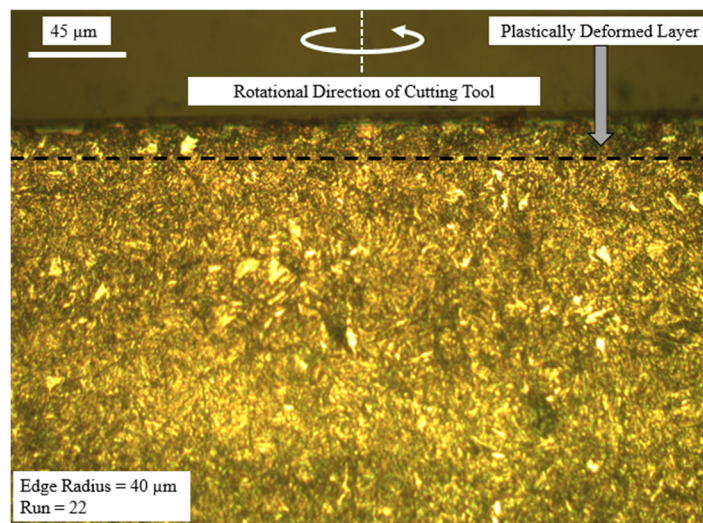


Figure B-14: Subsurface Microstructure of a Machined Specimen Using a 40 μm Edge Radius Insert at Run 22

Appendix B. Subsurface Plastic Deformation Figures

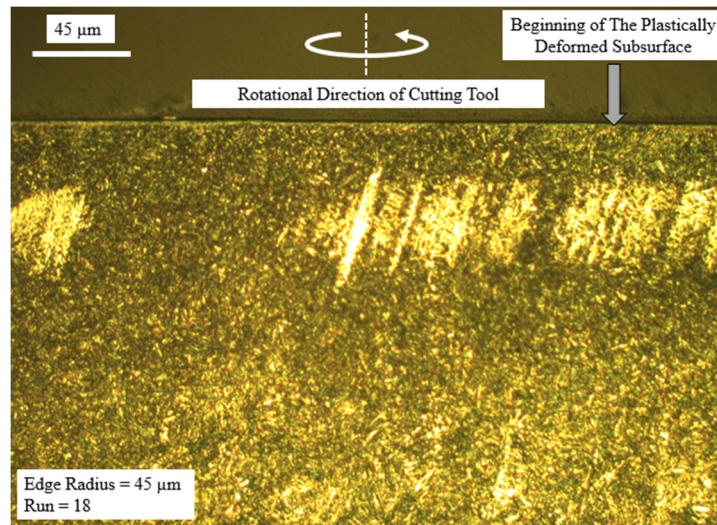


Figure B-15: Subsurface Microstructure of a Machined Specimen Using a 45 μm Edge Radius Insert at Run 18

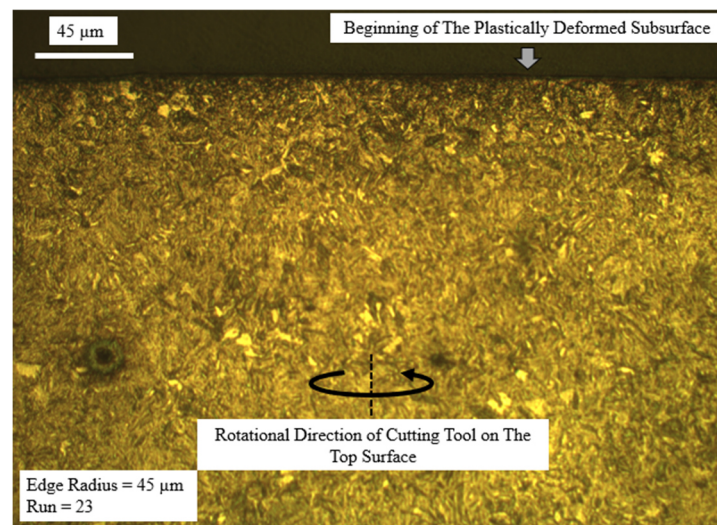


Figure B-16: Subsurface Microstructure of a Machined Specimen Using a 45 μm Edge Radius Insert at Run 23

Appendix B. Subsurface Plastic Deformation Figures

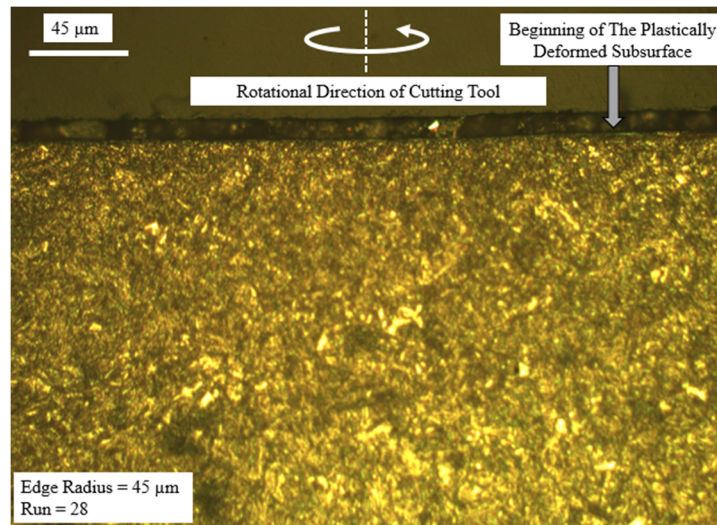


Figure B-17: Subsurface Microstructure of a Machined Specimen Using a 45 μm Edge Radius Insert at Run 28

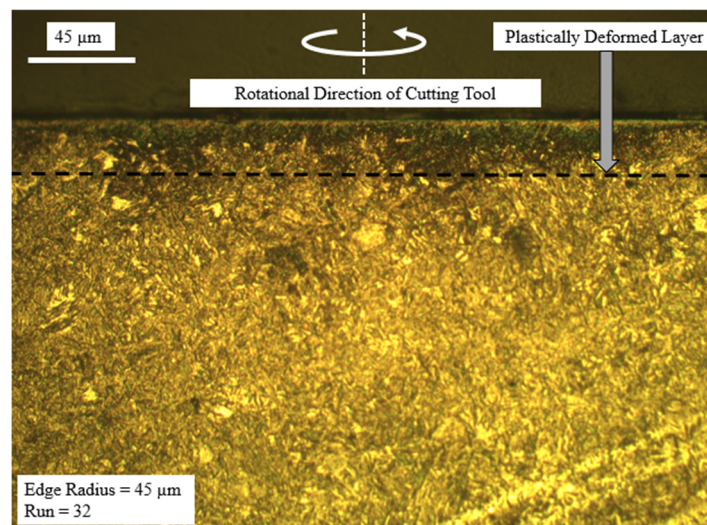


Figure B-18: Subsurface Microstructure of a Machined Specimen Using a 45 μm Edge Radius Insert at Run 32